

Cross Sections for the Reactions $e^+e^- \rightarrow K^+K^-\pi^+\pi^-$, $K^+K^-\pi^0\pi^0$, and $K^+K^-K^+K^-$ Measured Using Initial-State Radiation

J. P. Lees, V. Poireau, E. Prencipe, and V. Tisserand
*Laboratoire d'Annecy-le-Vieux de Physique des Particules (LAPP),
Université de Savoie, CNRS/IN2P3, F-74941 Annecy-Le-Vieux, France*

J. Garra Tico and E. Grauges
Universitat de Barcelona, Facultat de Física, Departament ECM, E-08028 Barcelona, Spain

M. Martinelli^{ab}, D. A. Milanes^{ab}, A. Palano^{ab}, and M. Pappagallo^{ab}
INFN Sezione di Bari^a; Dipartimento di Fisica, Università di Bari^b, I-70126 Bari, Italy

G. Eigen, B. Stugu, and L. Sun
University of Bergen, Institute of Physics, N-5007 Bergen, Norway

D. N. Brown, L. T. Kerth, Yu. G. Kolomensky, and G. Lynch
Lawrence Berkeley National Laboratory and University of California, Berkeley, California 94720, USA

H. Koch and T. Schroeder
Ruhr Universität Bochum, Institut für Experimentalphysik 1, D-44780 Bochum, Germany

D. J. Asgeirsson, C. Hearty, T. S. Mattison, and J. A. McKenna
University of British Columbia, Vancouver, British Columbia, Canada V6T 1Z1

A. Khan
Brunel University, Uxbridge, Middlesex UB8 3PH, United Kingdom

V. E. Blinov, A. R. Buzykaev, V. P. Druzhinin, V. B. Golubev, E. A. Kravchenko, A. P. Onuchin,
S. I. Serebnyakov, Yu. I. Skovpen, E. P. Solodov, K. Yu. Todyshev, and A. N. Yushkov
Budker Institute of Nuclear Physics, Novosibirsk 630090, Russia

M. Bondioli, S. Curry, D. Kirkby, A. J. Lankford, M. Mandelkern, and D. P. Stoker
University of California at Irvine, Irvine, California 92697, USA

H. Atmacan, J. W. Gary, F. Liu, O. Long, and G. M. Vitug
University of California at Riverside, Riverside, California 92521, USA

C. Campagnari, T. M. Hong, D. Kovalskyi, J. D. Richman, and C. A. West
University of California at Santa Barbara, Santa Barbara, California 93106, USA

A. M. Eisner, J. Kroseberg, W. S. Lockman, A. J. Martinez, T. Schalk, B. A. Schumm, and A. Seiden
University of California at Santa Cruz, Institute for Particle Physics, Santa Cruz, California 95064, USA

C. H. Cheng, D. A. Doll, B. Echenard, K. T. Flood, D. G. Hitlin, P. Ongmongkolkul, F. C. Porter, and A. Y. Rakitin
California Institute of Technology, Pasadena, California 91125, USA

R. Andreassen, M. S. Dubrovin, B. T. Meadows, and M. D. Sokoloff
University of Cincinnati, Cincinnati, Ohio 45221, USA

P. C. Bloom, W. T. Ford, A. Gaz, M. Nagel, U. Nauenberg, J. G. Smith, and S. R. Wagner
University of Colorado, Boulder, Colorado 80309, USA

R. Ayad* and W. H. Toki

Colorado State University, Fort Collins, Colorado 80523, USA

B. Spaan

Technische Universität Dortmund, Fakultät Physik, D-44221 Dortmund, Germany

M. J. Kobel, K. R. Schubert, and R. Schwierz

Technische Universität Dresden, Institut für Kern- und Teilchenphysik, D-01062 Dresden, Germany

D. Bernard and M. Verderi

Laboratoire Leprince-Ringuet, CNRS/IN2P3, Ecole Polytechnique, F-91128 Palaiseau, France

P. J. Clark, S. Playfer, and J. E. Watson

University of Edinburgh, Edinburgh EH9 3JZ, United Kingdom

D. Bettoni^a, C. Bozzi^a, R. Calabrese^{ab}, G. Cibinetto^{ab}, E. Fioravanti^{ab},

I. Garzia^{ab}, E. Luppi^{ab}, M. Munerato^{ab}, M. Negrini^{ab}, and L. Piemontese^a
INFN Sezione di Ferrara^a; Dipartimento di Fisica, Università di Ferrara^b, I-44100 Ferrara, Italy

R. Baldini-Ferroli, A. Calcaterra, R. de Sangro, G. Finocchiaro, M. Nicolaci,

S. Pacetti, P. Patteri, I. M. Peruzzi,[†] M. Piccolo, M. Rama, and A. Zallo
INFN Laboratori Nazionali di Frascati, I-00044 Frascati, Italy

R. Contri^{ab}, E. Guido^{ab}, M. Lo Vetere^{ab}, M. R. Monge^{ab}, S. Passaggio^a, C. Patrignani^{ab}, and E. Robutti^a

INFN Sezione di Genova^a; Dipartimento di Fisica, Università di Genova^b, I-16146 Genova, Italy

B. Bhuyan and V. Prasad

Indian Institute of Technology Guwahati, Guwahati, Assam, 781 039, India

C. L. Lee and M. Morii

Harvard University, Cambridge, Massachusetts 02138, USA

A. J. Edwards

Harvey Mudd College, Claremont, California 91711

A. Adametz, J. Marks, and U. Uwer

Universität Heidelberg, Physikalisches Institut, Philosophenweg 12, D-69120 Heidelberg, Germany

F. U. Bernlochner, M. Ebert, H. M. Lacker, and T. Lueck

Humboldt-Universität zu Berlin, Institut für Physik, Newtonstr. 15, D-12489 Berlin, Germany

P. D. Dauncey and M. Tibbetts

Imperial College London, London, SW7 2AZ, United Kingdom

P. K. Behera and U. Mallik

University of Iowa, Iowa City, Iowa 52242, USA

C. Chen, J. Cochran, H. B. Crawley, W. T. Meyer, S. Prell, E. I. Rosenberg, and A. E. Rubin

Iowa State University, Ames, Iowa 50011-3160, USA

A. V. Gritsan and Z. J. Guo

Johns Hopkins University, Baltimore, Maryland 21218, USA

N. Arnaud, M. Davier, D. Derkach, G. Grosdidier, F. Le Diberder, A. M. Lutz,

B. Malaescu, P. Roudeau, M. H. Schune, A. Stocchi, and G. Wormser
*Laboratoire de l'Accélérateur Linéaire, IN2P3/CNRS et Université Paris-Sud 11,
Centre Scientifique d'Orsay, B. P. 34, F-91898 Orsay Cedex, France*

D. J. Lange and D. M. Wright

Lawrence Livermore National Laboratory, Livermore, California 94550, USA

I. Bingham, C. A. Chavez, J. P. Coleman, J. R. Fry, E. Gabathuler, D. E. Hutchcroft, D. J. Payne, and C. Touramanis
University of Liverpool, Liverpool L69 7ZE, United Kingdom

A. J. Bevan, F. Di Lodovico, R. Sacco, and M. Sigamani
Queen Mary, University of London, London, E1 4NS, United Kingdom

G. Cowan and S. Paramesvaran
University of London, Royal Holloway and Bedford New College, Egham, Surrey TW20 0EX, United Kingdom

D. N. Brown and C. L. Davis
University of Louisville, Louisville, Kentucky 40292, USA

A. G. Denig, M. Fritsch, W. Gradl, and A. Hafner
Johannes Gutenberg-Universität Mainz, Institut für Kernphysik, D-55099 Mainz, Germany

K. E. Alwyn, D. Bailey, R. J. Barlow, G. Jackson, and G. D. Lafferty
University of Manchester, Manchester M13 9PL, United Kingdom

R. Cenci, B. Hamilton, A. Jawahery, D. A. Roberts, and G. Simi
University of Maryland, College Park, Maryland 20742, USA

C. Dallapiccola and E. Salvati
University of Massachusetts, Amherst, Massachusetts 01003, USA

R. Cowan, D. Dujmic, and G. Sciolla
Massachusetts Institute of Technology, Laboratory for Nuclear Science, Cambridge, Massachusetts 02139, USA

D. Lindemann, P. M. Patel, S. H. Robertson, and M. Schram
McGill University, Montréal, Québec, Canada H3A 2T8

P. Biassoni^{ab}, A. Lazzaro^{ab}, V. Lombardo^a, F. Palombo^{ab}, and S. Stracka^{ab}
INFN Sezione di Milano^a; Dipartimento di Fisica, Università di Milano^b, I-20133 Milano, Italy

L. Cremaldi, R. Godang,[‡] R. Kroeger, P. Sonnek, and D. J. Summers
University of Mississippi, University, Mississippi 38677, USA

X. Nguyen and P. Taras
Université de Montréal, Physique des Particules, Montréal, Québec, Canada H3C 3J7

G. De Nardo^{ab}, D. Monorchio^{ab}, G. Onorato^{ab}, and C. Sciacca^{ab}
INFN Sezione di Napoli^a; Dipartimento di Scienze Fisiche, Università di Napoli Federico II^b, I-80126 Napoli, Italy

G. Raven and H. L. Snoek
NIKHEF, National Institute for Nuclear Physics and High Energy Physics, NL-1009 DB Amsterdam, The Netherlands

C. P. Jessop, K. J. Knoepfel, J. M. LoSecco, and W. F. Wang
University of Notre Dame, Notre Dame, Indiana 46556, USA

K. Honscheid and R. Kass
Ohio State University, Columbus, Ohio 43210, USA

J. Brau, R. Frey, N. B. Sinev, D. Strom, and E. Torrence
University of Oregon, Eugene, Oregon 97403, USA

E. Feltresi^{ab}, N. Gagliardi^{ab}, M. Margoni^{ab}, M. Morandin^a,

M. Posocco^a, M. Rotondo^a, F. Simonetto^{ab}, and R. Stroili^{ab}
INFN Sezione di Padova^a; Dipartimento di Fisica, Università di Padova^b, I-35131 Padova, Italy

E. Ben-Haim, M. Bomben, G. R. Bonneaud, H. Briand, G. Calderini,
 J. Chauveau, O. Hamon, Ph. Leruste, G. Marchiori, J. Ocariz, and S. Sitt
*Laboratoire de Physique Nucléaire et de Hautes Energies,
 IN2P3/CNRS, Université Pierre et Marie Curie-Paris6,
 Université Denis Diderot-Paris7, F-75252 Paris, France*

M. Biasini^{ab}, E. Manoni^{ab}, and A. Rossi^{ab}
INFN Sezione di Perugia^a; Dipartimento di Fisica, Università di Perugia^b, I-06100 Perugia, Italy

C. Angelini^{ab}, G. Batignani^{ab}, S. Bettarini^{ab}, M. Carpinelli^{ab},[§] G. Casarosa^{ab}, A. Cervelli^{ab}, F. Forti^{ab},
 M. A. Giorgi^{ab}, A. Lusiani^{ac}, N. Neri^{ab}, B. Oberhof^{ab}, E. Paoloni^{ab}, A. Perez^a, G. Rizzo^{ab}, and J. J. Walsh^a
INFN Sezione di Pisa^a; Dipartimento di Fisica, Università di Pisa^b; Scuola Normale Superiore di Pisa^c, I-56127 Pisa, Italy

D. Lopes Pegna, C. Lu, J. Olsen, A. J. S. Smith, and A. V. Telnov
Princeton University, Princeton, New Jersey 08544, USA

F. Anulli^a, G. Cavoto^a, R. Faccini^{ab}, F. Ferrarotto^a, F. Ferroni^{ab},
 M. Gaspero^{ab}, L. Li Gioi^a, M. A. Mazzoni^a, and G. Piredda^a
*INFN Sezione di Roma^a; Dipartimento di Fisica,
 Università di Roma La Sapienza^b, I-00185 Roma, Italy*

C. Bünger, T. Hartmann, T. Leddig, H. Schröder, and R. Waldi
Universität Rostock, D-18051 Rostock, Germany

T. Adye, E. O. Olaiya, and F. F. Wilson
Rutherford Appleton Laboratory, Chilton, Didcot, Oxon, OX11 0QX, United Kingdom

S. Emery, G. Hamel de Monchenault, G. Vasseur, and Ch. Yèche
CEA, Irfu, SPP, Centre de Saclay, F-91191 Gif-sur-Yvette, France

D. Aston, D. J. Bard, R. Bartoldus, J. F. Benitez, C. Cartaro, M. R. Convery, J. Dorfan,
 G. P. Dubois-Felsmann, W. Dunwoodie, R. C. Field, M. Franco Sevilla, B. G. Fulsom, A. M. Gabareen,
 M. T. Graham, P. Grenier, C. Hast, W. R. Innes, M. H. Kelsey, H. Kim, P. Kim, M. L. Kocian,
 D. W. G. S. Leith, P. Lewis, S. Li, B. Lindquist, S. Luitz, V. Luth, H. L. Lynch, D. B. MacFarlane,
 D. R. Muller, H. Neal, S. Nelson, I. Ofte, M. Perl, T. Pulliam, B. N. Ratcliff, A. Roodman, A. A. Salnikov,
 V. Santoro, R. H. Schindler, A. Snyder, D. Su, M. K. Sullivan, J. Va'vra, A. P. Wagner, M. Weaver,
 W. J. Wisniewski, M. Wittgen, D. H. Wright, H. W. Wulsin, A. K. Yarritu, C. C. Young, and V. Ziegler
SLAC National Accelerator Laboratory, Stanford, California 94309 USA

W. Park, M. V. Purohit, R. M. White, and J. R. Wilson
University of South Carolina, Columbia, South Carolina 29208, USA

A. Randle-Conde and S. J. Sekula
Southern Methodist University, Dallas, Texas 75275, USA

M. Bellis, P. R. Burchat, and T. S. Miyashita
Stanford University, Stanford, California 94305-4060, USA

M. S. Alam and J. A. Ernst
State University of New York, Albany, New York 12222, USA

R. Gorodeisky, N. Guttman, D. R. Peimer, and A. Soffer
Tel Aviv University, School of Physics and Astronomy, Tel Aviv, 69978, Israel

P. Lund and S. M. Spanier

University of Tennessee, Knoxville, Tennessee 37996, USA

R. Eckmann, J. L. Ritchie, A. M. Ruland, C. J. Schilling, R. F. Schwitters, and B. C. Wray
University of Texas at Austin, Austin, Texas 78712, USA

J. M. Izen and X. C. Lou
University of Texas at Dallas, Richardson, Texas 75083, USA

F. Bianchi^{ab} and D. Gamba^{ab}
INFN Sezione di Torino^a; Dipartimento di Fisica Sperimentale, Università di Torino^b, I-10125 Torino, Italy

L. Lanceri^{ab} and L. Vitale^{ab}
INFN Sezione di Trieste^a; Dipartimento di Fisica, Università di Trieste^b, I-34127 Trieste, Italy

N. Lopez-March, F. Martinez-Vidal, and A. Oyanguren
IFIC, Universitat de Valencia-CSIC, E-46071 Valencia, Spain

H. Ahmed, J. Albert, Sw. Banerjee, H. H. F. Choi, G. J. King, R. Kowalewski,
 M. J. Lewczuk, C. Lindsay, I. M. Nugent, J. M. Roney, and R. J. Sobie
University of Victoria, Victoria, British Columbia, Canada V8W 3P6

T. J. Gershon, P. F. Harrison, T. E. Latham, and E. M. T. Puccio
Department of Physics, University of Warwick, Coventry CV4 7AL, United Kingdom

H. R. Band, S. Dasu, Y. Pan, R. Prepost, C. O. Vuosalo, and S. L. Wu
University of Wisconsin, Madison, Wisconsin 53706, USA

(Dated: March 15, 2011)

We study the processes $e^+e^- \rightarrow K^+K^-\pi^+\pi^-\gamma$, $K^+K^-\pi^0\pi^0\gamma$, and $K^+K^-K^+K^-\gamma$, where the photon is radiated from the initial state. About 84000, 8000, and 4200 fully reconstructed events, respectively, are selected from 454 fb⁻¹ of BABAR data. The invariant mass of the hadronic final state defines the e^+e^- center-of-mass energy, so that the $K^+K^-\pi^+\pi^-\gamma$ data can be compared with direct measurements of the $e^+e^- \rightarrow K^+K^-\pi^+\pi^-$ reaction. No direct measurements exist for the $e^+e^- \rightarrow K^+K^-\pi^0\pi^0$ or $e^+e^- \rightarrow K^+K^-K^+K^-$ reactions, and we present an update of our previous result with doubled statistics. Studying the structure of these events, we find contributions from a number of intermediate states, and extract their cross sections. In particular, we perform a more detailed study of the $e^+e^- \rightarrow \phi(1020)\pi\pi\gamma$ reaction, and confirm the presence of the $Y(2175)$ resonance in the $\phi(1020)f_0(980)$ and $K^+K^-f_0(980)$ modes. In the charmonium region, we observe the J/ψ in all three final states and in several intermediate states, as well as the $\psi(2S)$ in some modes, and measure the corresponding branching fractions.

PACS numbers: 13.66.Bc, 14.40.-n, 13.25.Jx

I. INTRODUCTION

Electron-positron annihilation at fixed center-of-mass (c.m.) energies has long been a mainstay of research in elementary particle physics. The idea of utilizing initial-state radiation (ISR) to explore e^+e^- reactions below the nominal c.m. energies was outlined in Ref. [1], and

discussed in the context of high-luminosity ϕ and B factories in Refs. [2–4]. At high c.m. energies, e^+e^- annihilation is dominated by quark-level processes producing two or more hadronic jets. Low multiplicity processes dominate below or around 2 GeV, and the region near charm threshold, 3.0–4.5 GeV, features a number of resonances [5]. These allow us to probe a wealth of physics topics, including cross sections, spectroscopy and form factors. Charmonium and other states with $J^{PC} = 1^{--}$ can be observed, and intermediate states may contribute to the final state hadronic system. Measurements of their decay modes and branching fractions are important to an understanding of the nature of such states.

Of particular current interest (see Ref. [6]) is the $Y(2175)$ state observed to decay to $\phi(1020)f_0(980)$ in our previous study [7] and confirmed by the BES [8] and

*Now at Temple University, Philadelphia, Pennsylvania 19122, USA

†Also with Università di Perugia, Dipartimento di Fisica, Perugia, Italy

‡Now at University of South Alabama, Mobile, Alabama 36688, USA

§Also with Università di Sassari, Sassari, Italy

Belle [9] Collaborations. With twice the integrated luminosity (compared to Ref. [7]) in the present analysis, we perform a more detailed study of this structure.

The study of $e^+e^- \rightarrow$ hadrons reactions in data is also critical to hadronic-loop corrections to the muon magnetic anomaly, $a_\mu = (g_\mu - 2)/2$. The theoretical predictions of this anomaly rely on these measurements [10]. Improving this prediction requires not only more precise measurements, but also measurements from threshold to the highest c.m. energy possible. In addition, all the important subprocesses should be studied in order to properly incorporate possible acceptance effects. Events produced via ISR at B factories provide independent and contiguous measurements of hadronic cross sections from the production threshold to c.m. energy of ~ 5 GeV. With more data we also are able to reduce systematic uncertainties in the cross section measurements.

The cross section for the radiation of a photon of energy E_γ in the c.m. frame, followed by the production of a particular hadronic final state f , is related to the corresponding direct $e^+e^- \rightarrow f$ cross section $\sigma_f(s)$ by

$$\frac{d\sigma_{\gamma f}(s_0, x)}{dx} = W(s_0, x) \cdot \sigma_f(s_0(1-x)), \quad (1)$$

where $\sqrt{s_0}$ is the nominal e^+e^- c.m. energy, $x = 2E_\gamma/\sqrt{s_0}$ is the fraction of the beam energy carried by the ISR photon and $E_{\text{c.m.}} \equiv \sqrt{s_0(1-x)} \equiv \sqrt{s}$ is the effective c.m. energy at which the final state f is produced. The probability density function $W(s_0, x)$ for ISR photon emission has been calculated with better than 1% precision (see, e.g. Ref. [4]). It falls rapidly as E_γ increases from zero, but has a long tail, which combines with the increasing $\sigma_f(s_0(1-x))$ to produce a sizable event rate at very low $E_{\text{c.m.}}$. The angular distribution of the ISR photon peaks along the beam directions, but 10–15% [4] of the photons are within a typical detector acceptance.

Experimentally, the measured invariant mass of the hadronic final state defines $E_{\text{c.m.}}$. An important feature of ISR data is that a wide range of energies is scanned continuously in a single experiment, so that no structure is missed, and the relative normalization uncertainties in data from different experiments are avoided. Furthermore, for large values of x the hadronic system is collimated, reducing acceptance issues and allowing measurements down to production threshold. The mass resolution is not as good as the typical beam energy spread used in direct measurements, but resolution and absolute energy scale can be monitored by means of the measured values of the width and mass of well-known resonances, such as the J/ψ produced in the reaction $e^+e^- \rightarrow J/\psi\gamma$. Backgrounds from $e^+e^- \rightarrow$ hadrons events at the nominal $\sqrt{s_0}$ and from other ISR processes can be suppressed by a combination of particle identification and kinematic fitting techniques. Studies of $e^+e^- \rightarrow \mu^+\mu^-\gamma$ and several multi-hadron ISR processes using *BABAR* data have been performed [7, 11–17], demonstrating the viability of such measurements. These analyses have led to improvements in background reduction procedures for more rare

ISR processes.

The $K^+K^-\pi^+\pi^-$ final state has been measured directly by the DM1 Collaboration [18] for $\sqrt{s} < 2.2$ GeV, and we have previously published ISR measurements of the $K^+K^-\pi^+\pi^-$ and $K^+K^-K^+K^-$ final states [13] for $E_{\text{c.m.}} < 4.5$ GeV. Later we reported an updated measurement of the $K^+K^-\pi^+\pi^-$ final state with a larger data sample, together with the first measurement of the $K^+K^-\pi^0\pi^0$ final state, in which we observed a structure near threshold in the ϕf_0 intermediate state [7].

In this paper we present a more detailed study of these two final states along with an updated measurement of the $K^+K^-K^+K^-$ final state. In all cases we require the detection of the ISR photon and perform a set of kinematic fits. We are able to suppress backgrounds sufficiently to study these final states from their respective production thresholds up to 5 GeV c.m. energy. In addition to measuring the overall cross sections, we study the internal structure of the final states and measure cross sections for a number of intermediate states contributing to them. We also study the charmonium region, measure several J/ψ and $\psi(2S)$ branching fractions, and set limits on other states.

II. THE *BABAR* DETECTOR AND DATASET

The data used in this analysis were collected with the *BABAR* detector at the PEP-II asymmetric-energy e^+e^- storage rings. The total integrated luminosity used is 454.2 fb^{-1} , which includes 413.1 fb^{-1} collected at the $\Upsilon(4S)$ peak, $\sqrt{s_0} = 10.58$ GeV, and 41.1 fb^{-1} collected at about $\sqrt{s_0} = 10.54$ GeV.

The *BABAR* detector is described elsewhere [19]. In the present work, we use charged-particle tracks reconstructed in the tracking system, which is comprised of the five double-sided-layer silicon vertex tracker (SVT) and the 40-layer drift chamber (DCH) in a 1.5 T axial magnetic field. Separation of charged pions, kaons, and protons is achieved using a combination of Cherenkov angles measured in the detector of internally reflected Cherenkov light (DIRC) and specific ionization measurements in the SVT and DCH. For the present study we use a kaon identification algorithm that provides 90–95% efficiency, depending on momentum, and pion and proton rejection factors in the 20–100 range. Photon and electron energies are measured in the CsI(Tl) electromagnetic calorimeter (EMC). We use muon identification provided by the instrumented flux return (IFR) to select the $\mu^+\mu^-\gamma$ final state used for photon efficiency studies.

To study the detector acceptance and efficiency, we use a simulation package developed for radiative processes. The simulation of hadronic final states, including $K^+K^-\pi^+\pi^-\gamma$, $K^+K^-\pi^0\pi^0\gamma$ and $K^+K^-K^+K^-$, is based on the approach suggested by Czyż and Kühn [20]. Multiple soft-photon emission from the initial-state charged particles is implemented with a structure-function technique [21, 22], and photon radiation from

the final-state particles is simulated by the PHOTOS package [23]. The precision of the radiative corrections is about 1%.

We simulate the two $K^+K^-\pi\pi$ ($\pi^+\pi^-, \pi^0\pi^0$) final states uniformly in phase space, and also according to models that include the $\phi(1020) \rightarrow K^+K^-$ and/or $f_0(980) \rightarrow \pi\pi$ channels. The $K^+K^-K^+K^-$ final state is simulated according to phase space, and also including the $\phi \rightarrow K^+K^-$ channel. The generated events are subjected to a detailed detector simulation [24], and we reconstruct them with the same software chain used for the experimental data. Variations in detector and background conditions over the course of the experiment are taken into account.

We also generate a large number of potential background processes, including the ISR reactions $e^+e^- \rightarrow \pi^+\pi^-\pi^+\pi^-\gamma$, $e^+e^- \rightarrow \pi^+\pi^-\pi^0\pi^0\gamma$, and $e^+e^- \rightarrow K_S^0K\pi\gamma$, which can contribute due to particle misidentification. We also simulate $e^+e^- \rightarrow \phi\eta\gamma$, $e^+e^- \rightarrow \phi\pi^0\gamma$, and $e^+e^- \rightarrow \pi^+\pi^-\pi^0\gamma$, which have larger cross sections and can contribute background via missing or spurious tracks or photons. In addition, we study non-ISR backgrounds resulting from $e^+e^- \rightarrow q\bar{q}$ ($q = u, d, s, c$) generated using JETSET [25] and from $e^+e^- \rightarrow \tau^+\tau^-$ generated using KORALB [26]. The cross sections for these processes are known to about 10% precision or better, which is sufficient for these measurements, and a special normalization procedure is also developed. The contribution from $\Upsilon(4S)$ decays is found to be negligible.

III. EVENT SELECTION AND KINEMATIC FIT

In the selection of candidate events, we consider photon candidates in the EMC with energy above 0.03 GeV, and charged-particle tracks reconstructed in either or both of the DCH and SVT, that extrapolate within 0.25 cm of the collision axis in the transverse plane and within 3 cm of the nominal collision point along this axis. We require a photon with c.m. energy $E_\gamma > 3$ GeV in each event, and either four charged-particle tracks with zero net charge and total momentum roughly (within 0.3 radians) opposite to the photon direction, or two oppositely charged tracks that combine with other photons to roughly balance the high-energy photon momentum. We assume that the photon with the largest value of E_γ is the ISR photon. We fit the set of charged-particle tracks to a common vertex and use this as the point of origin in calculating the photon direction(s). If additional well-reconstructed tracks exist, the nearest four (two) to the interaction region are chosen for the four-track (two-track) analysis. Most events contain additional soft photons due to machine background or interactions in the detector material.

We subject each candidate event to a set of constrained kinematic fits and use the fit results, along with charged-particle identification, both to select the final states of interest and to measure backgrounds from other processes.

The kinematic fits use the ISR photon direction and energy along with the four-momenta and covariance matrices of the initial e^+e^- and the set of selected tracks and photons. The ISR photon energy and position are additionally aligned and calibrated using the $\mu^+\mu^-\gamma$ ISR process, since the two well-identified muons predict precisely the position and energy of the photon. This process is also used to identify and measure data - Monte Carlo (MC) simulation differences in the photon detection efficiency and resolution. The fitted three-momentum for each charged-particle track and the photon are used in further kinematical calculations.

For the four-track event candidates the fits have four constraints (4C). We first fit to the $\pi^+\pi^-\pi^+\pi^-$ hypothesis, obtaining the chi-squared value $\chi_{4\pi}^2$. If the four tracks include one identified K^+ and one identified K^- , we fit to the $K^+K^-\pi^+\pi^-$ hypothesis and retain the event as a $K^+K^-\pi^+\pi^-$ candidate. For events with one identified kaon, we perform fits with each of the two oppositely charged tracks given the kaon hypothesis, and the combination with the lower $\chi_{2K2\pi}^2$ is retained if its value is less than $\chi_{4\pi}^2$. If the event contains three or four identified K^\pm , we fit to the $K^+K^-K^+K^-$ hypothesis and retain the event as a $K^+K^-K^+K^-$ candidate with chi-squared value χ_{4K}^2 .

For the events with two charged-particle tracks and five or more photon candidates, we require that both tracks be identified as kaons to suppress background from ISR $\pi^+\pi^-\pi^0\pi^0$ and $K^\pm K_S^0 \pi^\mp$ events. We then pair all non-ISR photon candidates and consider combinations with invariant mass within ± 30 MeV/ c^2 of the π^0 mass [5] as π^0 candidates. We perform a six-constraint (6C) fit to each set of two non-overlapping π^0 candidates, the ISR photon, the two charged-particle tracks, and the beam particles. Both π^0 candidates are constrained to the π^0 mass, and we retain the combination with the lowest chi-squared value, $\chi_{2K2\pi^0}^2$.

IV. THE $K^+K^-\pi^+\pi^-$ FINAL STATE

A. Final Selection and Backgrounds

The $\chi_{2K2\pi}^2$ distribution in data for the $K^+K^-\pi^+\pi^-$ candidates is shown in Fig. 1 (points); the open histogram is the distribution for the simulated $K^+K^-\pi^+\pi^-$ events. The distributions are broader than those for a typical 4C χ^2 distribution due to higher order ISR, and the experimental distribution has contributions from background processes. The simulated distribution is normalized to the data in the region $\chi_{2K2\pi}^2 < 10$ where the relative contributions of the backgrounds and radiative corrections are small ($\approx 9\%$).

The shaded histogram in Fig. 1 represents the background from non-ISR $e^+e^- \rightarrow q\bar{q}$ events obtained from the JETSET simulation. It is dominated by events with a hard π^0 that results in a fake ISR photon. These events otherwise have kinematics similar to the signal, resulting

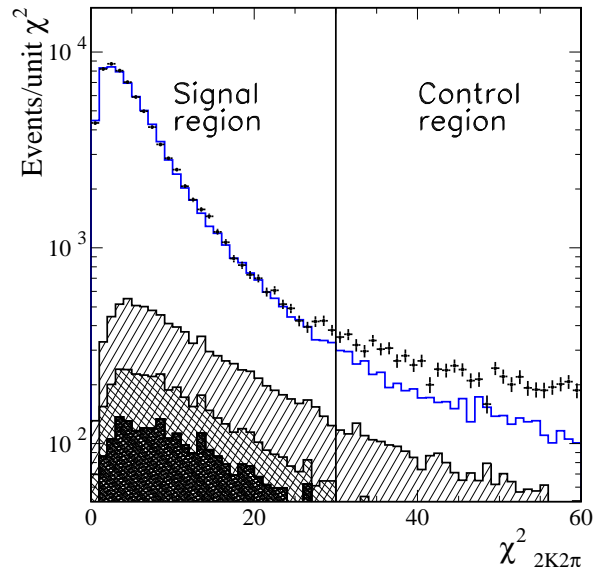


FIG. 1: Distribution of χ^2 from the four-constraint fit for $K^+K^-\pi^+\pi^-$ candidates in the data (points). The open histogram is the distribution for simulated signal events, normalized as described in the text. The shaded, cross-hatched, and hatched regions represent, respectively, the background from non-ISR events, from the ISR $K_S K \pi$ process, and backgrounds with dominant contribution from mis-identified ISR 4π events. Signal and control regions are indicated.

in the peaking structure at low values of $\chi^2_{2K2\pi}$. We evaluate this background in a number of $E_{c.m.}$ ranges by combining the ISR photon candidate with another photon candidate in both data and simulated events, and comparing the π^0 signals in the resulting $\gamma\gamma$ invariant mass distributions. The simulation gives an $E_{c.m.}$ -dependence consistent with the data, so we normalize it by an overall factor. The cross-hatched region in Fig. 1 represents $e^+e^- \rightarrow K_S K \pi \gamma$ events with $K_S \rightarrow \pi^+\pi^-$ decay close to the interaction region, and one pion mis-identified as a kaon. The process has similar kinematics to the signal process, and a contribution of about 1% is estimated using the cross section measured in our previous study [16]. The hatched region represents the contribution from ISR $e^+e^- \rightarrow \pi^+\pi^-\pi^+\pi^-$ events with one or two misidentified pions; this process contributes mainly at low χ^2 values. We estimate the contribution as a function of $E_{c.m.}$ from a simulation using the cross section value and shape from our previous study [13].

All remaining background sources are either negligible or give a $\chi^2_{2K2\pi}$ distribution that is nearly uniform over the range shown in Fig. 1. We define the signal region by requiring $\chi^2_{2K2\pi} < 30$, and estimate the sum of the remaining backgrounds from the difference between the number of data and simulated entries in the control region, $30 < \chi^2_{2K2\pi} < 60$, as we show in Fig. 1. This difference is normalized to the corresponding difference in the signal region, as described in detail in Refs. [13, 14]. The signal region contains 85598 data and 63784 simulated events; the control region contains 9684 data and 4315

simulated events.

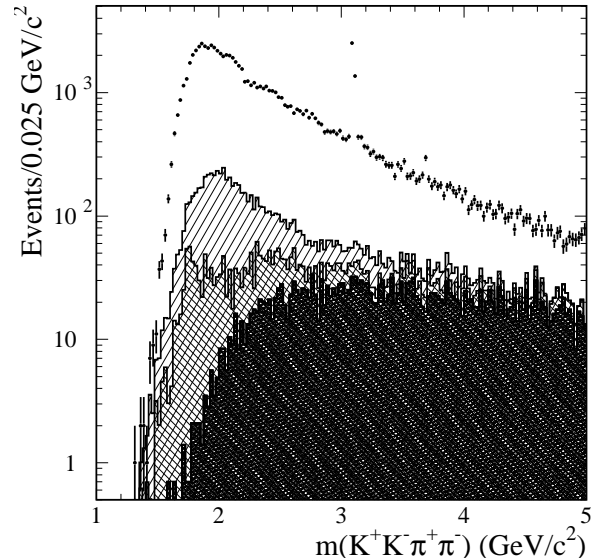


FIG. 2: The invariant mass distribution for $K^+K^-\pi^+\pi^-$ candidates in the data (points): the shaded, cross-hatched and hatched regions show, respectively, the non-ISR background from JETSET simulation, the $K_S K \pi$ background with a small contribution from the control region of Fig. 1, and the dominant contribution resulting from ISR mis-identified $\pi^+\pi^-\pi^+\pi^-$ events.

Figure 2 shows the $K^+K^-\pi^+\pi^-$ invariant mass distribution from threshold up to $5.0 \text{ GeV}/c^2$ for events in the signal region. Narrow peaks are apparent at the J/ψ and $\psi(2S)$ masses. The shaded histogram represents the $q\bar{q}$ background, which is negligible at low mass but dominates at higher masses. The cross-hatched region represents the background from the $K_S K \pi$ channel (which exhibits the peak of the $\phi(1680)$ [16]) and from the χ^2 control region. The hatched region represents the contribution from mis-identified ISR $\pi^+\pi^-\pi^+\pi^-$, and is dominant for masses below $3.0 \text{ GeV}/c^2$. The total background is 6–8% at low mass, but accounts for 20–25% of the observed distribution near $4 \text{ GeV}/c^2$ and increasing at higher masses.

We subtract the sum of backgrounds in each mass interval to obtain the number of signal events. Considering uncertainties in the cross sections for the background processes, the normalization of events in the control region, and the simulation statistics, we estimate a systematic uncertainty on the signal yield that is less than or near 2% in the $1.6\text{--}3.3 \text{ GeV}/c^2$ mass region, but increases linearly to 10% in the $3.3\text{--}5.0 \text{ GeV}/c^2$ region, and is about 20% for the masses below $1.6 \text{ GeV}/c^2$.

B. Selection Efficiency

The selection procedure applied to the data is also applied to the simulated signal samples. The resulting

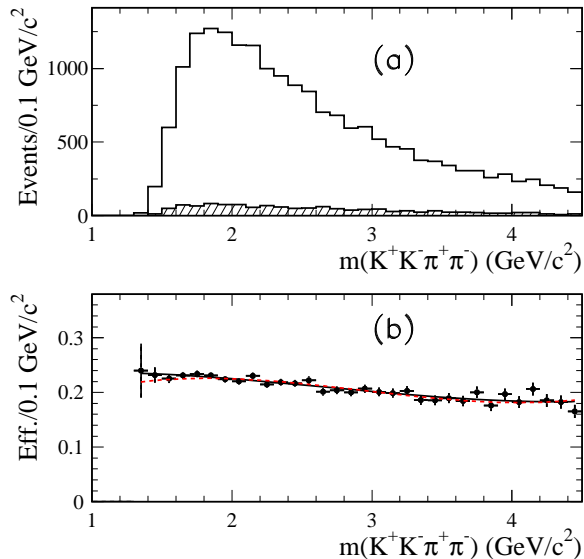


FIG. 3: (a) The invariant mass distributions for simulated uniformly in phase space $K^+K^-\pi^+\pi^-$ events, reconstructed in the signal (open) and control (hatched) regions of Fig. 1; (b) net reconstruction and selection efficiency as a function of mass obtained from this simulation (the curve represents a third-order polynomial fit). The dashed curve is obtained for the $\phi(1020)\pi^+\pi^-$ final state.

$K^+K^-\pi^+\pi^-$ invariant-mass distributions in the signal and control regions are shown in Fig. 3(a) for the uniform phase space simulation. This model reproduces the observed distributions of kaon and pion momenta and polar angles. A broad, smooth mass distribution is chosen to facilitate the estimation of the efficiency as a function of mass. We divide the number of reconstructed simulated events in each mass interval by the number generated in that interval to obtain the efficiency shown by the points in Fig. 3(b). The result of fitting a third-order polynomial to the points is used for further calculations. We simulate events with the ISR photon confined to the angular range $20\text{--}160^\circ$ with respect to the electron beam in the e^+e^- c.m. frame; wider than the actual EMC acceptance. The calculated efficiency is for this fiducial region, and includes the acceptance for the final-state hadrons, the inefficiencies of the detector subsystems, and event loss due to additional soft-photon emission.

The simulations including the $\phi(1020)\pi^+\pi^-$ and/or $K^+K^-f_0(980)$ channels give very different mass and angular distributions in the $K^+K^-\pi^+\pi^-$ rest frame. However, the angular acceptance is quite uniform for ISR events, and the efficiencies are within 1% of those from the uniform-in-phase-space simulation, as shown by the dashed curve in Fig. 3(b) for the $\phi(1020)\pi^+\pi^-$ final state.

To study possible mis-modeling of the acceptance, we repeat the analysis with tighter requirements. All charged tracks have to be within the DIRC acceptance, $0.45 < \theta_{\text{ch}} < 2.4$ radians, and the ISR photon has to be away from the edges of the EMC, $0.35 < \theta_{\text{ISR}} < 2.4$ radi-

ans. The fraction of selected data events satisfying the tighter requirements differs from the simulated ratio by 1.5%. We take the sum in quadrature of this variation and the 1% model variation (2% total) as the systematic uncertainty due to acceptance and model dependence.

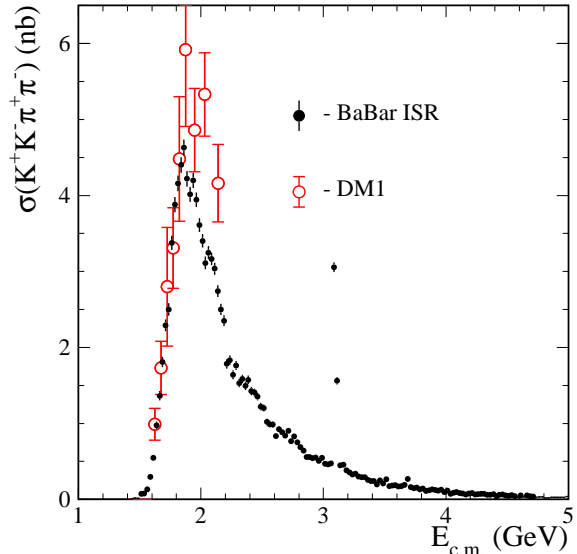


FIG. 4: The $e^+e^- \rightarrow K^+K^-\pi^+\pi^-$ cross section as a function of e^+e^- c.m. energy measured with ISR data at *BABAR* (dots). The direct measurements from DM1 [18] are shown as the open circles. Only statistical errors are shown.

Our data sample contains about 3000 events in the J/ψ peak. Comparing this number with and without selection on $\chi^2_{2K2\pi}$ we found less than a 1% difference between data and MC simulation due to mis-modeling of the shape of the $\chi^2_{2K2\pi}$ distribution. This value is taken as an estimate of the systematic uncertainty associated with the $\chi^2_{2K2\pi}$ selection criterion. To measure tracking efficiency, we consider data and simulated events that contain a high-energy photon and exactly three charged-particle tracks, which satisfy a set of kinematical criteria, including a good χ^2 from a kinematic fit to the $\pi^+\pi^-\pi^+\pi^-$ hypothesis, assuming one missing pion track in the event. We find that the simulated track-finding efficiency is overestimated by $(0.75 \pm 0.25)\%$ per track, so we apply a correction of $+(3 \pm 1)\%$ to the signal yield.

The kaon identification efficiency is studied in *BABAR* using many different test processes (e.g. $e^+e^- \rightarrow \phi(1020)\gamma \rightarrow K^+K^-\gamma$), and we conservatively estimate a systematic uncertainty of $\pm 1.0\%$ per kaon due to data-MC simulation difference in our kaon momentum range.

The data-MC simulation correction due to ISR photon detection efficiency was studied with $e^+e^- \rightarrow \mu^+\mu^-\gamma$ process and was found to be $+(1.0 \pm 0.5)\%$.

TABLE I: Summary of the cross section measurements for $e^+e^- \rightarrow K^+K^-\pi^+\pi^-$. Errors are statistical only.

$E_{c.m.}$ (GeV)	σ (nb)	$E_{c.m.}$ (GeV)	σ (nb)	$E_{c.m.}$ (GeV)	σ (nb)	$E_{c.m.}$ (GeV)	σ (nb)
1.4125	0.000 ± 0.004	2.3125	1.531 ± 0.056	3.2125	0.357 ± 0.025	4.1125	0.082 ± 0.011
1.4375	0.009 ± 0.008	2.3375	1.586 ± 0.056	3.2375	0.328 ± 0.023	4.1375	0.078 ± 0.011
1.4625	0.018 ± 0.008	2.3625	1.496 ± 0.055	3.2625	0.339 ± 0.023	4.1625	0.065 ± 0.010
1.4875	0.014 ± 0.010	2.3875	1.574 ± 0.055	3.2875	0.304 ± 0.022	4.1875	0.079 ± 0.010
1.5125	0.075 ± 0.017	2.4125	1.427 ± 0.053	3.3125	0.292 ± 0.022	4.2125	0.082 ± 0.011
1.5375	0.078 ± 0.018	2.4375	1.407 ± 0.052	3.3375	0.295 ± 0.021	4.2375	0.065 ± 0.010
1.5625	0.135 ± 0.022	2.4625	1.353 ± 0.051	3.3625	0.257 ± 0.020	4.2625	0.071 ± 0.009
1.5875	0.297 ± 0.030	2.4875	1.221 ± 0.048	3.3875	0.242 ± 0.020	4.2875	0.075 ± 0.010
1.6125	0.550 ± 0.040	2.5125	1.203 ± 0.047	3.4125	0.245 ± 0.020	4.3125	0.076 ± 0.010
1.6375	0.975 ± 0.053	2.5375	1.020 ± 0.044	3.4375	0.199 ± 0.018	4.3375	0.061 ± 0.009
1.6625	1.363 ± 0.061	2.5625	0.991 ± 0.043	3.4625	0.254 ± 0.019	4.3625	0.060 ± 0.009
1.6875	1.808 ± 0.069	2.5875	0.986 ± 0.043	3.4875	0.212 ± 0.019	4.3875	0.068 ± 0.009
1.7125	2.291 ± 0.078	2.6125	0.837 ± 0.040	3.5125	0.265 ± 0.020	4.4125	0.041 ± 0.008
1.7375	2.500 ± 0.083	2.6375	0.925 ± 0.041	3.5375	0.176 ± 0.018	4.4375	0.062 ± 0.009
1.7625	3.376 ± 0.094	2.6625	0.886 ± 0.040	3.5625	0.186 ± 0.017	4.4625	0.065 ± 0.009
1.7875	3.879 ± 0.099	2.6875	0.839 ± 0.038	3.5875	0.190 ± 0.018	4.4875	0.053 ± 0.008
1.8125	4.160 ± 0.101	2.7125	0.902 ± 0.039	3.6125	0.170 ± 0.016	4.5125	0.047 ± 0.008
1.8375	4.401 ± 0.103	2.7375	0.768 ± 0.037	3.6375	0.173 ± 0.016	4.5375	0.055 ± 0.008
1.8625	4.630 ± 0.105	2.7625	0.831 ± 0.038	3.6625	0.195 ± 0.017	4.5625	0.041 ± 0.007
1.8875	4.219 ± 0.101	2.7875	0.752 ± 0.036	3.6875	0.272 ± 0.019	4.5875	0.028 ± 0.008
1.9125	4.016 ± 0.098	2.8125	0.689 ± 0.034	3.7125	0.161 ± 0.016	4.6125	0.050 ± 0.007
1.9375	4.199 ± 0.099	2.8375	0.644 ± 0.033	3.7375	0.147 ± 0.015	4.6375	0.033 ± 0.007
1.9625	3.942 ± 0.095	2.8625	0.555 ± 0.031	3.7625	0.156 ± 0.015	4.6625	0.052 ± 0.008
1.9875	3.611 ± 0.091	2.8875	0.559 ± 0.031	3.7875	0.133 ± 0.015	4.6875	0.043 ± 0.006
2.0125	3.403 ± 0.088	2.9125	0.543 ± 0.030	3.8125	0.143 ± 0.015	4.7125	0.039 ± 0.006
2.0375	3.112 ± 0.085	2.9375	0.550 ± 0.030	3.8375	0.112 ± 0.013	4.7375	0.027 ± 0.006
2.0625	3.249 ± 0.085	2.9625	0.508 ± 0.030	3.8625	0.121 ± 0.015	4.7625	0.032 ± 0.006
2.0875	3.165 ± 0.083	2.9875	0.549 ± 0.030	3.8875	0.135 ± 0.014	4.7875	0.035 ± 0.006
2.1125	3.036 ± 0.080	3.0125	0.468 ± 0.028	3.9125	0.126 ± 0.013	4.8125	0.019 ± 0.006
2.1375	2.743 ± 0.077	3.0375	0.461 ± 0.027	3.9375	0.114 ± 0.013	4.8375	0.022 ± 0.006
2.1625	2.499 ± 0.073	3.0625	0.476 ± 0.028	3.9625	0.130 ± 0.013	4.8625	0.028 ± 0.006
2.1875	2.351 ± 0.070	3.0875	3.057 ± 0.065	3.9875	0.099 ± 0.012	4.8875	0.028 ± 0.005
2.2125	1.785 ± 0.062	3.1125	1.561 ± 0.048	4.0125	0.117 ± 0.013	4.9125	0.030 ± 0.005
2.2375	1.833 ± 0.061	3.1375	0.449 ± 0.028	4.0375	0.075 ± 0.011	4.9375	0.028 ± 0.005
2.2625	1.641 ± 0.059	3.1625	0.455 ± 0.027	4.0625	0.090 ± 0.011	4.9625	0.030 ± 0.005
2.2875	1.762 ± 0.059	3.1875	0.385 ± 0.025	4.0875	0.099 ± 0.012	4.9875	0.037 ± 0.005

C. Cross Section for $e^+e^- \rightarrow K^+K^-\pi^+\pi^-$

We calculate the $e^+e^- \rightarrow K^+K^-\pi^+\pi^-$ cross section as a function of the effective c.m. energy from

$$\sigma_{2K2\pi}(E_{c.m.}) = \frac{dN_{2K2\pi\gamma}(E_{c.m.})}{d\mathcal{L}(E_{c.m.}) \cdot \epsilon_{2K2\pi}(E_{c.m.}) \cdot R(E_{c.m.})}, \quad (2)$$

where $E_{c.m.} \equiv m_{2K2\pi}c^2$ with $m_{2K2\pi}$ the measured invariant mass of the $K^+K^-\pi^+\pi^-$ system, $dN_{2K2\pi\gamma}$ is the number of selected events after background subtraction in the interval $dE_{c.m.}$, $\epsilon_{2K2\pi}(E_{c.m.})$ is the corrected detection efficiency, and R is a radiative correction. We calculate the differential luminosity, $d\mathcal{L}(E_{c.m.})$, in each interval $dE_{c.m.}$ with the photon in the same fiducial range used for the simulation using the simple leading order (LO) formula, as described in Ref. [12]. From the mass spectra, obtained from the MC simulation with and without extra-soft-photon radiation, we extract $R(E_{c.m.})$ which gives a correction less than 1%.

From data-simulation comparison for the $e^+e^- \rightarrow \mu^+\mu^-\gamma$ events we estimate a systematic uncertainty on $d\mathcal{L}$ of 1% [17]. This $d\mathcal{L}$ has been corrected for vacuum polarization and final-state soft-photon emission; the former should be excluded when using these data in calculations of a_μ .

We show the cross section as a function of $E_{c.m.}$ in Fig. 4 with statistical errors only, and list our results in Table I. The results are consistent with the direct measurements from DM1 [18], and with our previous measurements for this reaction [7, 13], but have better statistical precision. The systematic uncertainties, summarized in Table II, affect the normalization, but have little effect on the energy dependence.

The cross section rises from threshold to a peak value of about 4.6 nb near 1.86 GeV, then generally decreases with increasing energy. In addition to narrow peaks at the J/ψ and $\psi(2S)$ mass values, there are several possible wider structures in the 1.8–2.8 GeV region. Such structures might be due to thresholds for intermediate

resonant states, such as $\phi f_0(980)$ near 2 GeV. Gaussian fits to the distributions of mass difference between generated and reconstructed MC data yield $K^+K^-\pi^+\pi^-$ mass resolution values that vary from 4.2 MeV/ c^2 in the 1.5–2.5 GeV/ c^2 region to 5.5 MeV/ c^2 in the 2.5–3.5 GeV/ c^2 region. The resolution functions are not purely Gaussian due to soft-photon radiation, but less than 10% of the signal is outside the 0.025 GeV/ c^2 mass interval used in Fig. 4. Since the cross section has no sharp structure other than the J/ψ and $\psi(2S)$ peaks discussed in Sec. IX below, we apply no correction for mass resolution.

D. Substructures in the $K^+K^-\pi^+\pi^-$ Final State

Our previous study [7, 13] showed evidence for many intermediate resonances in the $K^+K^-\pi^+\pi^-$ final state. With the larger data sample used here, these can be seen more clearly and, in some cases, studied in detail. Figure 5(a) shows a scatter plot of the invariant mass of the $K^-\pi^+$ pair versus that of the $K^+\pi^-$ pair. Signals for the $K^*(892)^0$ and $K_2^*(1430)^0$ are clearly visible. Figure 5(b) shows the $K^\pm\pi^\mp$ mass distribution (two entries per event) for all selected $K^+K^-\pi^+\pi^-$ events. We perform a fit to this distribution using P- and D-wave Breit-Wigner (BW) functions for the K^{*0} and K_2^{*0} signals, respectively, and a third-order polynomial function for the remainder of the distribution, taking into account the $K\pi$ threshold. The fit result is shown by the curves in Fig. 5(b). The fit yields a K^{*0} signal of 53997 ± 526 events with $m(K^{*0}) = 0.8932 \pm 0.0002$ GeV/ c^2 and $\Gamma(K^{*0}) = 0.0521 \pm 0.0007$ GeV, and a K_2^{*0} signal of 4361 ± 235 events with $m(K_2^{*0}) = 1.4274 \pm 0.0019$ GeV/ c^2 and $\Gamma(K_2^{*0}) = 0.0902 \pm 0.0056$ GeV. These values are consistent with current world averages [5], and the fit describes the data well, indicating that contributions from any other resonances decaying into $K^\pm\pi^\mp$ are small.

We combine K^{*0}/\bar{K}^{*0} candidates within the lines in

TABLE II: Summary of corrections and systematic uncertainties for the $e^+e^- \rightarrow K^+K^-\pi^+\pi^-$ cross section measurements. The total correction is the linear sum of the contributions, and the total uncertainty is obtained by summing the individual uncertainties in quadrature.

Source	Correction	Uncertainty
Rad. Corrections	–	1%
Backgrounds	–	2% , $E_{c.m.} < 3.3$ GeV 2-10 % , $E_{c.m.} > 3.3$ GeV
Model Acceptance	–	2%
$\chi^2_{2K2\pi}$ Distribution	–	1%
Tracking Efficiency	+3%	1%
Kaon ID Efficiency	–	2%
Photon Efficiency	+1.0%	0.5%
ISR Luminosity	–	1%
Total	+4.0%	4% , $E_{c.m.} < 3.3$ GeV 4-11% , $E_{c.m.} > 3.3$ GeV

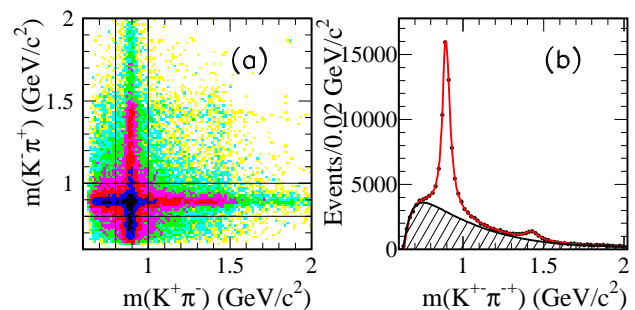


FIG. 5: (a) Invariant mass of the $K^-\pi^+$ pair versus that of the $K^+\pi^-$ pair; (b) The $K^\pm\pi^\mp$ mass distribution (two entries per event) for all selected $K^+K^-\pi^+\pi^-$ events: the solid line represents a fit including two resonances and a polynomial background function, which is shown as the hatched region.

Fig. 5(a) with the remaining pion and kaon to obtain the $K^*(892)^0\pi^\pm$ invariant mass distribution shown in Fig. 6(b), and the $K^*(892)^0\pi^\pm$ vs. $K^*(892)^0K^\mp$ mass scatter plot in Fig. 6(a). The bulk of Fig. 6(a) shows a strong positive correlation, characteristic of $K^{*0}K\pi$ final states with no higher resonances. The horizontal bands in Fig. 6(a) correspond to the peak regions of the projection plot of Fig. 6(b) and are consistent with the contribution from the $K_1(1270)$ and $K_1(1400)$ resonances. There is also an indication of a vertical band in Fig. 6(a), perhaps corresponding to a $K^*(892)^0K$ structure at ~ 1.5 GeV/ c^2 . The projection plot of Fig. 6(c) for the events with $m(K^*(892)^0\pi^\pm) > 1.5$ GeV/ c^2 shows the enhancement not consistent with a phase space behavior.

We now suppress $K^*(892)^0K\pi$ by considering only events outside the lines in Fig. 5(a). In Fig. 7(a) the $K^\pm\pi^+\pi^-$ invariant mass (two entries per event) shows evidence of the $K_1(1270)$ and $K_1(1400)$ resonances, both of which decay into $K\rho(770)$, although the latter decay is very weak [5]. In Fig. 7(b) we plot the $\pi^+\pi^-$ invariant mass for events with $m(K^\pm\pi^+\pi^-) > 1.3$ GeV/ c^2 . There is a strong $\rho(770) \rightarrow \pi^+\pi^-$ signal, and there are indications of additional structures in $f_0(980)$ and $f_2(1270)$ regions.

The separation of all these, and any other, intermediate states involving relatively broad resonances requires a partial wave analysis. This is beyond the scope of this paper. Instead we present the cross sections for the sum of all states that include $K^*(892)^0$, $K_2^*(1430)^0$ or $\rho(770)$ signals, and study intermediate states that include a narrow ϕ or f_0 resonance.

E. The $e^+e^- \rightarrow K^*(892)^0K\pi$, $K_2^*(1430)^0K\pi$ and $K^+K^-\rho(770)$ Cross Sections

Signals for the $K^*(892)^0$ and $K_2^*(1430)^0$ are clearly visible in the $K^\pm\pi^\mp$ mass distributions in Fig. 5(a,b). To extract the number of events with correlated production of $K^*(892)^0\bar{K}^*(892)^0$ and $K^*(892)^0\bar{K}_2^*(1430)^0 + c.c.$, we

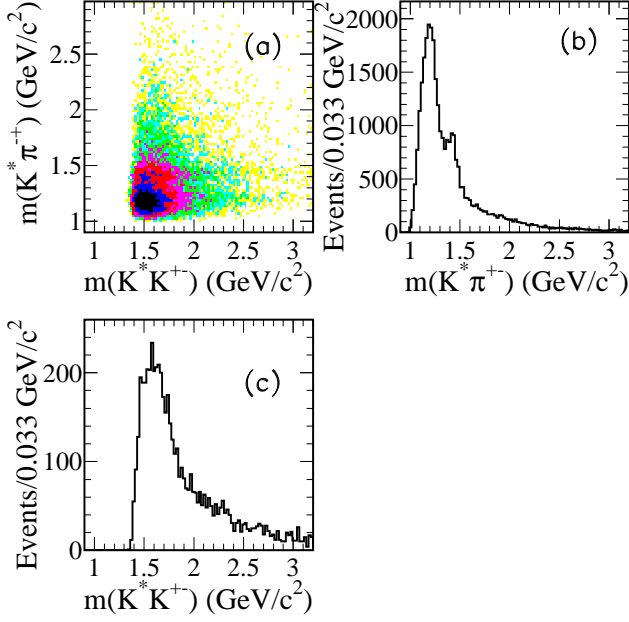


FIG. 6: (a) The $K^*(892)^0\pi^\pm$ mass versus $K^*(892)^0K^\mp$ mass scatterplot; (b) the $K^*(892)^0\pi^\pm$ projection plot of (a); (c) the $K^*(892)^0K^\mp$ projection plot of (a) for $m(K^*(892)^0\pi^\pm) > 1.5$ GeV/c^2 .

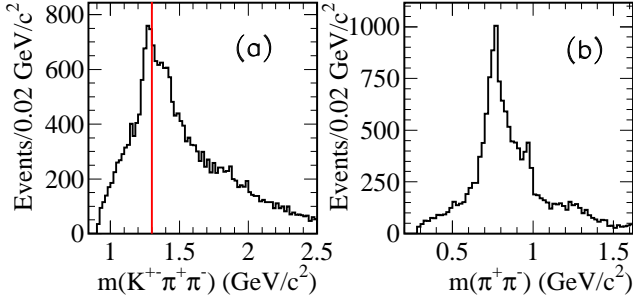


FIG. 7: (a) The invariant mass of the $K^\pm\pi^+\pi^-$ combinations with $K^*(892)^0K\pi$ events excluded; (b) the $\pi^+\pi^-$ invariant mass for events from (a) with the $K_1(1270)$ region suppressed by requiring $m(K^\pm\pi^+\pi^-) > 1.3$ GeV/c^2 as shown by vertical line in (a).

perform the same fit as that shown in Fig. 5(b), but to the $K^+\pi^-$ invariant mass distribution in each 0.04 GeV/c^2 interval of $K^-\pi^+$ invariant mass. From each fit we obtain the number of $K^*(892)^0$ and $K_2^*(1430)^0$ events and plot these values as a function of $K^+\pi^-$ mass in Fig. 8(a) and Fig. 8(b) respectively. The fit to the data of Fig. 8(a) indicates that only 548 ± 263 events are associated with correlated $\bar{K}^*(892)^0K^*(892)^0$ production (about 1% of the total number of $K^*(892)^0$ events), and that 1680 ± 343 events correspond to $\bar{K}^*(892)^0K_2^*(1430)^0$ pairs, compared to 4361 ± 235 , the total number of events with a $K_2^*(1430)^0$ in the final state. The distribution of the events from the $K_2^*(1430)^0$ peak shows a strong signal at the $\bar{K}^*(892)^0$ mass in Fig. 8(b) which con-

tains 1648 ± 32 events, in agreement with the number of $K^*(892)^0\bar{K}_2^*(1430)^0$ pairs obtained above.

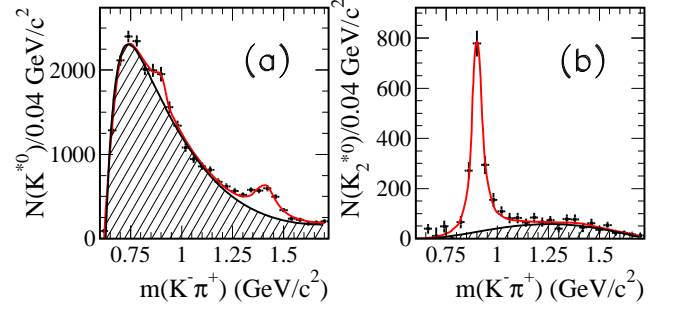


FIG. 8: The $K^-\pi^+$ invariant mass distribution corresponding to the number of $K^*(892)^0$ (a) and $K_2^*(1430)^0$ (b) events obtained from the fits to the $K^+\pi^-$ invariant mass distribution for each interval of $K^-\pi^+$ mass. The curves result from the fits described in the text.

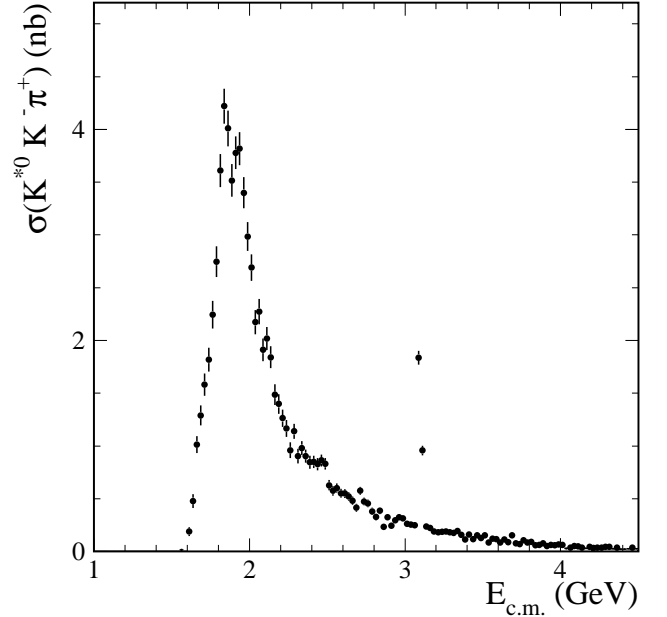


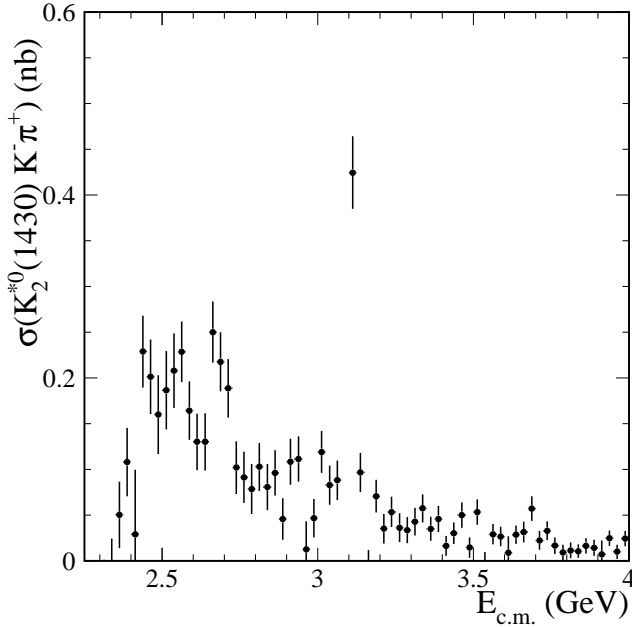
FIG. 9: The $e^+e^- \rightarrow K^*(892)^0K^-\pi^+$ cross section, obtained from the $K^*(892)^0$ signal of Fig. 5(b).

We perform a fit similar to that shown in Fig. 5(b) to the data in intervals of $K^+K^-\pi^+\pi^-$ invariant mass, with the resonance masses and widths fixed to the values obtained from the overall fit. Since correlated K^* production is small, we convert the resulting K^* yield in each interval into a cross section value for $e^+e^- \rightarrow K^*(892)^0K^-\pi^+$ or $K_2^*(1430)^0K^-\pi^+$, following the procedure described in Sec. IV C. These cross section values

¹ The use of charge conjugate reactions is implied throughout the paper

TABLE III: Summary of the cross section measurements for $e^+e^- \rightarrow K^{*0}(892)K^-\pi^+$. Errors are statistical only.

$E_{c.m.}$ (GeV)	σ (nb)	$E_{c.m.}$ (GeV)	σ (nb)	$E_{c.m.}$ (GeV)	σ (nb)	$E_{c.m.}$ (GeV)	σ (nb)
1.5875	0.00 ± 0.00	2.1875	1.40 ± 0.09	2.7875	0.38 ± 0.03	3.3875	0.11 ± 0.02
1.6125	0.19 ± 0.04	2.2125	1.26 ± 0.08	2.8125	0.33 ± 0.03	3.4125	0.16 ± 0.02
1.6375	0.48 ± 0.07	2.2375	1.17 ± 0.08	2.8375	0.39 ± 0.03	3.4375	0.12 ± 0.02
1.6625	1.01 ± 0.08	2.2625	0.96 ± 0.07	2.8625	0.24 ± 0.03	3.4625	0.15 ± 0.02
1.6875	1.29 ± 0.10	2.2875	1.14 ± 0.07	2.8875	0.32 ± 0.03	3.4875	0.13 ± 0.02
1.7125	1.58 ± 0.11	2.3125	0.90 ± 0.07	2.9125	0.24 ± 0.03	3.5125	0.15 ± 0.02
1.7375	1.82 ± 0.11	2.3375	0.98 ± 0.07	2.9375	0.30 ± 0.03	3.5375	0.08 ± 0.01
1.7625	2.24 ± 0.13	2.3625	0.90 ± 0.06	2.9625	0.33 ± 0.03	3.5625	0.12 ± 0.01
1.7875	2.75 ± 0.15	2.3875	0.85 ± 0.06	2.9875	0.31 ± 0.03	3.5875	0.12 ± 0.01
1.8125	3.61 ± 0.16	2.4125	0.85 ± 0.06	3.0125	0.26 ± 0.03	3.6125	0.09 ± 0.01
1.8375	4.22 ± 0.17	2.4375	0.83 ± 0.06	3.0375	0.26 ± 0.03	3.6375	0.12 ± 0.02
1.8625	4.01 ± 0.17	2.4625	0.86 ± 0.06	3.0625	0.25 ± 0.02	3.6625	0.09 ± 0.01
1.8875	3.52 ± 0.15	2.4875	0.83 ± 0.05	3.0875	1.84 ± 0.06	3.6875	0.15 ± 0.02
1.9125	3.78 ± 0.15	2.5125	0.63 ± 0.05	3.1125	0.96 ± 0.05	3.7125	0.08 ± 0.01
1.9375	3.82 ± 0.16	2.5375	0.58 ± 0.05	3.1375	0.24 ± 0.02	3.7375	0.07 ± 0.01
1.9625	3.40 ± 0.15	2.5625	0.60 ± 0.04	3.1625	0.22 ± 0.02	3.7625	0.11 ± 0.01
1.9875	2.98 ± 0.14	2.5875	0.55 ± 0.04	3.1875	0.19 ± 0.02	3.7875	0.09 ± 0.01
2.0125	2.69 ± 0.13	2.6125	0.55 ± 0.04	3.2125	0.18 ± 0.02	3.8125	0.09 ± 0.01
2.0375	2.17 ± 0.11	2.6375	0.52 ± 0.04	3.2375	0.19 ± 0.02	3.8375	0.06 ± 0.01
2.0625	2.27 ± 0.12	2.6625	0.48 ± 0.04	3.2625	0.19 ± 0.02	3.8625	0.06 ± 0.01
2.0875	1.91 ± 0.11	2.6875	0.41 ± 0.04	3.2875	0.18 ± 0.02	3.8875	0.08 ± 0.01
2.1125	2.02 ± 0.11	2.7125	0.57 ± 0.04	3.3125	0.17 ± 0.02	3.9125	0.05 ± 0.01
2.1375	1.84 ± 0.10	2.7375	0.47 ± 0.04	3.3375	0.19 ± 0.02	3.9375	0.06 ± 0.01
2.1625	1.49 ± 0.10	2.7625	0.46 ± 0.04	3.3625	0.16 ± 0.02	3.9625	0.06 ± 0.01

FIG. 10: The $K_2^{*0}(1430)^0 K^-\pi^+$ cross section, obtained from the $K_2^{*0}(1430)^0$ signal of Fig. 5(b).

take into account only the $K\pi$ decay of the $K^*(892)^0$ and the $K_2^{*0}(1430)^0$.

Note that the $e^+e^- \rightarrow K^*(892)^0 K\pi$ ($K_2^{*0}(1430)^0 K\pi$) cross section includes a small contribution from the $K_2^{*0}(1430)^0 K\pi$ ($K^*(892)^0 K\pi$) channel, because the

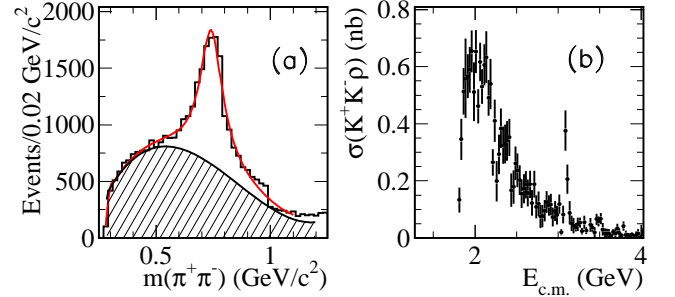


FIG. 11: (a) The $\pi^+\pi^-$ mass distribution for all selected $K^+K^-\pi^+\pi^-$ events with ϕ and K^{*0} regions excluded: the solid curve represents a fit as described in the text, and the background contribution is shown separately as the hatched region; (b) the $e^+e^- \rightarrow K^+K^-\rho(770)$ cross section obtained from the ρ signal from the fit in each 0.025 GeV c.m. energy interval.

$K_2^{*0}(1430)^0 K^*(892)^0$ final state has not been taken into account. These cross sections are shown in Fig. 9 and Fig. 10, and the $e^+e^- \rightarrow K^*(892)^0 K^-\pi^+$ channel is listed in Table III for $E_{c.m.}$ energies from threshold up to 4.0 GeV. At higher energies the signals are small and contain an unknown, but possibly large, contribution from $e^+e^- \rightarrow q\bar{q}$ events. There is a rapid rise from threshold to a peak value of about 4 nb at 1.84 GeV for the $e^+e^- \rightarrow K^*(892)^0 K^-\pi^+$ cross section, followed by a very rapid decrease with increasing energy. There are suggestions of narrow structures in the peak region, but the only statistically significant structure is the J/ψ

peak, which is discussed below. There are some structures in the $e^+e^- \rightarrow K_2^*(1430)^0 K^- \pi^+$ cross section, but the signal size is too small to make any definite statement.

The $e^+e^- \rightarrow K^*(892)^0 K^- \pi^+$ contribution is a large fraction of the total $K^+K^- \pi^+ \pi^-$ cross section at all energies above its threshold, and dominates in the 1.8–2.0 GeV region. The $K^+K^- \rho^0(770)$ intermediate state makes up the majority of the remainder of the cross section. We exclude a small ϕ contribution by requiring $|m(K^+K^-) - m(\phi)| > 0.01$ GeV/ c^2 , and suppress the large $K^*(892)^0$ contribution by means of the anti-selection $|m([K^\pm \pi^\mp] - 0.892)| > 0.035$ GeV/ c^2 . Figure 11(a) shows the $\pi^+ \pi^-$ mass distribution for the remaining events. We fit the $\rho(770)$ signal with a single BW (mass and width are fixed at 0.77 GeV/ c^2 and 0.15 GeV, respectively) and a polynomial background (contribution shown by the hatched area) for each 0.025 GeV c.m. energy interval. The cross section obtained is shown in Fig. 11(b), and has no significant structures except the J/ψ signal.

F. The $\phi(1020)\pi^+\pi^-$ Intermediate State

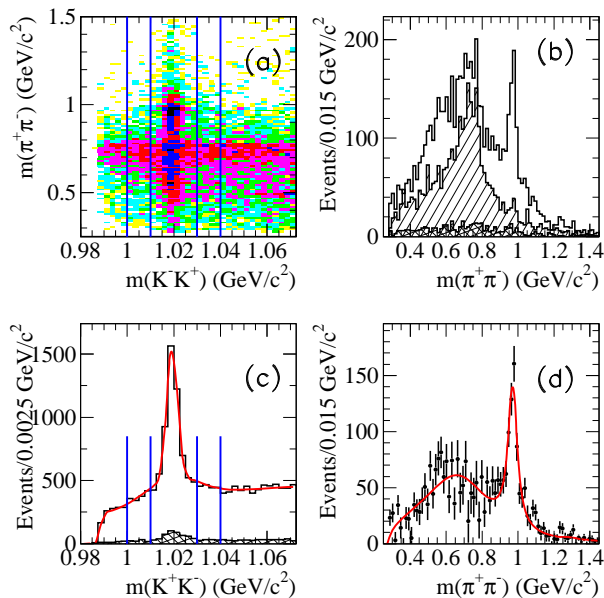


FIG. 12: (a) The $m(\pi^+\pi^-)$ vs. $m(K^+K^-)$ scatterplot for all selected $K^+K^- \pi^+ \pi^-$ events; (b) the $\pi^+ \pi^-$ invariant mass projections for events in the ϕ peak (open histogram), sidebands (hatched), and background control region (cross-hatched); (c) the K^+K^- mass projections for all events (open) and control region (cross-hatched); (d) the difference between the open histogram and the sum of the other contributions to (b).

Intermediate states containing narrow resonances can be studied more easily. For the $E_{\text{c.m.}}$ energy range below

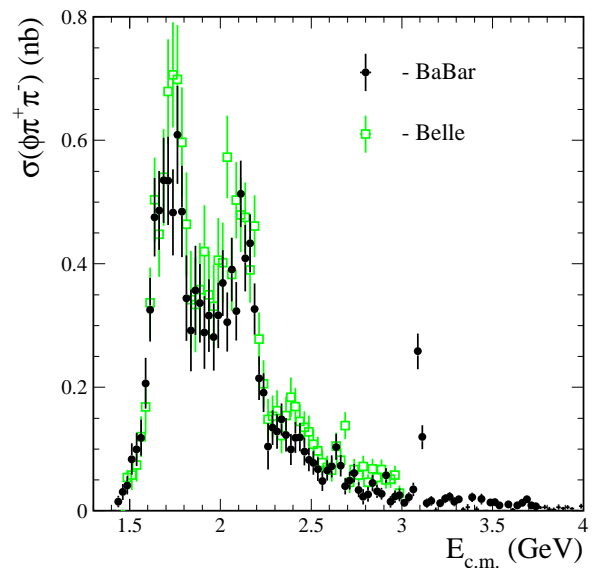


FIG. 13: The $e^+e^- \rightarrow \phi \pi^+ \pi^-$ cross section as a function of e^+e^- c.m. energy obtained by *BABAR* (dots) and *Belle* (squares) [9].

3.0 GeV, Fig. 12(a) shows a scatterplot of the invariant mass of the $\pi^+ \pi^-$ pair versus that of the K^+K^- pair. Horizontal and vertical bands corresponding to the $\rho^0(770)$ and ϕ , respectively, are visible, and there is a concentration of entries on the ϕ band corresponding to the correlated production of ϕ and $f_0(980)$, as demonstrated by the open histogram of Fig. 12(b). The ϕ signal is clearly visible in the K^+K^- mass projection of Fig. 12(c). The large contribution from the $\rho(770)$ is nearly uniform in K^+K^- mass, and the cross-hatched histogram shows the non- $K^+K^- \pi^+ \pi^-$ background estimated from the control region in $\chi^2_{2K2\pi}$. The cross-hatched histogram also shows a ϕ peak, but this is a small fraction of the events. When we subtract this background and fit the remaining data with a double-Gaussian function for ϕ signal, and a second-order polynomial function for non- ϕ background, we obtain 3951 ± 91 events corresponding to the $\phi \pi^+ \pi^-$ intermediate state.

To study the $\phi \pi^+ \pi^-$ channel, we select candidate events with a K^+K^- invariant mass within 10 MeV/ c^2 of the ϕ mass, indicated by the inner vertical lines in Figs. 12(a,c), and estimate the non- ϕ contribution from the mass sidebands between the inner and outer vertical lines. In Fig. 12(b) we show the $\pi^+ \pi^-$ invariant mass distributions for ϕ candidate events, sideband events, and χ^2 control region events as the open, hatched and cross-hatched histograms, respectively, and in Fig. 12(d) we show the $\pi^+ \pi^-$ distribution after subtracting the non- ϕ background contributions. We observe a clear, narrow peak in the $f_0(980)$ mass region, together with a broad enhancement which reaches a maximum at about 0.6 GeV/ c^2 which could indicate the $f_0(600)$ production. We defer a detailed analysis of this distribution to Secs. IV G, VII, and VIII.

TABLE IV: Summary of the cross section measurements for $e^+e^- \rightarrow \phi(1020)\pi^+\pi^-$. Errors are statistical only.

$E_{c.m.}$ (GeV)	σ (nb)	$E_{c.m.}$ (GeV)	σ (nb)	$E_{c.m.}$ (GeV)	σ (nb)	$E_{c.m.}$ (GeV)	σ (nb)
1.4875	0.04 ± 0.01	1.8375	0.29 ± 0.07	2.1875	0.33 ± 0.04	2.5375	0.07 ± 0.02
1.5125	0.08 ± 0.03	1.8625	0.36 ± 0.07	2.2125	0.21 ± 0.04	2.5625	0.05 ± 0.02
1.5375	0.10 ± 0.03	1.8875	0.34 ± 0.06	2.2375	0.19 ± 0.03	2.5875	0.07 ± 0.02
1.5625	0.12 ± 0.03	1.9125	0.29 ± 0.06	2.2625	0.10 ± 0.04	2.6125	0.07 ± 0.02
1.5875	0.21 ± 0.04	1.9375	0.32 ± 0.06	2.2875	0.13 ± 0.03	2.6375	0.10 ± 0.02
1.6125	0.33 ± 0.05	1.9625	0.28 ± 0.05	2.3125	0.13 ± 0.03	2.6625	0.07 ± 0.02
1.6375	0.48 ± 0.06	1.9875	0.32 ± 0.05	2.3375	0.15 ± 0.03	2.6875	0.04 ± 0.01
1.6625	0.49 ± 0.06	2.0125	0.37 ± 0.05	2.3625	0.12 ± 0.03	2.7125	0.05 ± 0.01
1.6875	0.54 ± 0.07	2.0375	0.31 ± 0.05	2.3875	0.10 ± 0.03	2.7375	0.06 ± 0.01
1.7125	0.53 ± 0.07	2.0625	0.39 ± 0.05	2.4125	0.12 ± 0.02	2.7625	0.03 ± 0.01
1.7375	0.48 ± 0.07	2.0875	0.32 ± 0.05	2.4375	0.12 ± 0.02	2.7875	0.02 ± 0.01
1.7625	0.61 ± 0.08	2.1125	0.51 ± 0.05	2.4625	0.10 ± 0.02	2.8125	0.03 ± 0.01
1.7875	0.48 ± 0.07	2.1375	0.41 ± 0.05	2.4875	0.08 ± 0.02	2.8375	0.04 ± 0.01
1.8125	0.34 ± 0.07	2.1625	0.43 ± 0.05	2.5125	0.08 ± 0.02	2.8625	0.03 ± 0.01

We obtain the number of $e^+e^- \rightarrow \phi\pi^+\pi^-$ events in 0.025 GeV/ c^2 intervals of $\phi\pi^+\pi^-$ invariant mass by fitting the K^+K^- invariant mass projection in that interval after subtracting non- $K^+K^-\pi^+\pi^-$ background. Each projection is a subset of Fig. 12(c), where the curve represents the fit to the full sample. In each mass interval, all parameters other than number of events in the ϕ peak are fixed to the values obtained from the overall fit.

The reconstruction efficiency may depend on the details of the production mechanism. Using the two-pion mass distribution in Fig. 12(d) as input, we simulate the $\pi^+\pi^-$ system as an S-wave composition of two structures both described by the Breit-Wigner (BW) amplitudes, with parameters set to the values obtained in Sec. VII. The BW amplitudes represent the $f_0(980)$ and the bump at 0.6 GeV/ c^2 , which we call $f_0(600)$ (see Sec. VII). We describe the $\phi\pi^+\pi^-$ mass distribution using a simple model with one resonance of mass 1.68 GeV/ c^2 and width 0.3 GeV, which decays to $\phi\pi^+\pi^-$ or $\phi f_0(980)$ when phase space allows. The reconstructed spectrum which results then has a sharp increase at about 2 GeV/ c^2 due to the $\phi f_0(980)$ threshold.

We obtain the efficiency as a function of $\phi\pi^+\pi^-$ mass by dividing the number of reconstructed events in each interval by the number generated; the result is shown in Fig. 3 by the dashed curve. Comparison with the solid curve in the same figure, shows that the model dependence is weak, giving confidence in the efficiency calculation. We calculate the $e^+e^- \rightarrow \phi\pi^+\pi^-$ cross section as described in Sec. IV C, and divide by the $\phi \rightarrow K^+K^-$ branching fraction (0.489 [5]). We show our results as a function of c.m. energy in Fig. 13, and list them in Table IV. The cross section has a peak value of about 0.6 nb at about 1.7 GeV, then decreases with increasing energy until $\phi(1020)f_0(980)$ threshold, around 2.0 GeV. From this point it rises, falls sharply at about 2.2 GeV, and then decreases slowly. Except in the charmonium region, the results at energies above 3 GeV are not meaningful due to small signals and potentially large backgrounds, and are omitted from Table IV. Figure 13 displays the

cross section up to 4.0 GeV in order to show the J/ψ and $\psi(2S)$ signals. These are discussed in Sec. IX.

The cross section obtained is in agreement with our previous measurement [7] and with results obtained by the Belle Collaboration [9], also shown in Fig. 13.

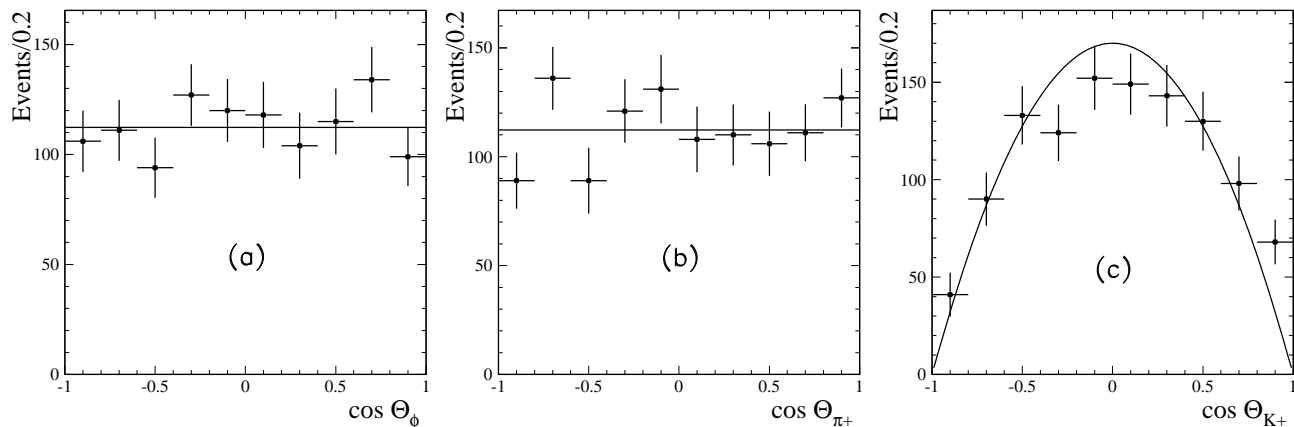
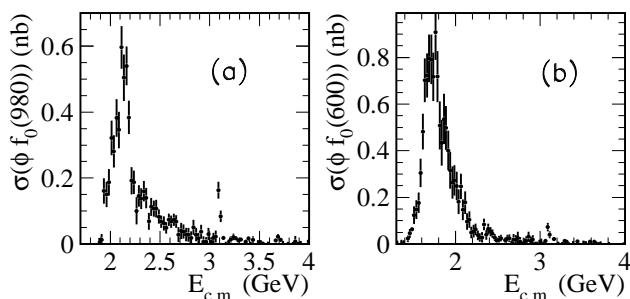
We perform a study of the angular distributions in the $\phi(1020)\pi^+\pi^-$ final state by considering all $K^+K^-\pi^+\pi^-$ candidate events with mass below 3 GeV/ c^2 in intervals of the cosine of each angle defined below, and fitting the background-subtracted K^+K^- mass projection in each interval. The efficiency is nearly uniform in the cosine of each angle, and so we study the number of events in each interval. We define the ϕ production angle, Θ_ϕ , as the angle between the ϕ direction and the ISR photon direction in the rest frame of the $\phi\pi^+\pi^-$ system (i.e. the new e^+e^- collision axis). The distribution of $\cos\Theta_\phi$, shown in Fig. 14(a), is consistent with the uniform distribution expected if the quasi-two-body final state ϕX , $X \rightarrow \pi^+\pi^-$, is produced in an S-wave angular-momentum state. We define the pion helicity angle, Θ_{π^+} , as that between the π^+ and the recoil ϕ direction in the $\pi^+\pi^-$ rest frame. The kaon helicity angle, Θ_{K^+} is defined as that between the K^+ direction and the ISR photon direction in the ϕ rest frame. The distributions of $\cos\Theta_{\pi^+}$ and $\cos\Theta_{K^+}$, shown in Figs. 14(b) and 14(c), respectively, are consistent with those expected from scalar and vector meson decays, where for the latter the ϕ retains the helicity of the virtual photon to which the ϕX system couples.

G. The $\phi(1020)f_0(980)$ and $\phi(1020)f_0(600)$ Intermediate States

The narrow $f_0(980)$ peak seen in Fig. 12(d) allows the selection of a fairly clean sample of $\phi f_0(980)$ events. We repeat the analysis just described with the additional requirement that the $\pi^+\pi^-$ invariant mass be in the range 0.85–1.10 GeV/ c^2 . A fit for this sample to the K^+K^- mass spectrum, analogous to that shown in Fig. 12(c), yields about 1350 events; all of these contain a true ϕ ,

TABLE V: Summary of the cross section measurements for $e^+e^- \rightarrow \phi(1020)f_0(980)$, $f_0(980) \rightarrow \pi\pi$. Errors are statistical only.

$E_{c.m.}$ (GeV)	σ (nb)	$E_{c.m.}$ (GeV)	σ (nb)	$E_{c.m.}$ (GeV)	σ (nb)	$E_{c.m.}$ (GeV)	σ (nb)
1.8875	0.00 ± 0.01	2.1625	0.54 ± 0.06	2.4375	0.11 ± 0.02	2.7125	0.04 ± 0.03
1.9125	0.01 ± 0.02	2.1875	0.38 ± 0.05	2.4625	0.11 ± 0.03	2.7375	0.04 ± 0.02
1.9375	0.16 ± 0.04	2.2125	0.19 ± 0.04	2.4875	0.08 ± 0.02	2.7625	0.03 ± 0.02
1.9625	0.15 ± 0.04	2.2375	0.19 ± 0.04	2.5125	0.07 ± 0.02	2.7875	0.03 ± 0.02
1.9875	0.19 ± 0.04	2.2625	0.10 ± 0.04	2.5375	0.06 ± 0.02	2.8125	0.02 ± 0.02
2.0125	0.32 ± 0.05	2.2875	0.15 ± 0.03	2.5625	0.05 ± 0.02	2.8375	0.05 ± 0.02
2.0375	0.28 ± 0.05	2.3125	0.14 ± 0.03	2.5875	0.07 ± 0.02	2.8625	0.03 ± 0.02
2.0625	0.38 ± 0.06	2.3375	0.16 ± 0.03	2.6125	0.07 ± 0.02	2.8875	0.02 ± 0.02
2.0875	0.35 ± 0.05	2.3625	0.14 ± 0.03	2.6375	0.07 ± 0.02	2.9125	0.04 ± 0.02
2.1125	0.60 ± 0.06	2.3875	0.07 ± 0.03	2.6625	0.07 ± 0.02	2.9375	0.01 ± 0.02
2.1375	0.50 ± 0.07	2.4125	0.11 ± 0.03	2.6875	0.03 ± 0.02	2.9625	0.01 ± 0.01

FIG. 14: Distributions of the cosine of (a) the ϕ production angle, (b) the pion helicity angle, and (c) the kaon helicity angle (see text) for $e^+e^- \rightarrow \phi\pi^+\pi^-$ events: the curves (normalized to the data) represent the distributions expected if the $\pi^+\pi^-$ system recoiling against the vector ϕ meson is an S-wave system produced in an S-wave orbital angular momentum state.FIG. 15: (a) The $e^+e^- \rightarrow \phi(1020)f_0(980)$, and (b) the $e^+e^- \rightarrow \phi(1020)\pi^+\pi^-$, $m(\pi^+\pi^-) < 0.85$ GeV/ c^2 cross section as a function of e^+e^- c.m. energy obtained from the $K^+K^-\pi^+\pi^-$ final state.

but about 10% are from $e^+e^- \rightarrow \phi\pi^+\pi^-$ events where the pion pair is not produced through the $f_0(980)$. By selecting events with the $\pi^+\pi^-$ invariant mass below 0.85 GeV/ c^2 , we similarly obtain a sample composed mostly of $\phi f_0(600)$ events.

We convert the above two samples of $f_0(980)$ and $f_0(600)$ events in each mass interval into measurements of the $e^+e^- \rightarrow \phi(1020)f_0(980)$ and $e^+e^- \rightarrow \phi(1020)f_0(600)$

cross sections as described above, dividing by the $f_0 \rightarrow \pi^+\pi^-$ branching fraction of two-thirds to account for $f_0 \rightarrow \pi^0\pi^0$ decay. The cross sections are shown in Fig. 15 as functions of c.m. energy and are listed in Table V and Table VI. The $\phi(1020)f_0(980)$ cross section behavior near threshold does not appear to be smooth, but is more consistent with a steep rise to a value of about 0.3 nb at 2.0 GeV followed by a slow decrease that is interrupted by a structure around 2.175 GeV. In contrast, the $\phi(1020)f_0(600)$ cross section has a smooth threshold increase to about 0.8 nb, followed by a smooth decrease thereafter. It is important to note that all structures above 2.0 GeV seen in Fig. 13 relate only to the $f_0(980)$ resonance. Possible interpretations of these structures are discussed in Sec. VIII. Again, the cross section values are not meaningful for c.m. energy above about 3 GeV, except for the J/ψ and $\psi(2S)$ signals, discussed in Sec. IX.

TABLE VI: Summary of the cross section measurements for $e^+e^- \rightarrow \phi(1020)f_0(600)$, $f_0(600) \rightarrow \pi\pi$. Errors are statistical only.

$E_{c.m.}$ (GeV)	σ (nb)	$E_{c.m.}$ (GeV)	σ (nb)	$E_{c.m.}$ (GeV)	σ (nb)	$E_{c.m.}$ (GeV)	σ (nb)
1.2875	0.00 ± 0.01	1.7125	0.79 ± 0.11	2.1375	0.10 ± 0.04	2.5625	0.00 ± 0.01
1.3125	0.01 ± 0.01	1.7375	0.72 ± 0.10	2.1625	0.10 ± 0.04	2.5875	0.02 ± 0.01
1.3375	0.00 ± 0.01	1.7625	0.91 ± 0.12	2.1875	0.05 ± 0.03	2.6125	0.03 ± 0.01
1.3625	0.01 ± 0.01	1.7875	0.72 ± 0.11	2.2125	0.05 ± 0.03	2.6375	0.03 ± 0.02
1.3875	0.01 ± 0.01	1.8125	0.51 ± 0.10	2.2375	0.06 ± 0.03	2.6625	0.01 ± 0.01
1.4125	0.00 ± 0.01	1.8375	0.43 ± 0.10	2.2625	0.04 ± 0.02	2.6875	0.02 ± 0.02
1.4375	0.02 ± 0.01	1.8625	0.54 ± 0.11	2.2875	0.03 ± 0.02	2.7125	0.02 ± 0.02
1.4625	0.05 ± 0.02	1.8875	0.50 ± 0.09	2.3125	0.03 ± 0.02	2.7375	0.03 ± 0.03
1.4875	0.06 ± 0.02	1.9125	0.40 ± 0.09	2.3375	0.08 ± 0.02	2.7625	0.01 ± 0.02
1.5125	0.12 ± 0.04	1.9375	0.32 ± 0.08	2.3625	0.04 ± 0.02	2.7875	0.00 ± 0.01
1.5375	0.15 ± 0.04	1.9625	0.26 ± 0.07	2.3875	0.06 ± 0.02	2.8125	0.01 ± 0.02
1.5625	0.18 ± 0.04	1.9875	0.27 ± 0.07	2.4125	0.05 ± 0.02	2.8375	0.01 ± 0.02
1.5875	0.31 ± 0.06	2.0125	0.25 ± 0.06	2.4375	0.04 ± 0.02	2.8625	0.03 ± 0.02
1.6125	0.48 ± 0.08	2.0375	0.18 ± 0.05	2.4625	0.03 ± 0.01	2.8875	0.01 ± 0.02
1.6375	0.70 ± 0.09	2.0625	0.25 ± 0.05	2.4875	0.01 ± 0.01	2.9125	0.02 ± 0.02
1.6625	0.72 ± 0.09	2.0875	0.15 ± 0.05	2.5125	0.02 ± 0.01	2.9375	0.00 ± 0.01
1.6875	0.80 ± 0.10	2.1125	0.18 ± 0.05	2.5375	0.03 ± 0.01	2.9625	0.00 ± 0.01

V. THE $K^+K^-\pi^0\pi^0$ FINAL STATE

A. Final Selection and Backgrounds

The $K^+K^-\pi^0\pi^0$ sample contains background from the ISR processes $e^+e^- \rightarrow K^+K^-\pi^0\gamma$ and $K^+K^-\eta\gamma$, in which two soft photon candidates from machine- or detector-related background combine with the relatively energetic photons from the π^0 or η to form two fake π^0 candidates. We reduce this background using the angle between each reconstructed π^0 direction and the direction of its higher-energy photon daughter calculated in the π^0 rest frame. If the cosines of both angles are larger than 0.85, we remove the event.

Figure 16 shows the distribution of $\chi^2_{2K2\pi^0}$ for the remaining candidates together with the simulated $K^+K^-\pi^0\pi^0$ events. Again, the distributions are broader than those for a typical 6C χ^2 distribution due to higher order ISR, and we normalize the histogram to the data in the region $\chi^2_{2K2\pi^0} < 15$. The cross-hatched histogram in Fig. 16 represents background from $e^+e^- \rightarrow q\bar{q}$ events, evaluated in the same way as for the $K^+K^-\pi^+\pi^-$ final state. The hatched region represents the ISR backgrounds from final states with similar kinematics. The first of these is $\pi^+\pi^-\pi^0\pi^0$, which yields events with both charged pions misidentified as kaons, and the second is the $K_S K\pi$, which yields $K_S \rightarrow \pi^0\pi^0$ and a misidentified pion. Each contribution is small.

The dominant background in this case is from residual ISR $K^+K^-\pi^0$ and $K^+K^-\eta$ events, as well as ISR-produced $K^+K^-\pi^0\pi^0\pi^0$ events. Their net simulated contribution, indicated by the dashed contour in Fig. 16, is consistent with the data in the high $\chi^2_{2K2\pi^0}$ region. All other backgrounds are either negligible or distributed uniformly in $\chi^2_{2K2\pi^0}$. We define the signal region by $\chi^2_{2K2\pi^0} < 50$, which contains 7967 data and 7402 simulated events, and a control region by $50 < \chi^2_{2K2\pi^0} <$

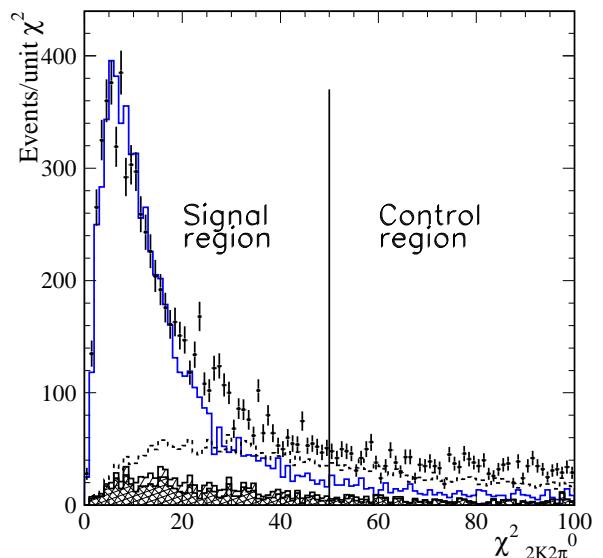


FIG. 16: Distribution of χ^2 from the six-constraint fits to $K^+K^-\pi^0\pi^0$ candidates in the data (points). The open histogram is the distribution for simulated signal events, normalized as described in the text. The cross-hatched, hatched, and dashed regions represent, respectively, the backgrounds from non-ISR $q\bar{q}$ events, ISR-produced $\pi^+\pi^-\pi^0\pi^0$ and $K_S K\pi$ events, and ISR-produced $K^+K^-\pi^0$, $K^+K^-\eta$ and $K^+K^-\pi^0\pi^0\pi^0$ events.

100, which contains 2007 data and 704 simulated signal events.

Figure 17 shows the $K^+K^-\pi^0\pi^0$ invariant mass distribution from threshold up to 5 GeV/c^2 for events in the signal region. The $q\bar{q}$ background (cross-hatched histogram) is negligible at low masses but yields a significant fraction of the selected events above about 4 GeV/c^2 . The ISR $\pi^+\pi^-\pi^0\pi^0$ contribution (hatched region) is negligible except in the 1.5–2.5 GeV/c^2 region. The sum of

all other backgrounds, estimated from the control region, is the dominant contribution below $2.5 \text{ GeV}/c^2$ and is non-negligible everywhere. The total background varies from 100% below $1.6 \text{ GeV}/c^2$ to 25% at higher masses.

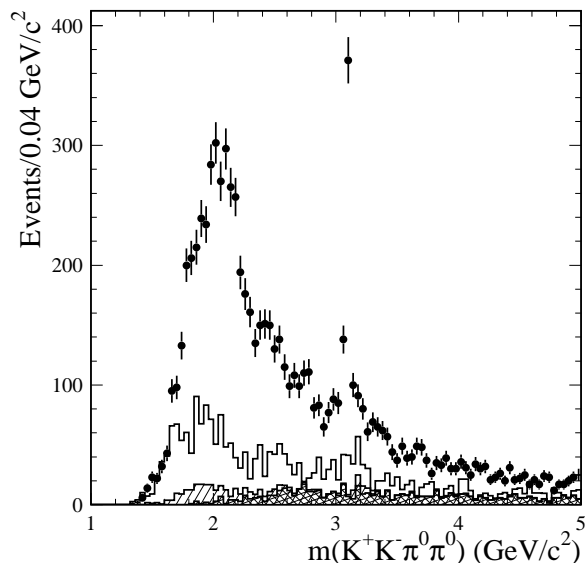


FIG. 17: Invariant mass distribution for $K^+K^-\pi^0\pi^0$ candidates in the signal region for data (points). The cross-hatched, hatched, and open regions represent, respectively, the non-ISR $q\bar{q}$ background, the contribution from ISR-produced $\pi^+\pi^-\pi^0\pi^0$ and $K_S K\pi$ events, and the contribution from the other ISR processes described in the text.

We subtract the sum of the estimated background contributions from the number of selected events in each mass interval to obtain the number of signal events. Considering uncertainties in the cross sections for the background processes, the normalization of events in the control region and the simulation statistics, we estimate a systematic uncertainty on the signal yield after background subtraction of about 5% in the $1.6\text{--}3.0 \text{ GeV}/c^2$ region; this increases linearly from 5% to 15% in the region above $3 \text{ GeV}/c^2$.

B. Selection Efficiency

The detection efficiency is determined in the same manner as in Sec. IV B. Figure 18(a) shows the simulated $K^+K^-\pi^0\pi^0$ invariant mass distributions in the signal and control regions obtained from the phase space model. We divide the number of reconstructed events in each $0.04 \text{ GeV}/c^2$ mass interval by the number generated in that interval to obtain the efficiency estimate shown by the points in Fig. 18(b); a third-order-polynomial fit to the efficiency is used in calculating the cross section. Again, the simulation of the ISR photon covers a limited angular range, which is about 30% wider than the EMC acceptance. Simulations assuming dominance of the $\phi \rightarrow K^+K^-$ and/or the $f_0 \rightarrow \pi^0\pi^0$ channels give re-

sults consistent with those of Fig. 18(b), and we apply a 3% systematic uncertainty for possible model dependence, as in Sec. IV B.

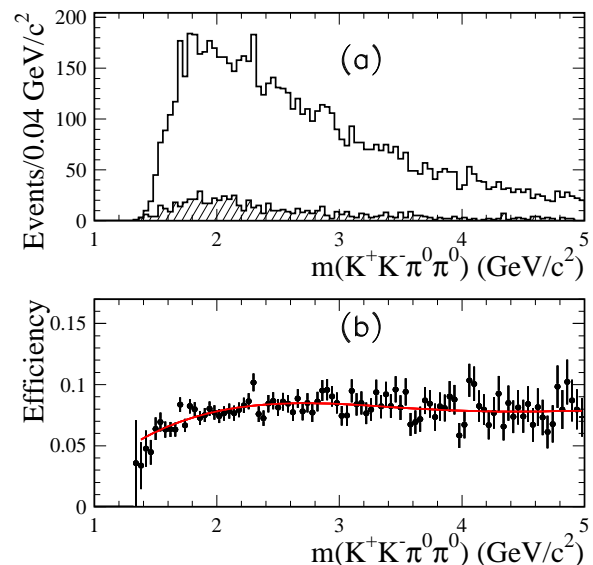


FIG. 18: (a) Invariant mass distribution for simulated $K^+K^-\pi^0\pi^0$ events in the signal (open) and control (hatched) regions (see Fig. 16); (b) net reconstruction and selection efficiency as a function of mass obtained from this simulation (the curve represents the result of a third-order-polynomial fit).

We correct for mis-modeling of the track-finding and kaon identification efficiencies as in Sec. IV B ($+1.9 \pm 0.6\%$ and $0 \pm 2.0\%$ corrections, respectively). We do not see any large discrepancy in the shape of the $\chi^2_{2K2\pi^0}$ distribution, and so apply no correction for the $\chi^2_{2K2\pi^0} < 50$ selection, but introduce 3% as an associated systematic uncertainty. We correct the π^0 -finding efficiency using the procedure described in detail in Ref. [14]. From ISR $e^+e^- \rightarrow \omega\pi^0\gamma \rightarrow \pi^+\pi^-\pi^0\pi^0\gamma$ events selected with and without the π^0 from the ω decay, we find that the simulated efficiency for one π^0 is too large by $(3.0 \pm 1.0)\%$. Conservatively, we apply a correction of $(+6.0 \pm 2.0)\%$ because of the two π^0 s in each event.

C. Cross Section for $e^+e^- \rightarrow K^+K^-\pi^0\pi^0$

We calculate the cross section for $e^+e^- \rightarrow K^+K^-\pi^0\pi^0$ in 0.04 GeV $E_{c.m.}$ intervals from the analog of Eq.(2), using the invariant mass of the $K^+K^-\pi^0\pi^0$ system to determine the c.m. energy. We show the results in Fig. 19 and list the values and statistical errors in Table VII. The cross section rises to a peak value near 0.8 nb at 2 GeV then shows a rapid decrease, which is interrupted by a large J/ψ signal; the charmonium region is discussed in Sec. IX below. The drop at 2.2 GeV is similar to that seen for the $K^+K^-\pi^+\pi^-$ final state. Again, the differential luminosity includes corrections for vacuum polar-

TABLE VII: Summary of the cross section measurements for $e^+e^- \rightarrow K^+K^-\pi^0\pi^0$. Errors are statistical only.

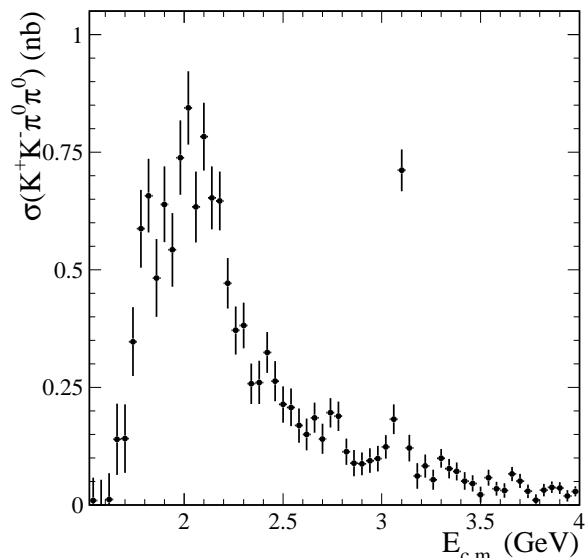
$E_{c.m.}$ (GeV)	σ (nb)	$E_{c.m.}$ (GeV)	σ (nb)	$E_{c.m.}$ (GeV)	σ (nb)	$E_{c.m.}$ (GeV)	σ (nb)
1.5000	0.00 ± 0.04	2.1400	0.65 ± 0.07	2.7800	0.19 ± 0.03	3.4200	0.05 ± 0.02
1.5400	0.01 ± 0.05	2.1800	0.65 ± 0.06	2.8200	0.11 ± 0.03	3.4600	0.05 ± 0.02
1.5800	0.00 ± 0.05	2.2200	0.47 ± 0.05	2.8600	0.09 ± 0.03	3.5000	0.02 ± 0.02
1.6200	0.01 ± 0.06	2.2600	0.37 ± 0.05	2.9000	0.09 ± 0.02	3.5400	0.06 ± 0.02
1.6600	0.14 ± 0.08	2.3000	0.38 ± 0.05	2.9400	0.09 ± 0.03	3.5800	0.04 ± 0.01
1.7000	0.14 ± 0.07	2.3400	0.26 ± 0.04	2.9800	0.10 ± 0.03	3.6200	0.03 ± 0.02
1.7400	0.35 ± 0.07	2.3800	0.26 ± 0.05	3.0200	0.12 ± 0.02	3.6600	0.07 ± 0.02
1.7800	0.59 ± 0.08	2.4200	0.32 ± 0.04	3.0600	0.18 ± 0.03	3.7000	0.05 ± 0.02
1.8200	0.66 ± 0.08	2.4600	0.26 ± 0.04	3.1000	0.71 ± 0.04	3.7400	0.03 ± 0.01
1.8600	0.48 ± 0.08	2.5000	0.21 ± 0.04	3.1400	0.12 ± 0.03	3.7800	0.01 ± 0.01
1.9000	0.64 ± 0.08	2.5400	0.21 ± 0.04	3.1800	0.06 ± 0.03	3.8200	0.03 ± 0.01
1.9400	0.54 ± 0.08	2.5800	0.17 ± 0.04	3.2200	0.08 ± 0.02	3.8600	0.04 ± 0.01
1.9800	0.74 ± 0.08	2.6200	0.15 ± 0.03	3.2600	0.05 ± 0.02	3.9000	0.04 ± 0.01
2.0200	0.84 ± 0.08	2.6600	0.19 ± 0.03	3.3000	0.10 ± 0.02	3.9400	0.02 ± 0.01
2.0600	0.63 ± 0.08	2.7000	0.14 ± 0.03	3.3400	0.08 ± 0.02	3.9800	0.03 ± 0.01
2.1000	0.78 ± 0.07	2.7400	0.20 ± 0.03	3.3800	0.07 ± 0.02	4.0200	0.02 ± 0.01

TABLE VIII: Summary of corrections and systematic uncertainties for the $e^+e^- \rightarrow K^+K^-\pi^0\pi^0$ cross section measurements. The total correction is the linear sum of the contributions, and the total uncertainty is obtained by summing the individual contributions in quadrature.

Source	Correction	Uncertainty
Rad. Corrections	–	1%
Backgrounds	–	5% , $E_{c.m.} < 3$ GeV 5-15% , $E_{c.m.} > 3$ GeV
Model Dependence	–	3%
$\chi^2_{2K2\pi^0}$ Distribution	–	3%
Tracking Efficiency	+1.9%	0.6%
Kaon ID Efficiency	–	2%
π^0 Efficiency	+6%	2%
ISR-photon Efficiency	+1.0%	0.5%
ISR Luminosity	–	1%
Total	+8.9%	7% , $E_{c.m.} < 3$ GeV 7-16% , $E_{c.m.} > 3$ GeV

ization that should be omitted for calculations of a_μ .

The simulated $K^+K^-\pi^0\pi^0$ invariant mass resolution is $8.8 \text{ MeV}/c^2$ in the $1.5\text{--}2.5 \text{ GeV}/c^2$ mass range, and increases with mass to $11.2 \text{ MeV}/c^2$ in the $2.5\text{--}3.5 \text{ GeV}/c^2$ range. Since less than 20% of the events in a 0.04 GeV interval are reconstructed outside that interval, and the cross section has no sharp structure other than the J/ψ peak, we again make no correction for resolution. The point-to-point systematic uncertainties are much smaller than the statistical uncertainties, and the errors on the normalization are summarized in Table VIII, along with the corrections that were applied to the measurements. The total correction is +8.9%, and the total systematic uncertainty is 7% at low mass, increasing linearly from 7% to 16% above $3 \text{ GeV}/c^2$.

FIG. 19: The $e^+e^- \rightarrow K^+K^-\pi^0\pi^0$ cross section as a function of e^+e^- c.m. energy measured with ISR data at *BABAR*. The errors are statistical only.

D. Substructure in the $K^+K^-\pi^0\pi^0$ Final State

A scatterplot of the invariant mass of the $K^-\pi^0$ pair versus that of the $K^+\pi^0$ pair is shown in Fig. 20(a) (two entries per event) for the χ^2 signal region after removing the $\phi(1020)$ contribution by $|m(K^+K^-) - m(\phi)| > 0.01 \text{ GeV}/c^2$. Horizontal and vertical bands corresponding to the $K^*(892)^-$ and $K^*(892)^+$, respectively, are visible. Figure 20(b) shows as points the sum of the two projections of Fig. 20(a); a large $K^*(892)^\pm$ signal is evident. Fitting this distribution with the function used in Sec. IV E, we obtain the number of events corresponding to $K^*(892)^\pm$ (8234 ± 269) and $K^*(1430)^\pm$ (675 ± 90) production. The $K^*(1430)^\pm:K^*(892)^\pm$ ratio is consis-

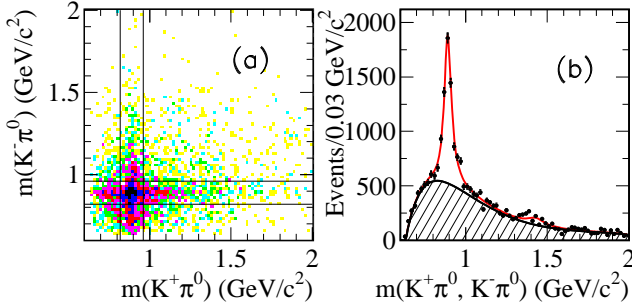


FIG. 20: (a) Invariant mass of the $K^- \pi^0$ pair versus that of the $K^+ \pi^0$ pair in selected $K^+ K^- \pi^0 \pi^0$ events (two entries per event); (b) sum of the projections of (a) (dots, four entries per event). The curves represent the result of the fit described in the text.

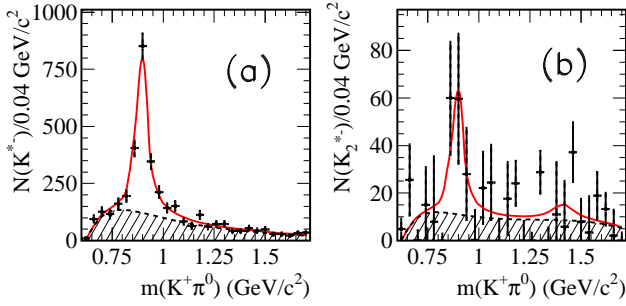


FIG. 21: The number of $K^*(892)^-$ (a) and $K_2^*(1430)^-$ (b) events obtained from the fits to the $K^- \pi^0$ invariant mass distributions for each $0.04 \text{ GeV}/c^2$ interval of $K^+ \pi^0$ mass. The curves result from the fits described in the text.

tent with that obtained for neutral K^* production in the $K^+ K^- \pi^+ \pi^-$ channel, but the number of $K^*(892)^\pm$ combinations in the peak is larger than the total number of $K^+ K^- \pi^0 \pi^0$ events (5522). This indicates the presence of some number of correlated $K^*(892)^+ K^*(892)^-$ pairs. Fitting the $K^- \pi^0$ mass distribution in each $0.04 \text{ GeV}/c^2$ bin of $K^+ \pi^0$ invariant mass, we obtain the number of $K^*(892)^-$ and $K_2^*(1430)^-$ events shown in Fig. 21(a,b). The correlated production of $K^*(892)^+ K^*(892)^-$ and $K^*(892)^+ K_2^*(1430)^-$ is clearly seen, and the fits yield 1750 ± 60 and 140 ± 49 events respectively. Note that $K^*(892)^+ K^*(892)^-$ accounts for about 30% of all $K^+ K^- \pi^0 \pi^0$ events, in contrast with the $K^+ K^- \pi^+ \pi^-$ channel, where only 548 ± 263 (less than 1%) events are found to result from the $\bar{K}^*(892)^0 K^*(892)^0$ pair production.

We find no evidence of resonance production in the $K^+ K^- \pi^0$ or $K^\pm \pi^0 \pi^0$ subsystems. Since the statistics are low in any given mass interval, we do not attempt to extract a separate $K^*(892)^+ K^- \pi^0 + c.c.$ cross section. The total $K^+ K^- \pi^0 \pi^0$ cross section is roughly a factor of four lower than the $K^*(892)^0 K^- \pi^+$ cross section observed in the $K^+ K^- \pi^+ \pi^-$ final state. This is consistent with what is expected from isospin considerations and the charged versus neutral K^* branching fractions involving charged kaons.

E. The $\phi(1020) \pi^0 \pi^0$ Intermediate State

The selection of events containing $\phi(1020) \rightarrow K^+ K^-$ decay follows that in Section IV F. Figure 22(a) shows the scatterplot of the invariant mass of the $\pi^0 \pi^0$ pair versus that of the $K^+ K^-$ pair. The ϕ resonance is visible as a vertical band, whose intensity decreases with increasing $\pi^0 \pi^0$ mass except for an enhancement in the $f_0(980)$ region (Fig. 22(b)). The ϕ signal is also visible in the $K^+ K^-$ invariant mass projection for events in the control region, shown in Fig. 22(c). The relative non- ϕ background is smaller than in the $K^+ K^- \pi^+ \pi^-$ mode, but there is a large background from ISR $\phi \pi^0$, $\phi \eta$ and/or $\phi \pi^0 \pi^0 \pi^0$ events, as indicated by the control region histogram (hatched) in Fig. 22(c). The contributions from non-ISR and ISR $\pi^+ \pi^- \pi^0 \pi^0$ events are negligible. Selecting ϕ candidate and side band events as for the $K^+ K^- \pi^+ \pi^-$ mode (vertical lines in Figs. 22(a,c)), we obtain the $\pi^0 \pi^0$ mass projections shown as the open and cross-hatched histograms, respectively, in Fig. 22(b). Control region events (hatched histogram) are concentrated at low mass values in Fig. 22(b), and a peak corresponding to the $f_0(980)$ is visible over a relatively low background.

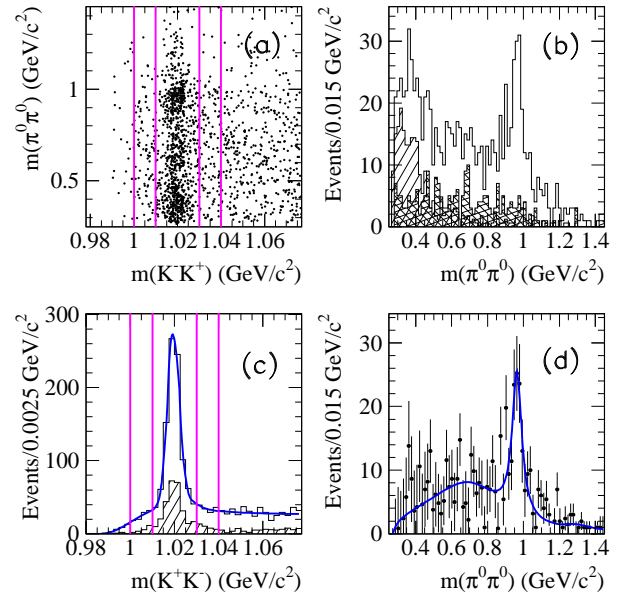


FIG. 22: (a) Scatterplot of the $\pi^0 \pi^0$ invariant mass vs. the $K^+ K^-$ invariant mass for all selected $K^+ K^- \pi^0 \pi^0$ events; (b) the $\pi^0 \pi^0$ invariant mass projections for events in the ϕ peak (open histogram), sidebands (cross-hatched), and control region (hatched); (c) the $K^+ K^-$ mass projection for events in the signal (open) and control (hatched) regions; (d) the difference between the open histogram and sum of the other contributions to (b).

In Fig. 22(d) we show the $\pi^0 \pi^0$ mass distribution associated with ϕ production after subtraction of all background contributions. The distribution is very similar to

TABLE IX: Summary of the cross section measurements for $e^+e^- \rightarrow \phi(1020)f_0(980)$, $f_0 \rightarrow \pi\pi$. Errors are statistical only.

$E_{c.m.}$ (GeV)	σ (nb)	$E_{c.m.}$ (GeV)	σ (nb)	$E_{c.m.}$ (GeV)	σ (nb)	$E_{c.m.}$ (GeV)	σ (nb)
1.9000	0.15 ± 0.07	2.1000	0.45 ± 0.11	2.3200	0.12 ± 0.06	2.9200	0.02 ± 0.01
1.9400	0.14 ± 0.06	2.1400	0.47 ± 0.11	2.4000	0.14 ± 0.03	3.0800	0.05 ± 0.01
1.9800	0.19 ± 0.09	2.1800	0.55 ± 0.10	2.4800	0.12 ± 0.03	3.2400	0.01 ± 0.01
2.0200	0.47 ± 0.11	2.2200	0.11 ± 0.05	2.6000	0.04 ± 0.01	3.4000	0.01 ± 0.00
2.0600	0.22 ± 0.08	2.2600	0.13 ± 0.05	2.7600	0.04 ± 0.01		

that of Fig. 12(d), but with a data sample which is about six times smaller.

We obtain the number of $e^+e^- \rightarrow \phi\pi^0\pi^0$ events in 0.04 GeV/ c^2 intervals of $\phi\pi^0\pi^0$ invariant mass by fitting the K^+K^- invariant mass projection in that interval to the ϕ signal, after subtracting the non- $K^+K^-\pi^0\pi^0$ background, the same way as described in Sec. IV F. The obtained cross section is shown in Fig. 23 and is very similar to that obtained from the $K^+K^-\pi^+\pi^-$ final state shown in Fig. 13. The errors shown reflect not only a six times smaller number of events, but also a much larger background level.

As before, we defer discussion to Secs. VII and VIII.

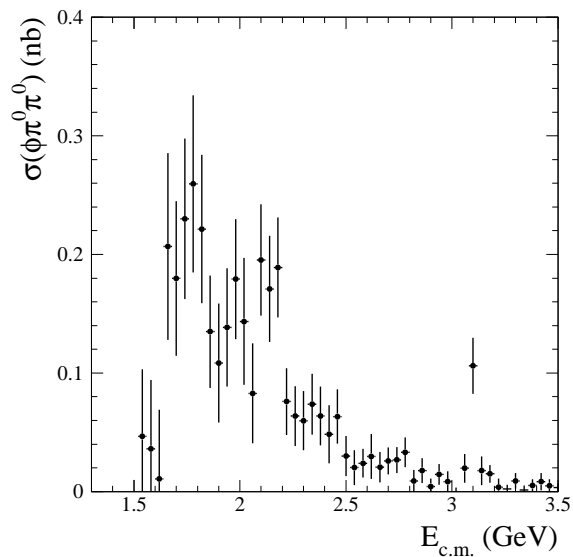


FIG. 23: Cross section for the reaction $e^+e^- \rightarrow \phi(1020)\pi^0\pi^0$ as a function of e^+e^- c.m. energy obtained from the $K^+K^-\pi^0\pi^0$ final state.

F. The $\phi(1020)f_0(980)$ Intermediate State

Since the background under the $f_0(980)$ peak in Figs. 22(b,d) is relatively small, we are able to extract the $\phi(1020)f_0(980)$ contribution. As in Sec. IV G, we require the dipion mass to be in the range 0.85–1.10 GeV/ c^2 and fit the background-subtracted K^+K^- mass projection in each 0.04 GeV/ c^2 interval of $K^+K^-\pi^0\pi^0$ mass to obtain the number of ϕf_0 events. Again, about 10% of these

are $\phi\pi^0\pi^0$ events in which the $\pi^0\pi^0$ pair is not produced through the f_0 , but this does not affect the conclusions.

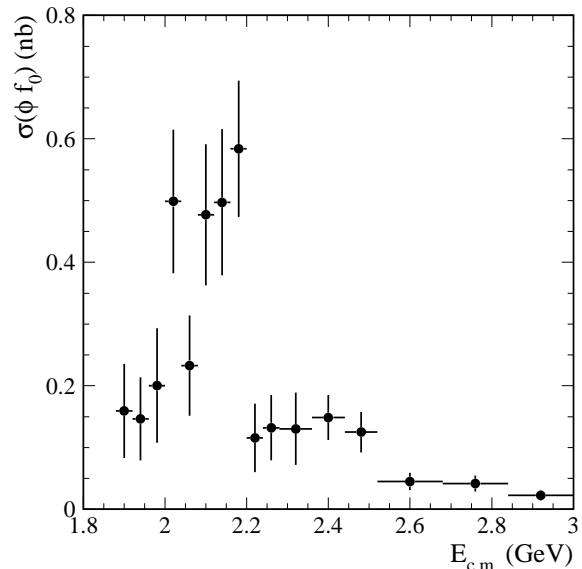


FIG. 24: Cross section for the reaction $e^+e^- \rightarrow \phi(1020)f_0(980)$, $f_0 \rightarrow \pi\pi$ as a function of e^+e^- c.m. energy obtained from the $K^+K^-\pi^0\pi^0$ final state.

We convert the number of $f_0(980)$ events in each mass interval into a measurement of the $e^+e^- \rightarrow \phi(1020)f_0(980)$ cross section as described previously, and divide by the $f_0(980) \rightarrow \pi^0\pi^0$ branching fraction of one-third to obtain the $f_0(980) \rightarrow \pi\pi$ value. The cross section, corrected for the $\phi(1020) \rightarrow K^+K^-$ decay rate, is shown in Fig. 24 as a function of $E_{c.m.}$ and is listed in Table IX. Due to the smaller number of events, we have used larger intervals at higher energies. The overall shape is consistent with that obtained from the $K^+K^-\pi^+\pi^-$ final state (see Fig. 15), and there seems to be a sharp drop near 2.2 GeV, however the statistical errors are large and no conclusion can be drawn from this mode alone. Possible interpretations are discussed in Section VIII.

VI. THE $K^+K^-K^+K^-$ FINAL STATE

A. Final Selection and Background

Figure 25 shows the distribution of χ^2_{4K} for the $K^+K^-K^+K^-$ candidates as points, and the open his-

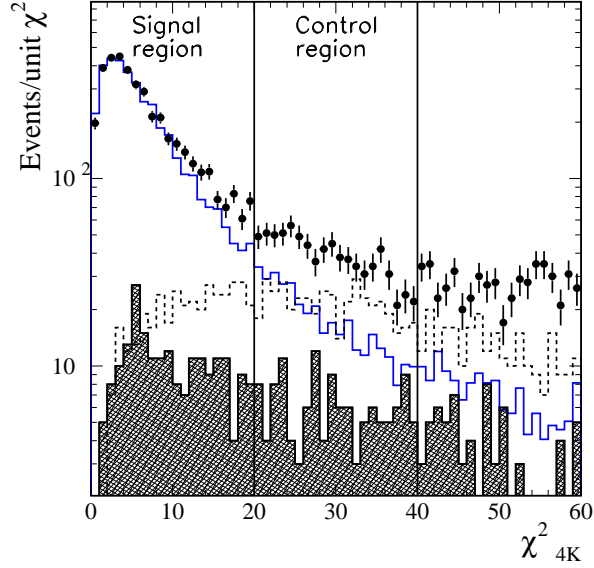


FIG. 25: Distribution of χ^2 from the three-constraint fit for $K^+K^-K^+K^-$ candidates in the data (points). The open histogram is the distribution for simulated signal events, normalized as described in the text. The shaded histogram represents the background from non-ISR events, estimated as described in the text. The region defined by the dashed contour is for simulated ISR $K^+K^-\pi^+\pi^-$ events with at least one pion misidentified as a kaon.

togram is the distribution for simulated $K^+K^-K^+K^-$ events, normalized to the data in the region $\chi_{4K}^2 < 5$ where the relative contributions of the backgrounds and radiative corrections are small. The shaded histogram represents the background from non-ISR $e^+e^- \rightarrow q\bar{q}$ events, evaluated as for the other modes. The region defined by the dashed contour represents the background from simulated ISR $K^+K^-\pi^+\pi^-$ events with at least one charged pion misidentified as a kaon.

We define signal and control regions by $\chi_{4K}^2 < 20$ and $20 < \chi_{4K}^2 < 40$, respectively. The signal region contains 4190 data and 14904 simulated events, and the control region contains 877 data and 1437 simulated events. Figure 26 shows the $K^+K^-K^+K^-$ invariant mass distribution from threshold up to $4.5 \text{ GeV}/c^2$ for events in the signal region as points with errors. The $q\bar{q}$ background (shaded histogram) is small at all masses. Since the ISR $K^+K^-\pi^+\pi^-$ background does not peak at low χ_{4K}^2 values, we include it in the background evaluated from the control region, according to the method explained in Sec. IV A. It dominates this background, which is about 20% for 2.3-2.6 GeV/c^2 and 10% or lower at all other mass values. The total background is shown as the hatched histogram in Fig. 26.

We subtract the sum of backgrounds from the number of selected events in each mass interval to obtain the number of signal events. Considering the uncertainties in the cross sections for the background processes, the normalization of events in the control region, and the simulation statistics, we estimate that the systematic uncertainty on

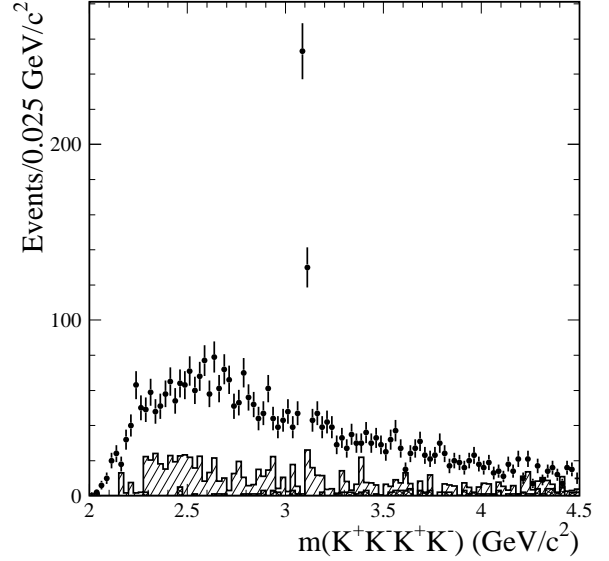


FIG. 26: Invariant mass distribution for $K^+K^-K^+K^-$ candidates in the data (points). The shaded histogram represents the non-ISR background, and the hatched region is for the ISR background from the control region, which is dominated by the contribution from misidentified ISR $K^+K^-\pi^+\pi^-$ events.

the signal yield is less than 5% in the 2–3 GeV/c^2 region, but that it increasing to about 10% above 3 GeV/c^2 .

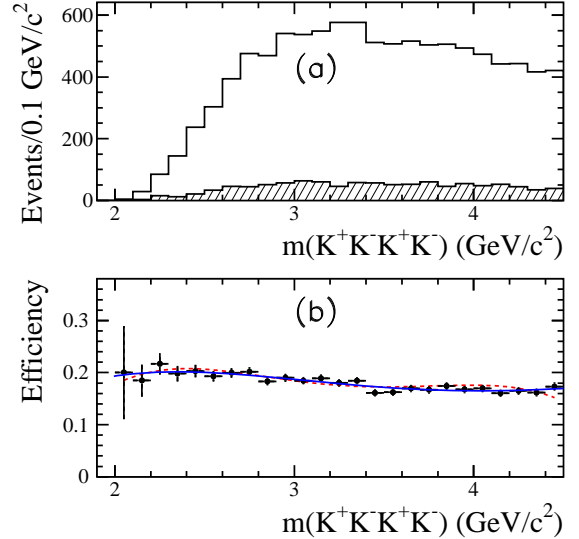


FIG. 27: (a) Invariant mass distributions for simulated $K^+K^-K^+K^-$ events in the signal (open) and control (hatched) regions (see Fig. 25); (b) net reconstruction and selection efficiency as a function of mass obtained from this simulation; the curves represent third-order polynomial fits for the phase space model (solid) and the ϕK^+K^- model (dashed).

B. Selection Efficiency

The detection efficiency is determined as for the other two final states. Figure 27(a) shows the simulated $K^+K^-K^+K^-$ invariant-mass distributions in the signal and control regions from the phase space model. We divide the number of reconstructed events in each mass interval by the number generated in that interval to obtain the efficiency shown by the points in Fig. 27(b). It is quite uniform, and we fit the measurements using a third-order polynomial, which we then use in obtaining the cross section. As discussed previously, this efficiency includes the difference between the EMC acceptance and the region of ISR photon simulation. A simulation assuming dominance of the ϕK^+K^- channel, with the K^+K^- pair in an angular-momentum S-wave state, gives consistent results, as shown by the dashed curve in Fig. 27(b), and we estimate a 5% systematic uncertainty associated with the difference. We correct only for mis-modeling of the track-finding and ISR-photon-detection efficiency as in Sec. IV B.

C. Cross Section for $e^+e^- \rightarrow K^+K^-K^+K^-$

We calculate the $e^+e^- \rightarrow K^+K^-K^+K^-$ cross section in 0.025 GeV intervals of $E_{c.m.}$ from the analog of Eq.(2), using the invariant mass of the $K^+K^-K^+K^-$ system to determine the c.m. energy. We show the cross section in Fig. 28, and list the measured values in Table X. The cross section increases from threshold to a peak value of about 0.1 nb near 2.7 GeV, then decreases slowly with increasing energy. The only statistically significant narrow structures are the large J/ψ peak and a possible narrow structure near 2.3 GeV, which will be discussed in Sec. VID. Again, the differential luminosity contribution in each $E_{c.m.}$ interval includes corrections for vacuum polarization that should be omitted for the calculations of a_μ . This measurement supersedes our previous result [13].

The simulated $K^+K^-K^+K^-$ invariant mass resolution is 3.0 MeV/ c^2 in the 2.0–2.5 GeV/ c^2 range, increasing with mass to 4.7 MeV/ c^2 in the 2.5–3.5 GeV/ c^2 range, and to about 6.5 MeV/ c^2 at higher masses. Since the cross section has no sharp structure except for the J/ψ peak, we again make no correction for resolution. The errors shown in Fig. 28 and listed in Table X are statistical only. The point-to-point systematic uncertainties are much smaller, and the errors on the normalization are summarized in Table XI, along with the corrections applied to the measurements. The total correction is +4.0%, and the total systematic uncertainty is 9% at low mass, linearly increasing to 13% above 3 GeV/ c^2 .

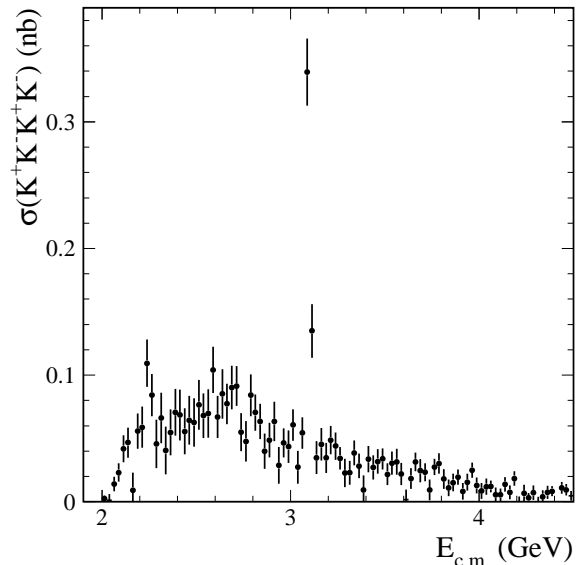


FIG. 28: The $e^+e^- \rightarrow K^+K^-K^+K^-$ cross section as a function of e^+e^- c.m. energy measured with ISR data at *BABAR*. The errors are statistical only.

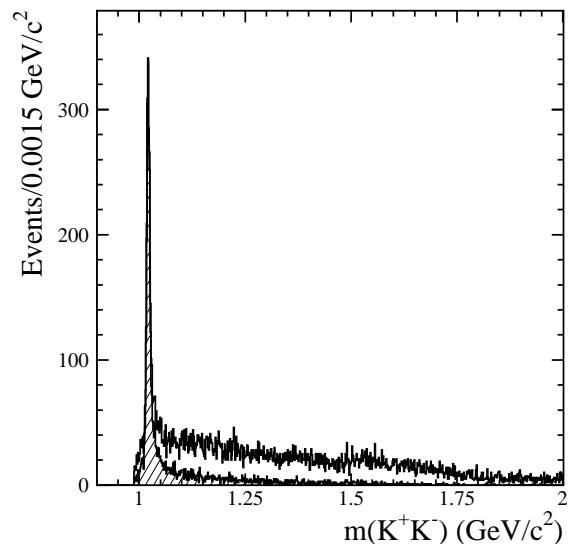


FIG. 29: Invariant mass distribution for all K^+K^- pairs in selected $e^+e^- \rightarrow K^+K^-K^+K^-$ events (open histogram), and for the combination in each event closest to the ϕ -meson mass (hatched).

D. The $\phi(1020)K^+K^-$ Intermediate State

Figure 29 shows the invariant mass distribution for all K^+K^- pairs in the selected $K^+K^-K^+K^-$ events (4 entries per event) as the open histogram. A prominent ϕ peak is visible along with a possible excess near 1.5 GeV/ c^2 . The hatched histogram is for the pair in each event with mass closest to the nominal ϕ mass, and indicates that the ϕK^+K^- channel dominates the $K^+K^-K^+K^-$ final state; we do not see any other signif-

TABLE X: Summary of the cross section measurements for $e^+e^- \rightarrow K^+K^-K^+K^-$. Errors are statistical only.

$E_{c.m.}$ (GeV)	σ (nb)	$E_{c.m.}$ (GeV)	σ (nb)	$E_{c.m.}$ (GeV)	σ (nb)	$E_{c.m.}$ (GeV)	σ (nb)
2.0125	0.002 ± 0.002	2.6375	0.100 ± 0.016	3.2625	0.035 ± 0.008	3.8875	0.020 ± 0.005
2.0375	0.003 ± 0.004	2.6625	0.083 ± 0.013	3.2875	0.030 ± 0.009	3.9125	0.011 ± 0.005
2.0625	0.013 ± 0.005	2.6875	0.097 ± 0.014	3.3125	0.027 ± 0.008	3.9375	0.017 ± 0.005
2.0875	0.021 ± 0.007	2.7125	0.094 ± 0.013	3.3375	0.040 ± 0.008	3.9625	0.023 ± 0.006
2.1125	0.040 ± 0.010	2.7375	0.064 ± 0.012	3.3625	0.032 ± 0.008	3.9875	0.015 ± 0.005
2.1375	0.046 ± 0.010	2.7625	0.061 ± 0.012	3.3875	0.021 ± 0.009	4.0125	0.012 ± 0.005
2.1625	0.021 ± 0.010	2.7875	0.091 ± 0.014	3.4125	0.037 ± 0.009	4.0375	0.015 ± 0.005
2.1875	0.057 ± 0.012	2.8125	0.074 ± 0.012	3.4375	0.031 ± 0.008	4.0625	0.012 ± 0.004
2.2125	0.066 ± 0.013	2.8375	0.067 ± 0.012	3.4625	0.035 ± 0.008	4.0875	0.008 ± 0.005
2.2375	0.112 ± 0.016	2.8625	0.050 ± 0.011	3.4875	0.034 ± 0.007	4.1125	0.008 ± 0.004
2.2625	0.086 ± 0.014	2.8875	0.054 ± 0.011	3.5125	0.025 ± 0.007	4.1375	0.015 ± 0.005
2.2875	0.063 ± 0.015	2.9125	0.073 ± 0.013	3.5375	0.033 ± 0.008	4.1625	0.010 ± 0.004
2.3125	0.083 ± 0.016	2.9375	0.042 ± 0.011	3.5625	0.035 ± 0.008	4.1875	0.018 ± 0.005
2.3375	0.060 ± 0.014	2.9625	0.048 ± 0.010	3.5875	0.025 ± 0.007	4.2125	0.003 ± 0.004
2.3625	0.070 ± 0.014	2.9875	0.050 ± 0.010	3.6125	0.008 ± 0.006	4.2375	0.012 ± 0.005
2.3875	0.083 ± 0.015	3.0125	0.062 ± 0.010	3.6375	0.020 ± 0.007	4.2625	0.004 ± 0.003
2.4125	0.087 ± 0.016	3.0375	0.037 ± 0.010	3.6625	0.031 ± 0.007	4.2875	0.009 ± 0.005
2.4375	0.071 ± 0.014	3.0625	0.057 ± 0.010	3.6875	0.028 ± 0.008	4.3125	0.003 ± 0.004
2.4625	0.079 ± 0.016	3.0875	0.334 ± 0.023	3.7125	0.023 ± 0.006	4.3375	0.006 ± 0.004
2.4875	0.080 ± 0.015	3.1125	0.151 ± 0.017	3.7375	0.014 ± 0.006	4.3625	0.009 ± 0.004
2.5125	0.093 ± 0.016	3.1375	0.045 ± 0.010	3.7625	0.026 ± 0.006	4.3875	0.008 ± 0.004
2.5375	0.079 ± 0.014	3.1625	0.053 ± 0.010	3.7875	0.031 ± 0.007	4.4125	0.001 ± 0.004
2.5625	0.086 ± 0.015	3.1875	0.041 ± 0.010	3.8125	0.021 ± 0.006	4.4375	0.012 ± 0.004
2.5875	0.110 ± 0.015	3.2125	0.051 ± 0.009	3.8375	0.013 ± 0.005	4.4625	0.010 ± 0.004
2.6125	0.077 ± 0.013	3.2375	0.046 ± 0.009	3.8625	0.018 ± 0.006	4.4875	0.006 ± 0.003

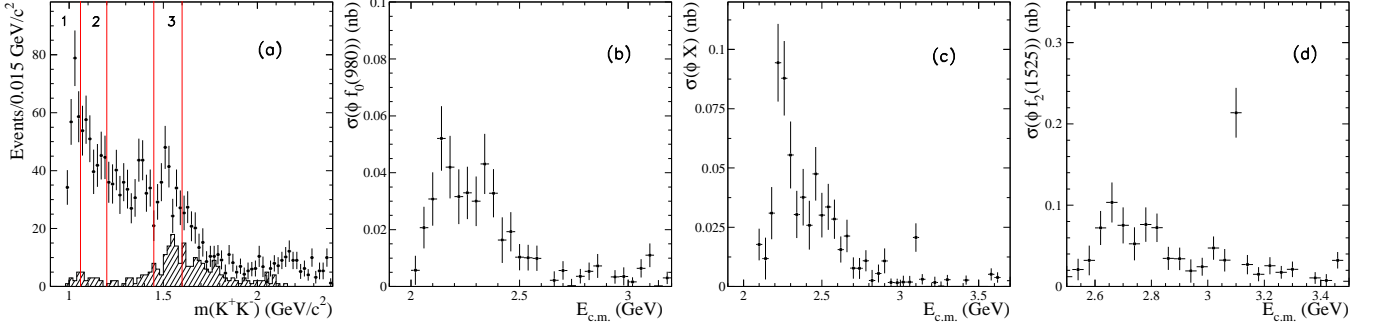


FIG. 30: (a) The invariant mass distribution for K^+K^- pairs in events in which the other K^+K^- pair has mass closest to, and within $10 \text{ MeV}/c^2$ of, the nominal ϕ mass (open histogram); events within $\pm 50 \text{ MeV}/c^2$ of the J/ψ mass have been excluded. The hatched histogram is for the $K^+K^-K^+K^-$ invariant mass in the J/ψ peak. The numbered regions of the combined histograms from (a) are used to calculate the cross sections shown in Figs. (b), (c) and (d) for regions 1, 2 and 3 respectively.

icant contribution. If the invariant mass of that K^+K^- pair which is closest to the ϕ mass is within $\pm 10 \text{ MeV}/c^2$ of the ϕ peak, then we include the invariant mass of the other K^+K^- combination in Fig. 30(a). Events with $K^+K^-K^+K^-$ mass within $\pm 50 \text{ MeV}/c^2$ of the J/ψ mass are excluded from the open histogram, while events within $\pm 50 \text{ MeV}/c^2$ of the J/ψ mass are shown as the hatched histogram. The latter is in agreement with the results from the BES experiment [31], for which the structures around $1.5, 1.7,$ and $2.0 \text{ GeV}/c^2$ were studied in detail. For the open histogram there is an enhancement at threshold that can be interpreted as being due to $f_0(980) \rightarrow K^+K^-$ decay. This is expected in light of the ϕf_0 cross sections measured above in the

$K^+K^-\pi^+\pi^-$ and $K^+K^-\pi^0\pi^0$ final states. For the combined histograms of Fig. 30(a), we select events with $m(K^+K^-) < 1.06 \text{ GeV}/c^2$ (shown as region 1) and calculate a cross section enriched in the $e^+e^- \rightarrow \phi f_0(980)$ reaction (Fig. 30(b)). A bump at $E_{c.m.} = 2.175 \text{ GeV}$ is seen, however the statistics and uncertainties in the $f_0(980) \rightarrow K^+K^-$ line-shape do not allow a meaningful extraction of the cross section for this $f_0(980)$ decay mode.

A clear signal corresponding to the $f'_2(1525)$ is seen in both histograms shown in Fig. 30(a). The $f'_2(1525)$ region is defined by $1.45 < m(K^+K^-) < 1.6 \text{ GeV}/c^2$, and is indicated as region 3 in Fig. 30(a). The corresponding cross section is shown in Fig. 30(d) and exhibits a broad

TABLE XI: Summary of corrections and systematic uncertainties for the $e^+e^- \rightarrow K^+K^-K^+K^-$ cross section measurements. The total correction is the linear sum of the individual corrections, and the total uncertainty is the sum in quadrature of the separate uncertainties.

Source	Correction	Uncertainty
Rad. Corrections	–	1%
Backgrounds	–	5% , $E_{c.m.} < 3$ GeV 5-10% , $E_{c.m.} > 3$ GeV
Model Dependence	–	5%
χ^2_{4K} Distribution	–	3%
Tracking Efficiency	+3.0%	2%
Kaon ID Efficiency	–	4%
ISR-photon Efficiency	+1.0%	0.5%
ISR Luminosity	–	3%
Total	+4.0%	9% , $E_{c.m.} < 3$ GeV 9-13% , $E_{c.m.} > 3$ GeV

(about 0.10-0.15 GeV) structure at 2.7 GeV and a strong J/ψ signal. In Fig. 30(a)(open histogram) there is an indication of structure for K^+K^- invariant mass in the 1.3-1.4 GeV/ c^2 region; this may correspond to production of the $\phi f_0(1370)$ final state.

Finally, we tried to find a region of K^+K^- invariant mass corresponding to the spike seen at about 2.3 GeV in the total $e^+e^- \rightarrow K^+K^-K^+K^-$ cross section shown in Fig. 28. This spike is much more significant if we require $1.06 < m(K^+K^-) < 1.2$ GeV/ c^2 , shown as region 2 in Fig. 30(a), with corresponding cross section shown in Fig. 30(c). We have no explanation of this structure.

We observe no significant structure in the $K^+K^-K^\pm$ mass distribution.

We use the ϕK^+K^- events to investigate the possibility that part of our $\phi\pi^+\pi^-$ signal is due to ϕK^+K^- events with the two kaons interpreted as pions. No structure is present in the resulting $K^+K^-\pi^+\pi^-$ invariant mass distribution.

VII. THE $e^+e^- \rightarrow \phi\pi\pi$ CROSS SECTION

We now perform a more detailed study in the $E_{c.m.}$ region from threshold to 3.0 GeV of the $e^+e^- \rightarrow \phi(1020)\pi\pi$ cross section. For this study we use the cross section for the $\phi\pi^+\pi^-$ final state shown in Figs. 13 and 15, after scaling by a factor of 1.5 to take into account the $\phi\pi^0\pi^0$ contribution. The cross section for the $\phi\pi^0\pi^0$ (see Fig. 23) final state does not help much due to large statistical errors. There are at least two candidate resonant structures in Fig. 13. These are associated with the peaks observed at 1.7 GeV and at 2.1 GeV. As shown in Sec. IV G, the latter is related to $\phi(1020)f_0(980)$ production, while the best candidate for the former may be the $\phi(1680)$, which is a radial excitation of the $s\bar{s}$ state decaying predominantly to $K^*(892)\bar{K}$ [16]. This would be the first observation of the decay of this state to $\phi(1020)\pi\pi$.

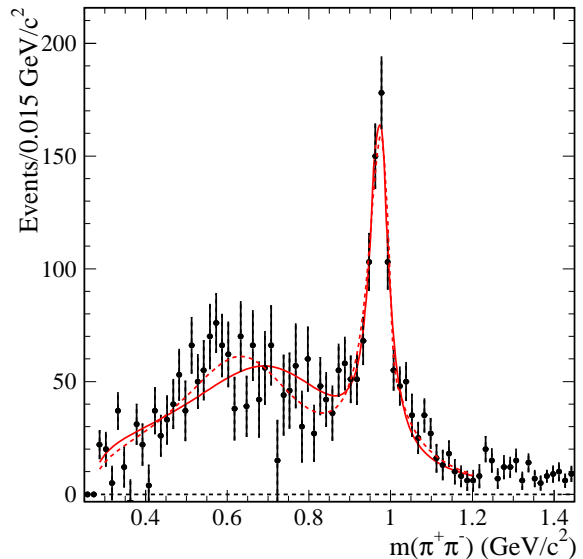


FIG. 31: The two-Breit-Wigner fit to the $\pi^+\pi^-$ invariant mass distribution of Fig. 12(d). The dashed curve corresponds to the inclusion of the partial width to $K\bar{K}$ in the propagator of the $f_0(980)$ BW.

As discussed in Sec. IV F we associate the narrow peak in the $\pi^+\pi^-$ invariant mass distribution, shown in larger scale in Fig. 31, with the $f_0(980)$ (denoted as the f_0 meson), and observe the broad bump at about 0.6 GeV/ c^2 ; the angular distributions of Fig. 14 justify that these structures are in an S-wave state. As shown in Sec. IV G the events in this broad structure are associated only with the $\phi(1680)$ resonance. This low mass bump can not be formed by pure three-body phase space. Indeed, the $\phi(1020)\pi\pi$ threshold is at 1.3 GeV, but the observed cross section has a slow rise started at 1.4 GeV. It indicates that the observed structure could be a result of the $f_0(600)$ resonance decay.

The observed two-pion-mass shape of the $f_0(600)$ (denoted as the σ meson) is distorted by the $\phi(1020)\pi\pi$ final state. This is less of an issue for the narrower $f_0(980)$. Nevertheless, to obtain mass and width parameter values for these states, we fit the data of Fig. 31 using a function consisting of an incoherent sum of two S-wave relativistic Breit-Wigner (BW) intensity distributions, modified to account for the two pion phase space. The fit values obtained are

$$m_\sigma = (0.692 \pm 0.030) \text{ GeV}/c^2, \Gamma_\sigma = (0.538 \pm 0.075) \text{ GeV}, \quad (3)$$

and

$$m_{f_0} = (0.972 \pm 0.002) \text{ GeV}/c^2, \Gamma_{f_0} = (0.056 \pm 0.011) \text{ GeV}, \quad (4)$$

and the fit result is represented by the solid curve in Fig. 31. Note that the $f_0(980)$ parameters are close to that from PDG [5], indicating a small interference effect with $f_0(600)$ (or $\pi\pi$ coherent continuum). This is expected because events with $m(\pi\pi) < 0.85$ GeV/ c^2 are associ-

ated with the resonance at $1.7 \text{ GeV}/c^2$ in the $\phi(1020)\pi\pi$ mass, while $f_0(980)$ contributes only to a structure above $2 \text{ GeV}/c^2$ (see Fig. 15).

The dashed curve is obtained when the $f_0(980) \rightarrow \bar{K}K$ partial width is incorporated into the BW propagator (the so called Flatté approximation used in Ref. [30]). It differs only slightly at the top of the $f_0(980)$, but the wider shape of the Flatté function leaves less room for the remaining events and we obtain:

$$m_\sigma = (0.631 \pm 0.020) \text{ GeV}/c^2, \Gamma_\sigma = (0.472 \pm 0.075) \text{ GeV}. \quad (5)$$

These parameters are in agreement with those obtained in Ref. [30]: $c2/c1 = 2.20 \pm 0.67$, $m \cdot c1 = 0.131 \pm 0.033$, which correspond to the ratio of the coupling constants $g_{KK}^2/g_{\pi\pi}^2$ and effective $f_0(980)$ width.

The Flatté approximation gives a little better description of the observed $\pi\pi$ mass spectrum, and so we use it in the analysis of the structures observed in the $\phi\pi\pi$ cross section.

It appears that the structure at $E_{\text{c.m.}} \approx 2.1 \text{ GeV}$ in the $\phi\pi^+\pi^-$ cross section (Fig. 13) couples to the $f_0(980)$ but not to the $f_0(600)$. This is very similar to the behavior observed for the $\pi^+\pi^-$ system in $J/\psi \rightarrow \phi\pi^+\pi^-$ decay [31] (and demonstrated with our data in Fig. 42 of Sec. IX), and in $D_s \rightarrow \pi^+\pi^-\pi^+$ decay [32]. In both instances a clear $f_0(980)$ signal is observed, while the broad $f_0(600)$ enhancement of Fig. 31 is absent. In contrast we note that in $J/\psi \rightarrow \omega\pi^+\pi^-$ decay [33] exactly the opposite behavior is observed; the $\pi^+\pi^-$ system exhibits a broad low-mass enhancement, and there is no evidence of an $f_0(980)$ signal.

Having established the mass and width values for the σ and f_0 , we now incorporate these two states in a simple model describing the structures in the $\phi\pi\pi$ cross section data of Fig. 13 (after scaling by a factor of 1.5 to take into account the $\phi\pi^0\pi^0$ contribution). The model consists of the incoherent addition of two contributions at each value of $E_{\text{c.m.}}$. The first represents the decay process $\phi(1680) \rightarrow \phi f_0(600)$, with the parameters of the σ given by Eq. (5); the second results from the coherent superposition of amplitudes describing the processes $\phi(1680) \rightarrow \phi f_0(980)$ and $Y(2175) \rightarrow \phi f_0(980)$, where the $Y(2175)$ BW amplitude describes the peak observed at $\approx 2.2 \text{ GeV}$ in Fig. 13. We note that in Ref. [9] the contribution from $\phi(1680) \rightarrow \phi f_0(980)$ decay was excluded. We see no physical evidence to justify doing this, and so allow the presence of this amplitude in our model. The angular distributions of Fig. 14 are consistent with the $\phi(1020)$ and the S-wave $\pi\pi$ system being in an S-wave orbital angular momentum state, and so our model includes no centrifugal barrier factor in the amplitude representations.

We fit the observed $e^+e^- \rightarrow \phi\pi\pi$ cross section using

the function

$$\sigma(s) = \frac{P_{\phi\sigma}(s)}{s^{3/2}} \cdot \left| \frac{A_{11}(s)}{\sqrt{P_{\phi\sigma}(m_1)}} \right|^2 + \frac{P_{\phi f_0}(s)}{s^{3/2}} \cdot \left| \frac{A_{12}(s)e^{i\psi}}{\sqrt{P_{\phi f_0}(m_1)}} + \frac{A_{22}(s)}{\sqrt{P_{\phi f_0}(m_2)}} \right|^2, \quad (6)$$

where

$$A_{ij}(s) = \frac{\sqrt{\sigma_{ij}} m_i^{3/2} m_i \Gamma_i}{m_i^2 - s - i\sqrt{s}\Gamma_i(s)},$$

with

$i = 1$ for the $\phi(1680)$, $i = 2$ for the $Y(2175)$,
 $j = 1$ for the $f_0(600)$, $j = 2$ for the $f_0(980)$,

so that

$A_{11}(s)$ describes $\phi(1680) \rightarrow \phi(1020)f_0(600)$ decay,
 $A_{12}(s)$ describes $\phi(1680) \rightarrow \phi(1020)f_0(980)$ decay,
 $A_{22}(s)$ describes $Y(2175) \rightarrow \phi(1020)f_0(980)$ decay;

$s = E_{\text{c.m.}}^2$, m_1 and Γ_1 are the mass and width of the $\phi(1680)$, m_2 and Γ_2 are the mass and width of the $Y(2175)$, and the σ_{ij} represent the peak cross section values.

The factors $P_{\phi\sigma}(s)$ and $P_{\phi f_0}(s)$ represent quasi-two body phase space integrated over the range of $\pi\pi$ invariant mass available at $E_{\text{c.m.}} = \sqrt{s}$, and are obtained from

$$P_{\phi\pi\pi}(s) = \int_{2m_\pi}^{\sqrt{s}-m_\phi} BW_{\pi\pi}(m) q(s, m, m_\phi) dm, \quad (7)$$

where $BW_{\pi\pi}(m)$ is a Breit-Wigner function with $f_0(980)$ parameters ($BW_{f_0}(m)$) to get $P_{\phi f_0}(s)$, or with $f_0(600)$ parameters ($BW_\sigma(m)$) to get $P_{\phi\sigma}(s)$ [27], and q is the quasi-two-body momentum for invariant mass \sqrt{s} .

Since the decay $\phi(1680) \rightarrow \phi(1020)f_0(980)$ is suppressed by phase space near $\sqrt{s} = m_1$, the value of σ_{12} is much smaller than that of σ_{11} , but its contribution to $\sigma(s)$ increases rapidly beyond $\phi(1020)f_0(980)$ threshold.

The $\phi(1680)$ resonance decays mainly to $\bar{K}K^*(892)$ and $\phi(1020)\eta$ [5], [16]. We find that it has a branching fraction of $\approx 10\%$ to $\phi\pi\pi$, which together with other modes listed in PDG, leads to an energy-dependent width which can be written as

$$\Gamma_1(s) = \Gamma_1 \left[0.7 \frac{m_1^3 P_{2K}(s)}{s^{3/2} P_{2K}(m_1^2)} + 0.2 \frac{m_1 P_{\phi\eta}(s)}{s^{1/2} P_{\phi\eta}(m_1^2)} + 0.1 \frac{m_1 P_{\phi\pi\pi}(s)}{s^{1/2} P_{\phi\pi\pi}(m_1^2)} \right], \quad (8)$$

with $P_{2K}(s) = q^3(\sqrt{s}, m_K, m_{K^*})$, and $P_{\phi\eta}(s) = q(\sqrt{s}, m_\phi, m_\eta)$.

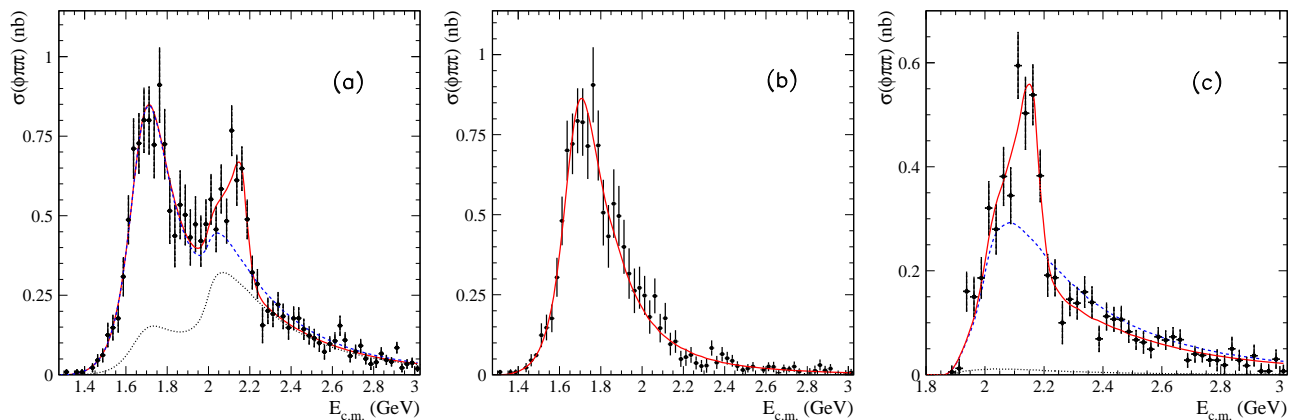


FIG. 32: (a) The fit to the $e^+e^- \rightarrow \phi\pi\pi$ cross section using the model described in the text; the entire contribution due to the $\phi(1680)$ is shown by the dashed curve. The dotted curve shows the contribution for only $\phi f_0(980)$ decay. (b) Comparison of the data and the curve obtained from the overall fit, with the restriction $m(\pi\pi) < 0.85 \text{ GeV}/c^2$. (c) The $e^+e^- \rightarrow \phi(1020)f_0(980)$ cross section with the requirement $0.85 < m(\pi\pi) < 1.1 \text{ GeV}/c^2$; the dashed and dotted curves represent the contributions from $\phi(1680) \rightarrow \phi(1020)f_0(980)$, and $\phi(1680) \rightarrow \phi(1020)f_0(600)$ calculated using the parameter values from the overall fit to the cross section data.

TABLE XII: Summary of parameter values obtained from the fits with Eq. (6) described in the text. An asterisk denotes a value that was fixed in that fit.

Fit	All $m(\pi\pi)$	$m(\pi\pi) < 0.85 \text{ GeV}/c^2$	$0.85 < m(\pi\pi) < 1.1 \text{ GeV}/c^2$
σ_{11} (nb)	$0.655 \pm 0.039 \pm 0.040$	$0.678 \pm 0.047 \pm 0.040$	0.655^*
m_1 (GeV/c^2)	$1.742 \pm 0.013 \pm 0.012$	$1.733 \pm 0.010 \pm 0.010$	1.742^*
Γ_1 (GeV)	$0.337 \pm 0.043 \pm 0.061$	$0.300 \pm 0.015 \pm 0.037$	0.337^*
σ_{22} (nb)	$0.082 \pm 0.024 \pm 0.010$	0.082^*	$0.094 \pm 0.023 \pm 0.010$
m_2 (GeV/c^2)	$2.176 \pm 0.014 \pm 0.004$	2.176^*	$2.172 \pm 0.010 \pm 0.008$
Γ_2 (GeV)	$0.090 \pm 0.022 \pm 0.010$	0.090^*	$0.096 \pm 0.019 \pm 0.012$
σ_{12} (nb)	$0.152 \pm 0.034 \pm 0.040$	0.152^*	$0.132 \pm 0.010 \pm 0.010$
ψ (rad)	$-1.94 \pm 0.34 \pm 0.10$	-1.94^*	$-1.92 \pm 0.24 \pm 0.12$
$\chi^2/\text{n.d.f.}$	48/(67-9)	46/(66-4)	38/(46-6)
$P(\chi^2)$	0.74	0.96	0.40

For the second resonance candidate, which decays mostly to $\phi\pi\pi$, the energy dependence of the width is written as

$$\Gamma_2(s) = \Gamma_2 \frac{m_2 P_{\phi\pi\pi}(s)}{s^{1/2} P_{\phi\pi\pi}(m_2^2)}. \quad (9)$$

We note that the introduction of an energy dependence for each width significantly increases the values of the resonance mass and width, especially for broad structures.

The results of the fits are shown in Fig. 32 and summarized in Table XII. The first error is statistical, and the second error represents the systematic uncertainty estimated as a difference in fitted values for two different descriptions of the two-pion spectrum as shown in Fig. 31. In Fig. 32(a) we show the contribution from the $\phi(1680)$ for both modes (dashed curves), and for $\phi(1680) \rightarrow \phi(1020)f_0(980)$ only (dotted curve). The increase of the cross section at about 2 GeV is explained by the opening of the $\phi f_0(980)$ decay channel of the $\phi(1680)$ resonance. However the fit shows that an additional relatively narrow state is needed in order to provide a better description of the observed data.

It is important to note that this model describes the observed data very well independently of the $m(\pi\pi)$ region selected. Figure 32(b) shows the $\phi\pi\pi$ cross section for $m(\pi^+\pi^-) < 0.85 \text{ GeV}/c^2$ for the data; the curve is obtained by using the parameter values from the overall fit and yields $\chi^2/\text{ndf} = 63/(66-1)$ ($P(\chi^2) = 0.54$). If we fit this distribution, slightly better parameter values can be obtained (see Table XII), but these still agree well with those from the overall fit. We consider them as our measurement of the $\phi(1680)$ resonance parameters and they are corresponding to the product of electronic width, Γ_{ee} , and branching fraction to $\phi\pi\pi$, $\mathcal{B}_{\phi\pi\pi}$,

$$\mathcal{B}_{\phi\pi\pi} \cdot \Gamma_{ee} = \frac{\Gamma_1 \sigma_{11} m_1^2}{12\pi C} = (42 \pm 2 \pm 3) \text{ eV},$$

where we fit the product $\Gamma_1 \sigma_{11}$ to reduce correlations, and C , the conversion constant, is $0.389 \text{ mb}(\text{GeV}/c^2)^2$ [5]. The second error is systematic, and corresponds to the normalization uncertainty on the cross section, and to the uncertainty in the $m(\pi\pi)$ distribution description.

If we require $0.85 < m(\pi\pi) < 1.1 \text{ GeV}/c^2$ (Fig. 32(c)), then without additional fitting the model gives χ^2/ndf

= 48/(46-1) ($P(\chi^2) = 0.31$), and improves by refitting to $\chi^2/\text{ndf} = 38/(46-6)$ ($P(\chi^2) = 0.40$) with the parameter values listed in Table XII. If we try to explain the observed cross section only in terms of the $\phi(1680)$ without any narrow state (dashed curve in Fig. 32(c), the fit gives $\chi^2/\text{ndf} = 123/(46-2)$ ($P(\chi^2) = 10^{-7}$), and so this hypothesis is not compatible with the data.

The model described above provides an excellent description of the observed cross section behavior, and suggests that the $Y(2175)$ may not be a radially excited $s\bar{s}$ state, since such a state would be expected to be much wider (300-400 GeV/c^2), and also should decay to $\phi f_0(600)$, like the $\phi(1680)$.

VIII. $e^+e^- \rightarrow \phi f_0$ NEAR THRESHOLD

The behavior of the $e^+e^- \rightarrow \phi f_0$ cross section near threshold shows a structure near $2.175 \text{ GeV}/c^2$, and we have published this result in Ref. [7]. Here we provide a more detailed study of the cross section for this channel in the 1.8–3 GeV region with the full *BABAR* dataset. In Fig. 33 we superimpose the cross sections measured in the $K^+K^-\pi^+\pi^-$ and $K^+K^-\pi^0\pi^0$ final states (shown in Figs. 15 and 24); they are consistent with each other.

We perform a combined fit to these cross section data using Eq.(6) with the two-pion mass restricted to the region 0.85-1.1 GeV/c^2 . We fix the $\phi(1680)$ parameters for the $\phi(1020)f_0(600)$ decay mode (which gives a small contribution in this mass range) and allow all other parameters to float. The result of the fit is shown as the solid curve in Fig. 33. The fit gives the resonance parameter values

$$\begin{aligned} \sigma_{22} &= (0.093 \pm 0.021 \pm 0.010) \text{ nb}, \\ m_2 &= (2.180 \pm 0.008 \pm 0.008) \text{ GeV}/c^2, \\ \Gamma_2 &= (0.077 \pm 0.015 \pm 0.010) \text{ GeV}, \\ \psi_2 &= (-2.11 \pm 0.24 \pm 0.12) \text{ rad}, \\ \sigma_{12} &= (0.140 \pm 0.009 \pm 0.010) \text{ nb}, \end{aligned}$$

and $\chi^2/\text{n.d.f.} = 57/(61-6)$ ($P(\chi^2) = 0.33$). The statistical precision is improved compared to that of Ref. [7], for which the analysis was based on half as much data. For this state we estimate the product of electronic width and branching fraction to ϕf_0 as

$$\mathcal{B}_{\phi f_0} \cdot \Gamma_{ee} = \frac{\Gamma_2 \sigma_{22} m_2^2}{12\pi C} = (2.3 \pm 0.3 \pm 0.3) \text{ eV},$$

where we fit the product $\Gamma_2 \sigma_{22}$ to reduce correlations. The second error is systematic, and corresponds to the normalization uncertainty on the cross section.

If we assume no resonance structure other than the $\phi(1680) \rightarrow \phi(1020)f_0(980)$, the fit yields $\chi^2/\text{n.d.f.} = 150/(61-2)$ with $P(\chi^2) = 8 \cdot 10^{-9}$. The result of this fit is shown as the dashed curve in Fig. 33. It is a poor fit to the region below 2.3 GeV , but gives a good description of the cross section behavior at higher values of $E_{\text{c.m.}}$. The

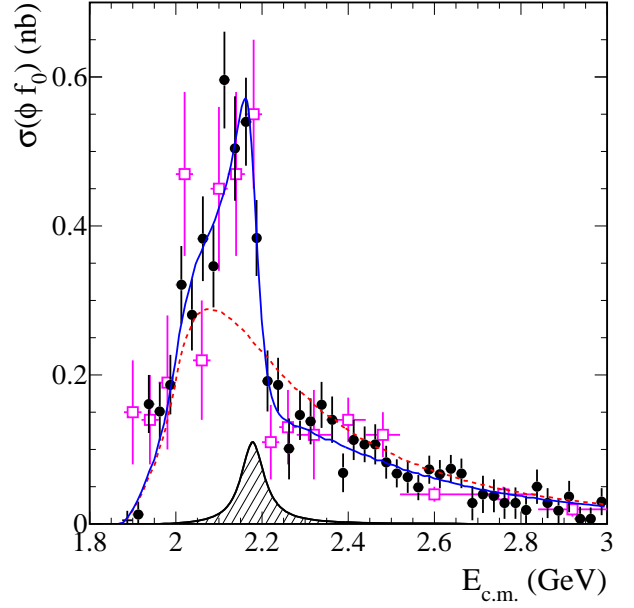


FIG. 33: The $e^+e^- \rightarrow \phi(1020)f_0(980)$ cross section measured in the $K^+K^-\pi^+\pi^-$ (solid dots) and $K^+K^-\pi^0\pi^0$ (open squares) final states. The solid (dashed) curve represents the result of the two-resonance (one-resonance - $\phi(1680) \rightarrow \phi(1020)f_0(980)$) fit using Eq.(6), as described in the text. The hatched area shows $Y(2175)$ contribution.

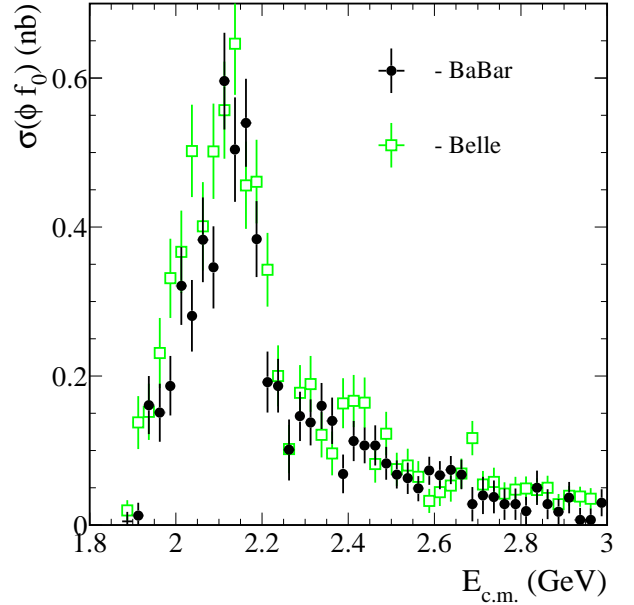


FIG. 34: The $e^+e^- \rightarrow \phi(1020)f_0(980)$ cross section measurements from the $K^+K^-\pi^+\pi^-$ final state from *BABAR* (dots) and Belle [9](squares).

fit, with or without the resonance at 2.18 GeV/c^2 , gives a maximum value of the non-resonant cross section of 0.3 nb at $E_{\text{c.m.}} \approx 2.1 \text{ GeV}$. This is of independent theoretical interest, because it can be related to the $\phi \rightarrow f_0(980)\gamma$ decay studied at the ϕ -factory [28, 29].

The significance of the structure calculated from the

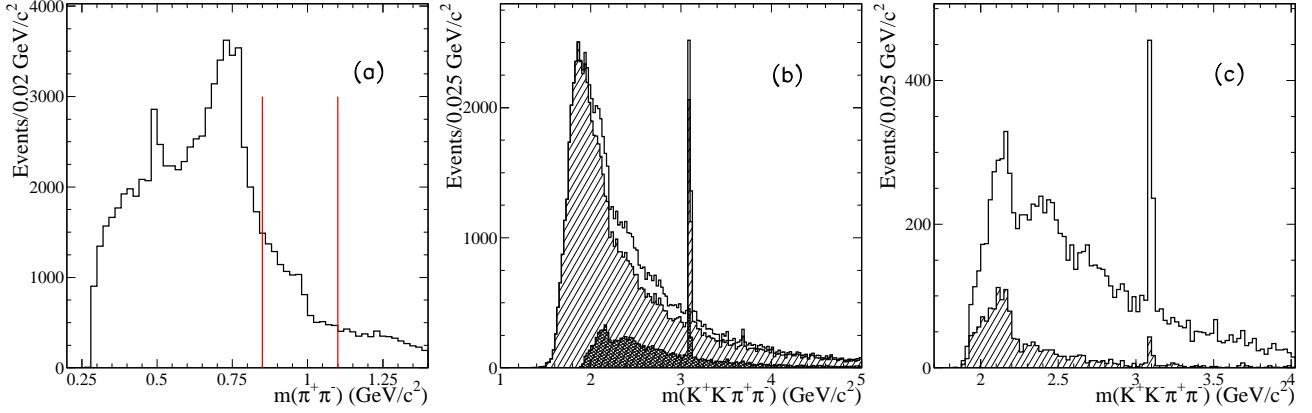


FIG. 35: (a) The $m(\pi^+\pi^-)$ distribution without background subtraction for $K^+K^-\pi^+\pi^-$ events. The vertical lines indicate the $f_0(980)$ region. (b) All selected $K^+K^-\pi^+\pi^-$ events (open histogram), selected $K^+K^-f_0(980)$ events (cross-hatched histogram), and all the rest (hatched histogram). (c) The $K^+K^-f_0(980)$ events (open histogram) in comparison with the $\phi(1020)f_0(980)$ sample (hatched histogram).

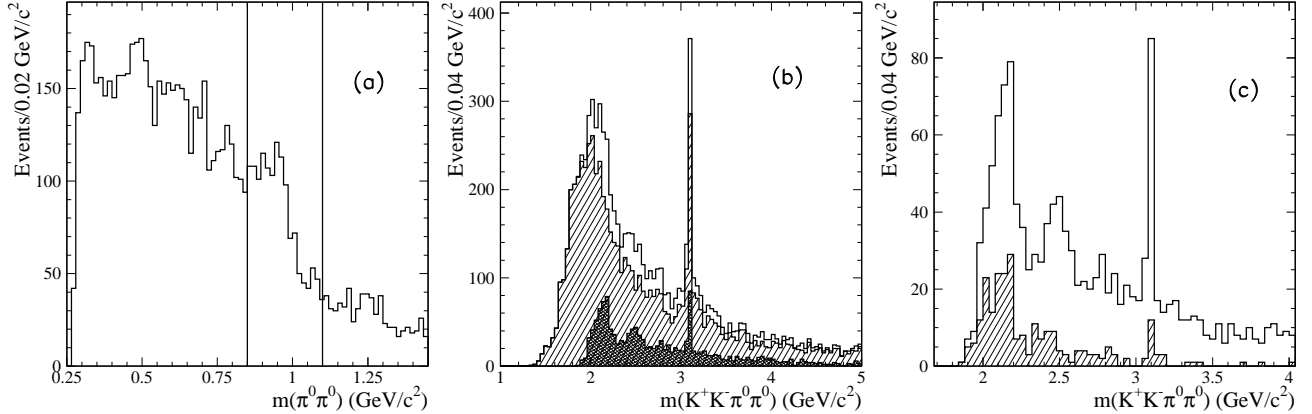


FIG. 36: (a) The $m(\pi^0\pi^0)$ distribution without background subtraction for $K^+K^-\pi^0\pi^0$ events. The vertical lines indicate the $f_0(980)$ region. (b) All selected $K^+K^-\pi^0\pi^0$ events (open histogram), selected $K^+K^-f_0(980)$ events (cross-hatched histogram), and all the rest (hatched histogram). (c) The $K^+K^-f_0(980)$ events (open histogram) in comparison with the $\phi(1020)f_0(980)$ sample (hatched histogram).

change in χ^2 between the fits with and without the resonance at 2.18 GeV is $\sqrt{150 - 61} = 9.4$ standard deviations; the χ^2 value, 61 for 2 constraints yields the same probability as the χ^2 value 57 for 6 constraints.

The cross section measurements from the $K^+K^-\pi^+\pi^-$ final state shown in Fig. 33 are compared to those from Belle [9] in Fig. 34. There is good overall agreement between the results from the two experiments. Overall agreement between the results of the fits to the BABAR and Belle data is also good.

A. Structures in the $K^+K^-f_0(980)$ final state

We now search for other decay modes of the $Y(2175)$ state. Figure 35(a) shows the “raw” (no background subtraction) two-pion mass distribution for all selected $K^+K^-\pi^+\pi^-$ events, and Fig. 36(a) shows the same distribution for the $K^+K^-\pi^0\pi^0$ sample. The $f_0(980)$ con-

tribution is relatively small for the charged-pion mode, and larger for the neutral-pion mode. If we select the region $0.85 < m(\pi\pi) < 1.1$ GeV/ c^2 , and plot the $K^+K^-\pi\pi$ mass distribution, the bump at 2.175 GeV/ c^2 is seen much more clearly in spite of larger background (Figs. 35(b) and 36(b)), and a bump at 2.5 GeV/ c^2 is also seen; the rest of events have no structures at 2.175 GeV/ c^2 or 2.5 GeV/ c^2 (Figs. 35(b) and 36(b) hatched histograms). The bumps are seen only in the $K^+K^-f_0(980)$ sample (Figs. 35(c) and 36(c)), but if we select the $\phi(1020)$ region, no bumps are seen at 2.5 GeV/ c^2 , as shown by the hatched histograms in Figs. 35(c) and 36(c).

From these histograms we can conclude, that the $Y(2175)$ resonance has a $K^+K^-f_0(980)$ decay mode when the K^+K^- system is not from ϕ , and that the decay rate is comparable to that for $\phi f_0(980)$. Also another state at 2.5 GeV seems to exist; this decays to $K^+K^-f_0(980)$ (but seems not to couple to $\phi f_0(980)$)

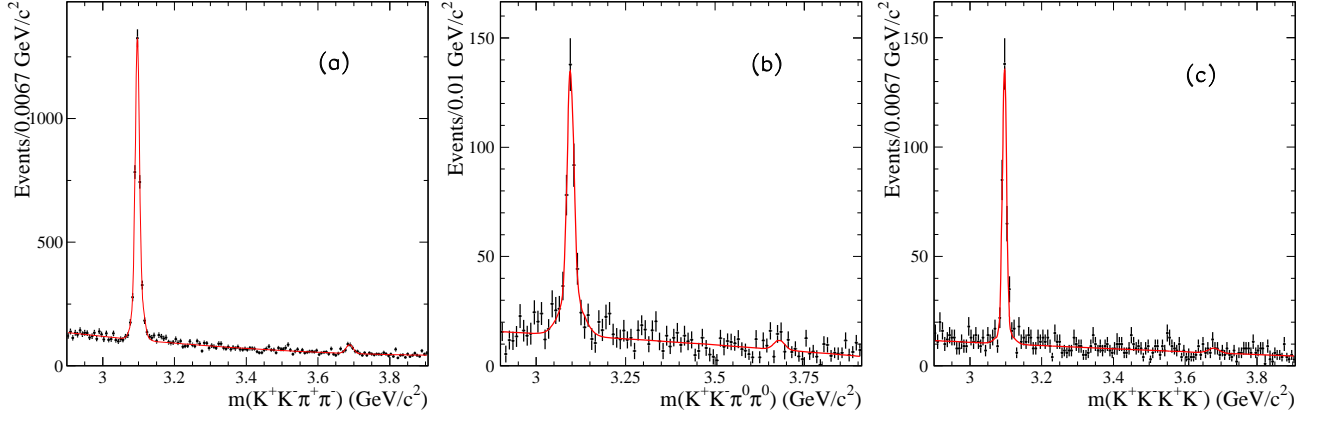


FIG. 37: Raw invariant mass distribution for all selected events in the charmonium region for (a) $e^+e^- \rightarrow K^+K^-\pi^+\pi^-$, (b) $e^+e^- \rightarrow K^+K^-\pi^0\pi^0$, and (c) $e^+e^- \rightarrow K^+K^-K^+K^-$; in each figure the curve represents the result of the fit described in the text.

with width $\approx 0.06\text{-}0.08$ GeV (see Ref. [7]). The large background does not allow us to clearly separate this state.

IX. THE CHARMONIUM REGION

For the $E_{c.m.}$ region above 3 GeV, our data can be used to measure, or set limits on, the decay branching fractions for the J/ψ and $\psi(2S)$ (See Figs. 4, 19, and 28). In addition, these signals allow checks of our mass scale, and of our measurements of mass resolution. Figure 37 shows the invariant mass distributions for the selected $K^+K^-\pi^+\pi^-$, $K^+K^-\pi^0\pi^0$, and $K^+K^-K^+K^-$ events, respectively, in this region, using smaller mass intervals than in the corresponding Figs. 2, 17, and 26. We do not subtract any background from the $K^+K^-\pi^+\pi^-$ and $K^+K^-K^+K^-$ distributions, since it is small and nearly uniformly distributed, but we use the $\chi^2_{2K2\pi^0}$ control region to subtract part of the ISR background from the $K^+K^-\pi^0\pi^0$ distribution. Production of the J/ψ is apparent in all three distributions, and a small, but clear, $\psi(2S)$ signal is visible in the $K^+K^-\pi^+\pi^-$ mode.

We fit each of these distributions using a sum of two Gaussian functions to describe the J/ψ signal and incorporate a similar representation of a $\psi(2S)$ signal, although there is no clear evidence of the latter in Figs. 37(b) and 37(c). In each case, a second-order-polynomial function is used to describe the remainder of the distribution. We take the signal function parameter values from simulation, but let the overall mean and width values vary in the fits, together with the coefficients of the polynomial. For the $K^+K^-\pi^0\pi^0$ and $K^+K^-K^+K^-$ modes we fix the $\psi(2S)$ mass position [5], and take the width from MC simulation. The fits are of good quality, and are shown by the curves in Fig. 37. In all cases, the fitted mean value is within 1 MeV/ c^2 of the nominal J/ψ or $\psi(2S)$ mass [5], and the width is within

10% of the simulated resolution discussed in Secs. IV C, V C, and VI C.

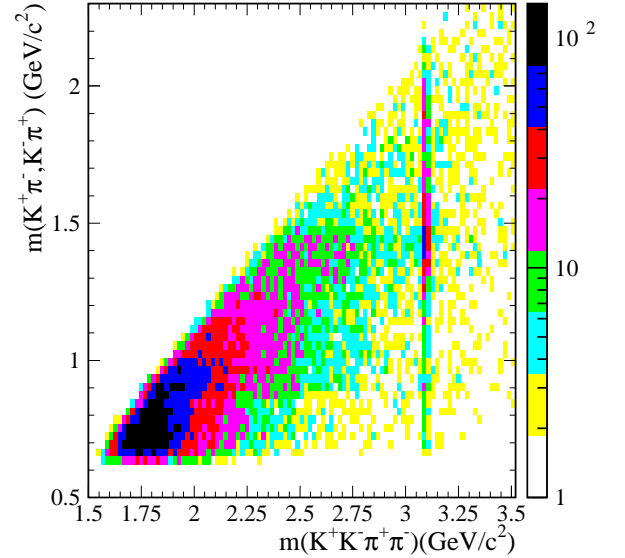


FIG. 38: The $K^\pm\pi^\mp$ invariant mass versus $K^+K^-\pi^+\pi^-$ invariant mass for events with the $K^\pm\pi^\pm$ combination in one of the $K^*(892)^0$ regions of Fig. 5(a); for events in overlap region, only one combination is chosen.

The fitted J/ψ signals for the $K^+K^-\pi^+\pi^-$, $K^+K^-\pi^0\pi^0$, and $K^+K^-K^+K^-$ final states are found to contain 3137 ± 67 , 388 ± 28 , and 287 ± 24 events, respectively. From the number of events in each final state f , $N_{J/\psi \rightarrow f}$, we calculate the product of the J/ψ branching fraction to f and the J/ψ electronic width using

$$\mathcal{B}_{J/\psi \rightarrow f} \cdot \Gamma_{ee}^{J/\psi} = \frac{N_{J/\psi \rightarrow f} \cdot m_{J/\psi}^2}{6\pi^2 \cdot d\mathcal{L}/dE \cdot \epsilon_f(m_{J/\psi}) \cdot C} \quad , \quad (10)$$

where $d\mathcal{L}/dE = 173.1 \pm 1.7$ nb $^{-1}$ /MeV, and $\epsilon_f(m_{J/\psi})$ are the ISR luminosity and corrected selection efficiency,

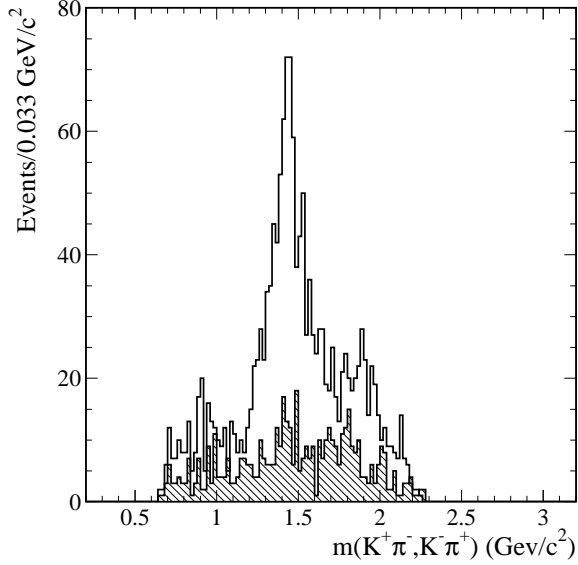


FIG. 39: The $K^\pm\pi^\pm$ mass projection for events from Fig. 38 with $K^+K^-\pi^+\pi^-$ invariant mass within $50 \text{ MeV}/c^2$ of the nominal J/ψ mass (open histogram), and for events for which this mass value is $50\text{--}100 \text{ MeV}/c^2$ less than nominal (hatched).

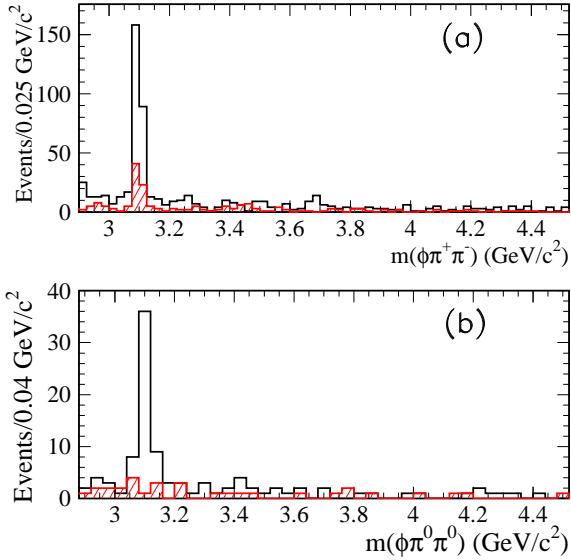


FIG. 40: Raw invariant mass distributions in the charmonium region for (a) candidate $e^+e^- \rightarrow \phi\pi^+\pi^-$ events (open histogram), and for events in the ϕ sideband regions of Fig. 12(c) (hatched); (b) candidate $e^+e^- \rightarrow \phi\pi^0\pi^0$ events (open histogram) and events in the $\chi^2_{K2\pi^0}$ control region (hatched).

respectively, at the J/ψ mass, and C is the conversion constant. We estimate $\epsilon_{K^+K^-\pi^+\pi^-} = 0.198 \pm 0.006$, $\epsilon_{K^+K^-\pi^0\pi^0} = 0.079 \pm 0.004$, and $\epsilon_{K^+K^-\pi^+K^-} = 0.173 \pm 0.012$ using the corrections and errors discussed in Secs. IV C, V C, and VI C.

We list the values of the product of the branching fraction(s) and $\Gamma_{ee}^{J/\psi}$ in Table XIII, and using $\Gamma_{ee}^{J/\psi} = (5.55 \pm 0.14) \text{ keV}$ [5], obtain the corresponding branching fraction values and list them together with their PDG

values [5]. The systematic uncertainties quoted include a 2.5% uncertainty on $\Gamma_{ee}^{J/\psi}$. Our measured branching fractions of $K^+K^-\pi^+\pi^-$, $K^+K^-\pi^0\pi^0$, and $K^+K^-\pi^+K^-$ are more precise than the current PDG values, which are dominated by our previous results $((6.6 \pm 0.5) \times 10^{-3}$, $(2.5 \pm 0.3) \times 10^{-3}$ and $(7.6 \pm 0.9) \times 10^{-4}$, respectively [7]).

These fits also yield 133 ± 21 $K^+K^-\pi^+\pi^-$ events, 17 ± 9 $K^+K^-\pi^0\pi^0$ events and 13 ± 6 $K^+K^-\pi^+K^-$ events in the $\psi(2S)$ peak. We expect 12 events from $\psi(2S) \rightarrow J/\psi\pi^+\pi^- \rightarrow K^+K^-\pi^+\pi^-$ from the relevant branching fractions [5], which is less than the statistical error. Subtracting this contribution and using the calculation analogous to Eq.(10), with $d\mathcal{L}/dE = 221.2 \pm 2.2 \text{ nb}^{-1}/\text{MeV}$, we obtain the product of the branching fraction and electronic width for the decays $\psi(2S) \rightarrow K^+K^-\pi^+\pi^-$, $\psi(2S) \rightarrow K^+K^-\pi^0\pi^0$, and $\psi(2S) \rightarrow K^+K^-\pi^+K^-$. Dividing by $\Gamma_{ee}^{\psi(2S)} = 2.36 \pm 0.04 \text{ keV}$ [5], we obtain the branching fractions listed in Table XIII. The $K^+K^-\pi^+\pi^-$ and $K^+K^-\pi^+K^-$ values are consistent with those in Ref. [5]. There is no entry in Ref. [5] for the $K^+K^-\pi^0\pi^0$ decay mode of the $\psi(2S)$.

As noted in Sec. IV D and shown in Fig. 5, the $K^+K^-\pi^+\pi^-$ final state is dominated by the $K^*(892)^0 K^-\pi^+$ channels, with a small contribution from the $K^*(892)^0 \bar{K}_2^*(1430)^0$ channels. Figure 38 shows a scatter plot of the invariant mass of a $K^\pm\pi^\mp$ pair versus that of the $K^+K^-\pi^+\pi^-$ system for events with the mass of the $K^\mp\pi^\pm$ pair near the $K^*(892)^0$ mass, i.e. within the bands in Fig. 5(a), but with only one combination plotted in the overlap region. There is a large concentration of entries in the J/ψ band with $K^\pm\pi^\mp$ mass values near $1.43 \text{ GeV}/c^2$, but a relatively small number of events in a horizontal band corresponding to the $K_2^*(1430)^0$ production outside the J/ψ region. We show the $K^\pm\pi^\mp$ mass projection for the subset of events with $K^+K^-\pi^+\pi^-$ mass within $50 \text{ MeV}/c^2$ of the nominal J/ψ mass in Fig. 39 as the open histogram. The hatched histogram is the projection for events with a $K^+K^-\pi^+\pi^-$ mass between 50 and $100 \text{ MeV}/c^2$ away from the nominal J/ψ mass.

The $K\pi$ distribution from the J/ψ is dominated by the $K_2^*(1430)^0$ signal. A small signal at the $K^*(892)^0$ indicates the presence of $K^*(892)^0 \bar{K}^*(892)^0$ decay of the J/ψ ; this is also seen as an enhancement in the J/ψ band in Fig. 38. The enhancement at $1.9 \text{ GeV}/c^2$ of Fig. 39 may be due to the 3F_2 ground state, or to the first radial excitation of the $K_2^*(1430)$, neither of which has been reported previously. Subtracting the number of sideband events from the number in the J/ψ mass window, we obtain 710 ± 30 events with $K^\pm\pi^\mp$ mass in the range $1.2\text{--}1.7 \text{ GeV}/c^2$, which we take as a measure of J/ψ decay into $K^*(892)^0 \bar{K}_2^*(1430)^0$, 47 ± 12 events in the $0.8\text{--}1.0 \text{ GeV}/c^2$ window for $K^*(892)^0 \bar{K}^*(892)^0$ decay, and 185 ± 21 events for decay to $K^*(892)^0 K^-\pi^+$ with $m(K\pi)$ in the $1.7\text{--}2.0 \text{ GeV}/c^2$ region. We convert these to branching fractions using Eq.(10), and divide by the known branching fractions of the K^* states [5]. The results are listed in Table XIII, and are more precise than

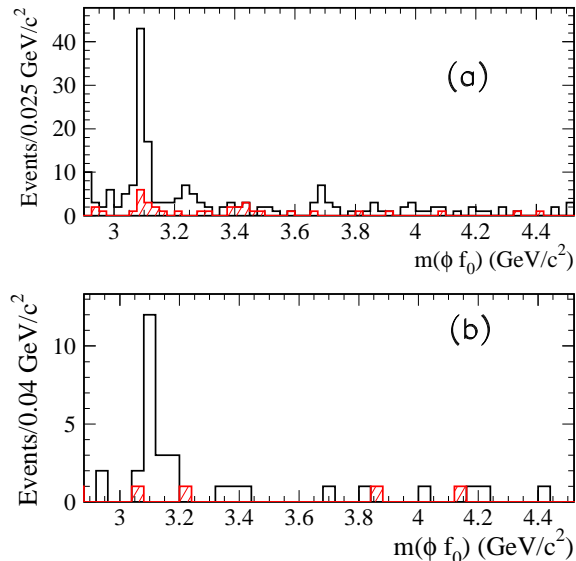


FIG. 41: Raw invariant mass distribution in the charmonium region (a) for candidate ϕf_0 , $f_0 \rightarrow \pi^+\pi^-$ events (open histogram), and for events in the ϕ sideband region (hatched), and (b) for candidate ϕf_0 , $f_0 \rightarrow \pi^0\pi^0$ events (open histogram) and for events in the $\chi^2_{2K2\pi^0}$ control region (hatched).

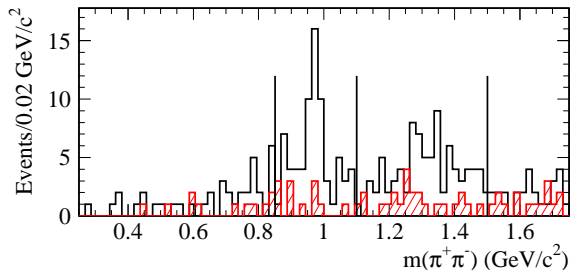


FIG. 42: The $\pi^+\pi^-$ invariant mass distribution for $\phi\pi^+\pi^-$ events from the J/ψ peak of Fig. 40(a) (open histogram), and for events in the ϕ sideband region (hatched);

those in Ref. [5]. For the 1.7–2.0 GeV/c^2 mass region we obtain $\Gamma_{ee}^{J/\psi} B_{J/\psi \rightarrow K^*(892)^0 K^-\pi^+} = (2.24 \pm 0.25 \pm 0.15) \text{eV}$.

We study decays into $\phi\pi^+\pi^-$ and $\phi\pi^0\pi^0$ using the mass distributions shown in Figs. 40(a),(b). The open histograms are for events with K^+K^- mass within the ϕ bands of Figs. 12(c) and 22(c). The hatched histogram in Fig. 40(a) is from the ϕ sidebands of Fig. 12(c), and represents the dominant background in the $\phi\pi^+\pi^-$ mode. The hatched histogram in Fig. 40(b) is from the $\chi^2_{2K2\pi^0}$ control region, and represents the dominant background in the $\phi\pi^0\pi^0$ mode. Subtracting these backgrounds, we find 181 ± 19 $J/\psi \rightarrow \phi\pi^+\pi^-$ events, 45 ± 9 $J/\psi \rightarrow \phi\pi^0\pi^0$ events, and 19 ± 6 $\psi(2S) \rightarrow \phi\pi^+\pi^-$ events. We convert these to branching fractions and, after correcting for the modes other than $\phi \rightarrow K^+K^-$, list them in Table XIII. All are consistent with current PDG values, of which the first two are dominated by our previous measurement.

We do not see any evidence for $Y(4260)$ decay to these modes, nor do we see a $Y(4260)$ signal in any other mode

studied here.

Figures 41(a)(b) show the corresponding mass distributions for $\phi f_0(980)$ events, i.e. the subsets of the events in Figs. 40(a) and 40(b) with a di-pion mass in the range 0.85–1.10 GeV/c^2 . Signals at the J/ψ mass are visible in both cases. From Fig. 41(b) we estimate 16 ± 4 ϕf_0 events in the $\pi^0\pi^0$ mode. However, $\phi f_0(980)$ is not the dominant mode contributing to $J/\psi \rightarrow \phi\pi^+\pi^-$ decay. The open histogram of Fig. 42 shows the $\pi^+\pi^-$ invariant mass distribution for events in the J/ψ peak of Fig. 40(a) ($|m(K^+K^-\pi^+\pi^-) - m(J/\psi)| < 0.05 \text{ GeV}/c^2$); events in the J/ψ sidebands ($0.05 < |m(K^+K^-\pi^+\pi^-) - m(J/\psi)| < 0.1 \text{ GeV}/c^2$) are shown by the hatched histogram. A two-peak structure is visible that is very similar to that studied by the BES Collaboration [31] and observed in $D_s^+ \rightarrow \pi^+\pi^-\pi^+$ decay [32]. In both cases the $\pi^+\pi^-$ system is believed to couple to an $s\bar{s}$ system; both $\pi^+\pi^-$ distributions exhibit a clear $f_0(980)$ peak and a broad bump in the 1.3–1.5 GeV/c^2 region. The analysis of Refs. [31, 32] shows that this bump is made up of $f_2(1270)$ and $f_0(1370)$ contributions; we denote this region by f_x . By selecting $f_0(980)$ in the 0.85–1.10 GeV/c^2 range and f_x in the 1.1–1.5 GeV/c^2 range, shown by vertical lines in Fig. 42, and subtracting J/ψ side band background we find 57 ± 9 $J/\psi \rightarrow \phi f_0(980)$ events and 61 ± 10 $J/\psi \rightarrow \phi f_x$ events.

Using Eq.(10) and dividing by the appropriate branching fractions, we obtain the J/ψ branching fractions listed in Table XIII. The measurements of $B_{J/\psi \rightarrow \phi f_0}$ in the $\pi^+\pi^-$ and $\pi^0\pi^0$ decay modes of the f_0 are consistent with each other and with the PDG value, and combined they have roughly the same precision as listed in Ref.[5].

Note that, in contrast to $\phi(1680) \rightarrow \phi\pi\pi$ decay, there is no indication of a $J/\psi \rightarrow \phi f_0(600)$ decay mode. Only $J/\psi \rightarrow \phi f_0(980)$ is observed, as is true for the $Y(2175)$ state.

We also observe 12 ± 4 $\psi(2S) \rightarrow \phi f_0$, $f_0 \rightarrow \pi^+\pi^-$ events, which we convert to the branching fraction listed in Table XIII; it is consistent with the value in Ref. [5], assuming $B_{f_0 \rightarrow \pi^+\pi^-} = 2/3$.

The hatched histogram in Fig. 30(a) shows the K^+K^- invariant mass distribution, when the other kaon pair is in the ϕ region, for the $K^+K^-K^+K^-$ events in the J/ψ peak, selected by requiring $|m(K^+K^-) - m(J/\psi)| < 0.05 \text{ GeV}/c^2$. Subtracting sideband events we find 163 ± 19 events corresponding to $J/\psi \rightarrow \phi K^+K^-$ decay. Using our normalization we obtain the branching fraction listed in Table XIII which agrees with that in Ref. [5], but has better precision. In obtaining these values, we have used $B(\phi \rightarrow K^+K^-) = 0.489$ [5], and assume equal rates for $J/\psi \rightarrow \phi K^+K^-$ and $J/\psi \rightarrow \phi K^0\bar{K}^0$.

X. SUMMARY

We use the excellent charged-particle tracking, track identification, and photon detection of the *BABAR* detector to fully reconstruct events of the type

TABLE XIII: Summary of the J/ψ and $\psi(2S)$ branching fraction values obtained in this analysis.

Measured Quantity	Measured Value (eV)	J/ψ or $\psi(2S)$ Branching Fraction (10^{-3}) This work	PDG2010
$\Gamma_{ee}^{J/\psi} \cdot \mathcal{B}_{J/\psi \rightarrow K^+ K^- \pi^+ \pi^-}$	$37.94 \pm 0.81 \pm 1.10$	$6.84 \pm 0.15 \pm 0.27$	6.6 ± 0.5
$\Gamma_{ee}^{J/\psi} \cdot \mathcal{B}_{J/\psi \rightarrow K^+ K^- \pi^0 \pi^0}$	$11.75 \pm 0.81 \pm 0.90$	$2.12 \pm 0.15 \pm 0.18$	2.45 ± 0.31
$\Gamma_{ee}^{J/\psi} \cdot \mathcal{B}_{J/\psi \rightarrow K^+ K^- K^+ K^-}$	$4.00 \pm 0.33 \pm 0.29$	$0.72 \pm 0.06 \pm 0.05$	0.76 ± 0.09
$\Gamma_{ee}^{J/\psi} \cdot \mathcal{B}_{J/\psi \rightarrow K^{*0} \bar{K}_2^{*0}} \cdot \mathcal{B}_{K^{*0} \rightarrow K^+ \pi^-} \cdot \mathcal{B}_{\bar{K}_2^{*0} \rightarrow K^- \pi^+}$	$8.59 \pm 0.36 \pm 0.27$	$6.98 \pm 0.29 \pm 0.21$	6.0 ± 0.6
$\Gamma_{ee}^{J/\psi} \cdot \mathcal{B}_{J/\psi \rightarrow K^{*0} \bar{K}^{*0}} \cdot \mathcal{B}_{K^{*0} \rightarrow K^+ \pi^-} \cdot \mathcal{B}_{\bar{K}^{*0} \rightarrow K^- \pi^+}$	$0.57 \pm 0.15 \pm 0.03$	$0.23 \pm 0.06 \pm 0.01$	0.23 ± 0.07
$\Gamma_{ee}^{J/\psi} \cdot \mathcal{B}_{J/\psi \rightarrow \phi \pi^+ \pi^-} \cdot \mathcal{B}_{\phi \rightarrow K^+ K^-}$	$2.19 \pm 0.23 \pm 0.07$	$0.81 \pm 0.08 \pm 0.03$	0.94 ± 0.09
$\Gamma_{ee}^{J/\psi} \cdot \mathcal{B}_{J/\psi \rightarrow \phi \pi^0 \pi^0} \cdot \mathcal{B}_{\phi \rightarrow K^+ K^-}$	$1.36 \pm 0.27 \pm 0.07$	$0.50 \pm 0.10 \pm 0.03$	0.56 ± 0.16
$\Gamma_{ee}^{J/\psi} \cdot \mathcal{B}_{J/\psi \rightarrow \phi K^+ K^-} \cdot \mathcal{B}_{\phi \rightarrow K^+ K^-}$	$2.26 \pm 0.26 \pm 0.16$	$1.66 \pm 0.19 \pm 0.12$	1.83 ± 0.24^a
$\Gamma_{ee}^{J/\psi} \cdot \mathcal{B}_{J/\psi \rightarrow \phi f_0} \cdot \mathcal{B}_{\phi \rightarrow K^+ K^-} \cdot \mathcal{B}_{f_0 \rightarrow \pi^+ \pi^-}$	$0.69 \pm 0.11 \pm 0.05$	$0.25 \pm 0.04 \pm 0.02$	0.18 ± 0.04^b
$\Gamma_{ee}^{J/\psi} \cdot \mathcal{B}_{J/\psi \rightarrow \phi f_0} \cdot \mathcal{B}_{\phi \rightarrow K^+ K^-} \cdot \mathcal{B}_{f_0 \rightarrow \pi^0 \pi^0}$	$0.48 \pm 0.12 \pm 0.05$	$0.18 \pm 0.04 \pm 0.02$	0.17 ± 0.07^c
$\Gamma_{ee}^{J/\psi} \cdot \mathcal{B}_{J/\psi \rightarrow \phi f_x} \cdot \mathcal{B}_{\phi \rightarrow K^+ K^-} \cdot \mathcal{B}_{f_x \rightarrow \pi^+ \pi^-}$	$0.74 \pm 0.12 \pm 0.05$	$0.27 \pm 0.04 \pm 0.02$	0.72 ± 0.13^d
$\Gamma_{ee}^{\psi(2S)} \cdot \mathcal{B}_{\psi(2S) \rightarrow K^+ K^- \pi^+ \pi^-}$	$1.92 \pm 0.30 \pm 0.06$	$0.81 \pm 0.13 \pm 0.03$	0.75 ± 0.09
$\Gamma_{ee}^{\psi(2S)} \cdot \mathcal{B}_{\psi(2S) \rightarrow K^+ K^- \pi^0 \pi^0}$	$0.60 \pm 0.31 \pm 0.03$	$0.25 \pm 0.13 \pm 0.02$	no entry
$\Gamma_{ee}^{\psi(2S)} \cdot \mathcal{B}_{\psi(2S) \rightarrow K^+ K^- K^+ K^-}$	$0.22 \pm 0.10 \pm 0.02$	$0.09 \pm 0.04 \pm 0.01$	0.060 ± 0.014
$\Gamma_{ee}^{\psi(2S)} \cdot \mathcal{B}_{\psi(2S) \rightarrow \phi \pi^+ \pi^-} \cdot \mathcal{B}_{\phi \rightarrow K^+ K^-}$	$0.27 \pm 0.09 \pm 0.02$	$0.23 \pm 0.08 \pm 0.01$	0.117 ± 0.029
$\Gamma_{ee}^{\psi(2S)} \cdot \mathcal{B}_{\psi(2S) \rightarrow \phi f_0} \cdot \mathcal{B}_{\phi \rightarrow K^+ K^-} \cdot \mathcal{B}_{f_0 \rightarrow \pi^+ \pi^-}$	$0.17 \pm 0.06 \pm 0.02$	$0.15 \pm 0.05 \pm 0.01$	0.068 ± 0.024^e

^a $\mathcal{B}_{J/\psi \rightarrow \phi \bar{K} K}$ obtained as $2 \cdot \mathcal{B}_{J/\psi \rightarrow \phi K^+ K^-}$.

^bNot corrected for the $f_0 \rightarrow \pi^0 \pi^0$ mode.

^cNot corrected for the $f_0 \rightarrow \pi^+ \pi^-$ mode.

^dWe compare our $\phi f_x, f_x \rightarrow \pi^+ \pi^-$ mode with $\phi f_2(1270)$.

^e $\mathcal{B}_{\psi(2S) \rightarrow \phi f_0, f_0 \rightarrow \pi^+ \pi^-}$

$e^+ e^- \rightarrow \gamma e^+ e^- \rightarrow \gamma K^+ K^- \pi^+ \pi^-, \gamma K^+ K^- \pi^0 \pi^0$, and $\gamma K^+ K^- K^+ K^-$, where the γ is radiated from the initial state e^+ or e^- . Such events are equivalent to direct $e^+ e^-$ annihilation at a c.m. energy corresponding to the mass of the hadronic system. Consequently, we are able to use the full *BABAR* data set to study annihilation into these three final states from their respective production thresholds up to 5 GeV c.m. energy. The $K^+ K^- \pi^+ \pi^-$, $K^+ K^- \pi^0 \pi^0$ and $K^+ K^- K^+ K^-$ measurements are consistent with, and supersede, our previous results [7].

The systematic uncertainties on the $e^+ e^- \rightarrow K^+ K^- \pi^+ \pi^-, K^+ K^- \pi^0 \pi^0$ and $K^+ K^- K^+ K^-$ cross section values are 4%, 7% and 9%, respectively, for $E_{\text{c.m.}} < 3$ GeV, and increase, respectively, to 11%, 16% and 13% in the 3–5 GeV range. The values obtained are considerably more precise than previous measurements, and cover this low-energy range completely. As such they provide useful input to calculations of the hadronic corrections to the anomalous magnetic moment of the muon, and of the fine structure constant at the Z^0 mass.

These final states exhibit complex resonant substructures. For the $K^+ K^- \pi^+ \pi^-$ final state we measure the cross sections for the specific channels $e^+ e^- \rightarrow K^*(892)^0 K^- \pi^+$, $\phi \pi^+ \pi^-$, and ϕf_0 , and, for the first time, for the $e^+ e^- \rightarrow K_2^*(1430)^0 K^- \pi^+$ and $e^+ e^- \rightarrow \rho(770)^0 K^+ K^-$ reactions. We also observe signals for the $K_1(1270)$, $K_1(1400)$, and $f_2(1270)$ resonances. It is diffi-

cult to disentangle these contributions to the final state, and we make no attempt to do so in this paper. We note that the ρ^0 signal is consistent with being due entirely to K_1 decays, and that while the total cross section is dominated by the $K^*(892)^0 K^- \pi^+$ channels, there is no significant signal for $e^+ e^- \rightarrow K^*(892)^0 \bar{K}^*(892)^0$.

For the $K^+ K^- \pi^0 \pi^0$ final state we measure the cross section for $e^+ e^- \rightarrow \phi f_0$, and observe signals for the $K^*(892)^\pm$ and $K_2^*(1430)^\pm$ resonances. Again, the total cross section is dominated by the $K^*(892)^+ K^- \pi^0$ channel, but about 30% of events are produced in the $e^+ e^- \rightarrow K^*(892)^+ K^*(892)^-$ reaction. For the $K^+ K^- \pi^0 \pi^0$ final state we note that the cross section is roughly a factor of four smaller than that for the $K^+ K^- \pi^+ \pi^-$ over most of the $E_{\text{c.m.}}$ range, consistent with a factor of two isospin suppression of the $\pi^0 \pi^0$ final state and another factor of two for the relative branching fractions of the neutral and charged K^* to charged kaons.

With the increased data sample for the present analysis, we perform a more detailed study of the $e^+ e^- \rightarrow \phi(1020) \pi \pi$ reaction. The $\pi^+ \pi^-$ and $\pi^0 \pi^0$ invariant mass distributions both show a clear $f_0(980)$ signal, and broad structure at lower mass interpreted as the $f_0(600)$. We obtain parameter values for these resonances. The $\phi \pi^+ \pi^-$ cross section measured in the $K^+ K^- \pi^+ \pi^-$ final state shows a structure around 1.7 GeV and some structures above 2.0 GeV. The corresponding $\phi \pi^0 \pi^0$ cross

section for the $K^+K^-\pi^0\pi^0$ final state exhibits consistent with $\phi\pi^+\pi^-$ behavior, as reported in Ref. [7]. If the $f_0(980)$ is excluded from the di-pion mass distribution, no structures above 2.0 GeV are seen. We fit the observed cross section with the VMD model assuming $\phi(1680) \rightarrow \phi f_0(600)$ and $\phi(1680) \rightarrow \phi f_0(980)$ decay; the latter appears to be responsible for the threshold increase of the cross section at 2.0 GeV. Confirming our previous study [7], our data require an additional resonance at 2.175 GeV, which we call the $Y(2175)$, with decay to $\phi f_0(980)$, but not to $\phi f_0(600)$. Further investigation reveals consistent results for the $K^+K^-K^+K^-$ final state, and clear $Y(2175)$ signals in the $K^+K^-f_0(980)$ channels, with $f_0(980) \rightarrow \pi^+\pi^-$ and $\pi^0\pi^0$. This structure can be interpreted as a strange partner (with c -quarks replaced by s -quarks) of the $Y(4260)$ [34], which has the analogous decay mode $J/\psi\pi^+\pi^-$, or perhaps as an $s\bar{s}s\bar{s}$ state that decays predominantly to ϕf_0 .

In the $K^+K^-K^+K^-$ mode we find $e^+e^- \rightarrow \phi K^+K^-$ to be the dominant channel. With the current data sample we can say little about other K^+K^- combination. We observe an enhancement near threshold, consistent with the ϕf_0 channel and if these events are selected we have an indication of a $Y(2175)$ signal. Two other structures in the K^+K^- invariant mass spectrum are seen: the smaller could be an indication of the $\phi f_0(1370)$ final state, and the larger of the $\phi f_2'(1525)$ mode. If events corresponding to the $\phi f_2'(1525)$ final state are selected, the $K^+K^-K^+K^-$ cross section shows a resonance-like structure around 2.7 GeV, and a strong J/ψ signal, which has been studied in detail by the BES Collaboration [31]. In the $K^+K^-K^+K^-$ cross section we observe a sharp peak at 2.3 GeV which corresponds to the ϕK^+K^- channel with the K^+K^- invariant mass in the 1.06–1.2 GeV/ c^2 region.

We also investigate charmonium decays into the stud-

ied final states and into their intermediate channels. Some of the obtained J/ψ branching fractions listed in Table XIII are as precise as, or more precise than, the current world averages, many of which were obtained in our previous study [7]; the latter are superseded by our new results. We do not observe the $Y(4260)$ in any of the final states studied.

ACKNOWLEDGMENTS

We are grateful for the extraordinary contributions of our PEP-II colleagues in achieving the excellent luminosity and machine conditions that have made this work possible. The success of this project also relies critically on the expertise and dedication of the computing organizations that support *BABAR*. The collaborating institutions wish to thank SLAC for its support and the kind hospitality extended to them. This work is supported by the US Department of Energy and National Science Foundation, the Natural Sciences and Engineering Research Council (Canada), the Commissariat à l’Energie Atomique and Institut National de Physique Nucléaire et de Physique des Particules (France), the Bundesministerium für Bildung und Forschung and Deutsche Forschungsgemeinschaft (Germany), the Istituto Nazionale di Fisica Nucleare (Italy), the Foundation for Fundamental Research on Matter (The Netherlands), the Research Council of Norway, the Ministry of Education and Science of the Russian Federation, Ministerio de Ciencia e Innovación (Spain), and the Science and Technology Facilities Council (United Kingdom). Individuals have received support from the Marie-Curie IEF program (European Union), the A. P. Sloan Foundation (USA) and the Binational Science Foundation (USA-Israel).

-
- [1] V. N. Baier and V. S. Fadin, Phys. Lett. **B27**, 223 (1968).
 - [2] A. B. Arbuzov *et al.*, J. High Energy Phys. **9812**, 009 (1998).
 - [3] S. Binner, J.H. Kühn and K. Melnikov, Phys. Lett. **B459**, 279 (1999).
 - [4] M. Benayoun *et al.*, Mod. Phys. Lett. **A14**, 2605 (1999).
 - [5] C. K. Nakamura *et al.* (Particle Data Group), Journal of Physics **G37**, 075021 (2010).
 - [6] See for example: S. Gomez-Avila, M. Napsuciale, E. Oset, Phys. Rev. **D79**, 034018,2009; M. Napsuciale, E. Oset, K. Sasaki, C.A. Vaquera-Araujo, Phys.Rev. **D76**, 074012 (2007).
 - [7] B. Aubert *et al.* (*BABAR* Collaboration), Phys. Rev. **D76**, 012008 (2007).
 - [8] M. Ablikim *et al.* (BES Collaboration), Phys. Rev. Lett. **100**, 102003 (2008).
 - [9] C.P. Shen *et al.* (Belle Collaboration), Phys. Rev. **D80**, 031101(R) (2009).
 - [10] M. Davier, S. Eidelman, A. Höcker, Z. Zhang, Eur. Phys. J. **C31**, 503 (2003).
 - [11] B. Aubert *et al.* (*BABAR* Collaboration), Phys. Rev. **D69**, 011103 (2004).
 - [12] B. Aubert *et al.* (*BABAR* Collaboration), Phys. Rev. **D70**, 072004 (2004).
 - [13] B. Aubert *et al.* (*BABAR* Collaboration), Phys. Rev. **D71**, 052001 (2005).
 - [14] B. Aubert *et al.* (*BABAR* Collaboration), Phys. Rev. **D73**, 052003 (2006).
 - [15] B. Aubert *et al.* (*BABAR* Collaboration), Phys. Rev. **D76**, 092005 (2007).
 - [16] B. Aubert *et al.* (*BABAR* Collaboration), Phys. Rev. **D77**, 092002 (2008).
 - [17] B. Aubert *et al.* (*BABAR* Collaboration), Phys. Rev. Lett. **103**, 231801 (2009).
 - [18] A. Cordier *et al.* (DM1 Collaboration), Phys. Lett. **B110**, 335 (1982).
 - [19] B. Aubert *et al.* (*BABAR* Collaboration), Nucl. Instrum. and Meth. **A479**, 1 (2002); W. Menges, IEEE Nucl. Sci. Simp. Conf. Rec. **5**, 1470 (2006).
 - [20] H. Czyż and J. H. Kühn, Eur. Phys. J. **C18**, 497 (2001).

- [21] A. B. Arbuzov *et al.*, J. High Energy Phys. **9710**, 001 (1997).
- [22] M. Caffo, H. Czyż, E. Remiddi, Nuovo Cim. **A110**, 515 (1997); Phys. Lett. **B327**, 369 (1994).
- [23] E. Barberio, B. van Eijk and Z. Was, Comput. Phys. Commun. **66**, 115 (1991).
- [24] S. Agostinelli *et al.* (GEANT4 Collaboration), Nucl. Instrum. Methods Phys. Res., Sect. A **506**, 250 (2003).
- [25] T. Sjöstrand, Comput. Phys. Commun. **82**, 74 (1994).
- [26] S. Jadach and Z. Was, Comput. Phys. Commun. **85**, 453 (1995).
- [27] N.N. Achasov and A.A. Kozhevnikov, Phys. Rev. **D55**, 2663 (1997).
- [28] A. Aloisio *et al.* (KLOE Collaboration), Phys. Lett. **B537**, 21 (2002).
- [29] S. Pacetti, Eur. Phys. J. **A31**, 665 (2007).
- [30] T. A. Armstrong *et al.* (WA76 Collaboration), Z. Phys. **C52**, 389 (1991).
- [31] M. Ablikim *et al.* (BES Collaboration), Phys. Lett. **B607**, 243 (2005).
- [32] B. Aubert *et al.* (BABAR Collaboration), Phys. Rev. **D79**, 032003 (2009).
- [33] M. Ablikim *et al.* (BES Collaboration), Phys. Lett. **B598**, 149 (2004).
- [34] B. Aubert *et al.* (BABAR Collaboration), Phys. Rev. Lett. **95**, 142001 (2005).